Journal for Multiscale Computational Engineering 8(6), 549–559 (2010)

TOWARD A NONINTRUSIVE STOCHASTIC MULTISCALE DESIGN SYSTEM FOR COMPOSITE MATERIALS

Wei Wu & Jacob Fish*

Multiscale Science and Engineering Center, Rensselaer Polytechnic Institute, Troy, New York 12180

*Address all correspondence to Wei Wu E-mail: wuw3@rpi.edu

In this paper we study a nonintrusive stochastic collocation method in combination with a reduced-order homogenization method for solving partial differential equations with oscillatory random coefficients. The method consists of the two-scale homogenization in space, eigendeformation-based model reduction, Galerkin approximation of the reduced-order problem in space, and collocation approximation based on a sparse grid in the probability space that naturally leads to a nonintrusive approach. By this approach the solution of the original stochastic partial differential equations is constructed from a set of decoupled deterministic solutions from which statistical information is obtained. Preliminary numerical experiments are conducted to determine the feasibility of the method for solving two-scale problems in heterogeneous media.

KEY WORDS: *multiscale, homogenization, nonintrusive, stochastic*

1. INTRODUCTION

It is well known that information across scales contains a certain level of uncertainty due to incomplete knowledge of input parameters and physical laws (assuming that the error of numerical solutions of the deterministic problem is negligible). However, incorporation of stochastic processes into multiscale modeling with accurate assessment of uncertainty propagation across scales is highly challenging. Moreover, despite growing computer power, engineering designs that resolve fine-scale details and account for uncertainty in the input data such as constitutive equations, forcing terms, boundary conditions, and geometry at multiple scales are very rare. When both multiscale and stochastic phenomena are taken into account, cross-cutting multiscale stochastic modeling forms an emerging research frontier, as evidenced by numerous papers, books, new journals, workshops, and funding opportunities. Anecdotally, we counted over one million hits of "stochastic multiscale" on the Google search engine. We refer to few selected references for a comprehensive review of the subject matter (Shi and Ghanem, 2006; Ganapathysubramanian and Zabaras, 2008; Cao et al., 2005; Xu, 2007; DeVolder et al., 2002).

The primary objective of the present manuscript is not to develop a new multiscale or stochastic approach, but rather to explore the feasibility of applying the best combination to practical problems of interest. Our choice of the "best of two worlds" is affected by the ability to integrate existing stochastic and multiscale capabilities. For the multiscale simulation engine we select an eigendeformation-based, reduced-order homogenization method (Fish and Yuan, 2009; Oskay and Fish, 2007; Yuan and Fish, 2009) due to its computational efficiency stemming from a unit cell solution constructed in terms of eigendeformation modes that *a priori* satisfy equilibrium equations at the fine scale, and therefore eliminate the need for costly solution of discretized nonlinear equilibrium. For uncertainty quantification, we choose a nonintrusive approach based on stochastic collocation originally proposed by Mathelin and Hussaini (2003), which when combined with the sparse grid approach (Gerstner and Griebel, 1998; Klimke, 2005) has been shown (Ganapathysubramanian and Zabaras, 2007), outperforms other

1543–1649/10/$35.00

nonintrusive methods, such as nonintrusive polynomial chaos (Walters, 2003; Xiu and Karniadakis, 2002), Monte Carlo simulation, and its improved version based on the Latin hypercube sampling (Iman and Conover, 1980). However, if integration considerations were not an issue, various derivatives of the spectral stochastic finite element method (Ghanem and Spanos, 2003) may have offered computational advantages.

The manuscript is organized as follows. A statement of the two-scale stochastic problem with properties of microphases and microinterfaces as random variables is given in Section 2. These are the dominant variables affecting the coarse-scale quantities of interest, such as critical stresses and strains as indicated in Wu (2010). Reduced-order homogenization and sparse grid collocation methods are reviewed in Section 3. The nonintrusive stochastic multiscale design system (NSMDS), based on the sparse grid collocation method in combination with the reduced order multiscale approach, is given in Section 4. Numerical examples are presented in Section 5. We conclude the manuscript with a brief summary and future work in Section 6.

2. PROBLEM DEFINITION

We assume that various response fields such as displacements, strains, and stresses, denoted as $g(\mathbf{x}, \mathbf{y}, \boldsymbol{\eta})$, are dependent on the macro and micro spatial coordinates, $\mathbf{x}$ and $\mathbf{y} = \mathbf{x}/\zeta$, respectively, related by $0 < \zeta \ll 1$, as well as on a set of input independent random variables $\boldsymbol{\eta} = \{\eta^i\}_{i=1}^d$ spanning the d-dimensional support space Ψ. Since random variables may have different probability density functions $f^i(\eta^i)$, the joint probability density function can be obtained by their product as

$$f(\boldsymbol{\eta}) = \prod_{i=1}^{d} f^i(\eta^i). \tag{1}$$

A two-scale asymptotic expansion is employed to approximate the displacement field

$$\begin{aligned} u_i(\mathbf{x},\mathbf{y},\boldsymbol{\eta}) &= u_i^0(\mathbf{x},\mathbf{y},\boldsymbol{\eta}) + \zeta u_i^1(\mathbf{x},\mathbf{y},\boldsymbol{\eta}) \\ &+ \zeta^2 u_i^2(\mathbf{x},\mathbf{y},\boldsymbol{\eta}) + \cdots . \end{aligned} \tag{2}$$

The resulting two-scale strong form of the boundary value problem is given by
(a) Fine scale

$$\sigma_{ij,y_j}(\mathbf{x},\mathbf{y},\boldsymbol{\eta}) = 0, \qquad \mathbf{x} \in \Omega, \mathbf{y} \in \Theta, \boldsymbol{\eta} \in \Psi \tag{3}$$

$$\begin{aligned} \sigma_{ij}(\mathbf{x},\mathbf{y},\boldsymbol{\eta}) = L_{ijkl}(\mathbf{x},\mathbf{y},\boldsymbol{\eta}) \Big[\varepsilon_{kl}(\mathbf{x},\mathbf{y},\boldsymbol{\eta}) \\ - \sum_I {}^I\mu_{kl}(\mathbf{x},\mathbf{y},\boldsymbol{\eta}) \Big], \qquad \mathbf{x} \in \Omega,\ \mathbf{y} \in \Theta,\ \boldsymbol{\eta} \in \Psi \end{aligned} \tag{4}$$

$$\begin{aligned} \varepsilon_{ij}(\mathbf{x},\mathbf{y},\boldsymbol{\eta}) = u^1_{(i,y_j)} + u^0_{(i,x_j)} = \frac{1}{2}\Bigg[\left(\frac{\partial u_i^1}{\partial y_j} + \frac{\partial u_j^1}{\partial y_i} \right) \\ + \left(\frac{\partial u_i^0}{\partial x_j} + \frac{\partial u_j^0}{\partial x_i} \right) \Bigg], \quad \mathbf{x} \in \Omega,\ \mathbf{y} \in \Theta,\ \boldsymbol{\eta} \in \Psi \end{aligned} \tag{5}$$

$$u_i^1 - \text{periodic on } \partial\Theta \tag{6}$$

(b) Coarse scale

$$\bar{\sigma}_{ij,x_j}(\mathbf{x},\boldsymbol{\eta}) + \bar{b}_i(\mathbf{x}) = 0, \qquad \mathbf{x} \in \Omega, \boldsymbol{\eta} \in \Psi \tag{7}$$

$$\bar{\sigma}_{ij}(\mathbf{x},\boldsymbol{\eta}) \equiv \frac{1}{|\Theta|}\int_\Theta \sigma_{ij}(\mathbf{x},\mathbf{y},\boldsymbol{\eta})\, d\Theta, \quad \mathbf{x} \in \Omega,\ \boldsymbol{\eta} \in \Psi \tag{8}$$

$$u_i^0(\mathbf{x},\boldsymbol{\eta}) = \bar{u}_i(\mathbf{x}), \qquad \mathbf{x} \in \Gamma_u \tag{9}$$

$$\bar{\sigma}_{ij}(\mathbf{x},\boldsymbol{\eta})\, n_j(\mathbf{x}) = \bar{t}_i(\mathbf{x}), \qquad \mathbf{x} \in \Gamma_t \tag{10}$$

where Eq. (4) describes the constitutive relation which assumes an additive decomposition of total strain ε_{ij} into elastic and inelastic components, more generally referred to as *eigenstrains* ${}^I\mu_{kl}$, where the left superscript I stands for various eigenstrain types, such as inelastic deformation, thermal change, moisture effects, etc. For simplicity, we assume that coarse-scale essential and natural boundary conditions as well as fine-scale periodic boundary conditions are deterministic. Similarly, the geometry of body is assumed to be deterministic and depends on coarse-scale coordinates.

In the present manuscript we focus on a case where material constitutive parameters at the fine scale are random variables with a given joint probability distribution. We will assume that the fine-scale topology (or microstructure geometry) is deterministic and that the constitutive relation does not vary randomly from one point to another in the coarse-scale domain Ω. Such variation can be described in terms of random fields with a given covariance structure. Although such random fields are properly described by means of an infinite number of random variables, Karhunen–Loeve expansion (Ghanem and Spanos, 2003) could be employed to describe the random fields in terms of a small number of uncorrelated random variables, but this case is not considered here.

3. REVIEW OF BUILDING BLOCKS OF NSMDS

3.1 Eigendeformation-Based Reduced-Order Homogenization

Due to its nonintrusive nature, the solution in probability support space Ψ can be decoupled into a set of independent problems solvable by a deterministic solver on $\Omega \times \Theta$. We employ an eigendeformation-based homogenization to solve for the two-scale deterministic problem. For each realization $\boldsymbol{\eta} \in \Psi$, we construct a residual-free microscale displacement field $u_i^1(\mathbf{x}, \mathbf{y}, \boldsymbol{\eta})$ to ensure the stress field in a unit cell satisfies equilibrium equations for arbitrary eigenstrains ${}^I\mu_{ij}^0$ and eigenseparations $\delta_{\hat{n}}$

$$\begin{aligned} u_i^1(\mathbf{x}, \mathbf{y}, \boldsymbol{\eta}) &= u_i^{el}(\mathbf{x}, \mathbf{y}, \boldsymbol{\eta}) + \sum_I {}^I u_i^{\mu}(\mathbf{x}, \mathbf{y}, \boldsymbol{\eta}) \\ &+ u_i^{\delta}(\mathbf{x}, \mathbf{y}, \boldsymbol{\eta}) = H_{ikl}^{mic}(\mathbf{y}, \boldsymbol{\eta})\, \bar{\varepsilon}_{kl}(\mathbf{x}, \boldsymbol{\eta}) \\ &+ \sum_I \int_{\Theta} {}^I h_{ikl}^{mic\_\mu}(\mathbf{y}, \hat{\mathbf{y}}, \boldsymbol{\eta})\, {}^I \mu_{kl}^0(\mathbf{x}, \hat{\mathbf{y}}, \boldsymbol{\eta})\, d\hat{\mathbf{y}} \\ &+ \int_S h_{i\hat{n}}^{mic\_\delta}(\mathbf{y}, \hat{\mathbf{y}}, \boldsymbol{\eta})\, \delta_{\hat{n}}(\mathbf{x}, \hat{\mathbf{y}}, \boldsymbol{\eta})\, d\hat{\mathbf{y}}. \end{aligned} \tag{11}$$

The resulting fine-scale displacement gradients is given by

$$\begin{aligned} u_{i,y_j}^1(\mathbf{x}, \mathbf{y}, \boldsymbol{\eta}) &= G_{ijkl}^{mic}(\mathbf{y}, \boldsymbol{\eta})\, \bar{\varepsilon}_{kl}(\mathbf{x}, \boldsymbol{\eta}) \\ &+ \sum_I \int_{\Theta} {}^I g_{ijkl}^{mic\_\mu}(\mathbf{y}, \hat{\mathbf{y}}, \boldsymbol{\eta})\, {}^I \mu_{kl}^0(\mathbf{x}, \hat{\mathbf{y}}, \boldsymbol{\eta})\, d\hat{\mathbf{y}} \\ &+ \int_S g_{ij\hat{n}}^{mic\_\delta}(\mathbf{y}, \hat{\mathbf{y}}, \boldsymbol{\eta})\, \delta_{\hat{n}}(\mathbf{x}, \hat{\mathbf{y}}, \boldsymbol{\eta})\, d\hat{\mathbf{y}}, \end{aligned} \tag{12}$$

where G_{ijkl}^{mic}, ${}^I g_{ijkl}^{mic\_\mu}$, and $g_{ij\hat{n}}^{mic\_\delta}$ are influence functions for macrostrain, eigenstrain, and eigenseparation, respectively. When elastic constitutive parameters are considered as random variables, these influence functions need to be recomputed at each realization by solving a sequence of elastic boundary value problems.

The reduced-order model is obtained by discretizing the eigenstrain and eigenseparation fields as

$$\begin{aligned} {}^I\mu_{ij}^0(\mathbf{x}, \mathbf{y}, \boldsymbol{\eta}) &= \sum_{\alpha=1}^{n_I} {}^I N^{(\alpha)}(\mathbf{y})\, {}^I \bar{\mu}_{ij}^{(\alpha)}(\mathbf{x}, \boldsymbol{\eta}), \\ \delta_{\hat{n}}(\mathbf{x}, \tilde{\mathbf{y}}, \boldsymbol{\eta}) &= \sum_{\xi=1}^{m} N^{(\xi)}(\tilde{\mathbf{y}})\, \bar{\delta}_{\hat{n}}^{(\xi)}(\mathbf{x}, \boldsymbol{\eta}), \end{aligned} \tag{13}$$

where n_I and m are the number of partitions of phases and interfaces, respectively; ${}^I\bar{\mu}_{ij}^{(\alpha)}$ and $\bar{\delta}_{\hat{n}}^{(\xi)}$ are the average eigenstrain and eigenseparation in the phase partition α and in the interface partition ξ, respectively. $N^{(\alpha)}(\mathbf{y})$ is a piecewise constant shape function defined as

$$N^{(\alpha)}(\mathbf{y}) = \begin{cases} 1 & \mathbf{y} \in \Theta^{(\alpha)}, \\ 0 & \mathbf{y} \notin \Theta^{(\alpha)}, \end{cases} \tag{14}$$

whereas $N^{(\xi)}(\tilde{\mathbf{y}})$ is a linear combination of piecewise linear finite element shape functions defined over the surface partition ξ. The reduced-order system of equations can be obtained by

(i) Fine scale

$$\begin{aligned} &\varepsilon_{ij}^{(\beta)}(\mathbf{x}, \boldsymbol{\eta}) - \sum_{I=1}^{N} \sum_{\alpha=1}^{n_I} {}^I P_{ijkl}^{(\beta\alpha)}(\mathbf{y}, \boldsymbol{\eta})\, {}^I \bar{\mu}_{kl}^{(a)}(\mathbf{x}, \eta) \\ &- \sum_{\xi=1}^{m} Q_{ij\hat{n}}^{(\beta\xi)}(\mathbf{y}, \boldsymbol{\eta}) \bar{\delta}_{\hat{n}}^{(\xi)}(\mathbf{x}, \boldsymbol{\eta}) = A_{ijkl}^{(\beta)}(\mathbf{y}, \boldsymbol{\eta}) \bar{\varepsilon}_{kl}(\mathbf{x}, \boldsymbol{\eta}), \\ &- \sum_{I=1}^{N} \sum_{\alpha=1}^{n_I} {}^I C_{\hat{n}kl}^{(\vartheta\alpha)}(\mathbf{y}, \boldsymbol{\eta})\, {}^I \bar{\mu}_{kl}^{(\alpha)}(\mathbf{x}, \boldsymbol{\eta}) + t_{\hat{n}}^{(\vartheta)}(\mathbf{x}, \boldsymbol{\eta}) \\ &- \sum_{\xi=1}^{m} D_{\hat{n}\hat{m}}^{(\vartheta\xi)}(\mathbf{y}, \boldsymbol{\eta}) \bar{\delta}_{\hat{m}}^{(\xi)}(\mathbf{x}, \boldsymbol{\eta}) = B_{\hat{n}kl}^{(\vartheta)}(\mathbf{y}, \boldsymbol{\eta}) \bar{\varepsilon}_{kl}(\mathbf{x}, \boldsymbol{\eta}), \end{aligned} \tag{15}$$

(ii) Coarse scale

$$\begin{aligned} \bar{\sigma}_{ij}(\mathbf{x}, \boldsymbol{\eta}) &= \bar{L}_{ijkl}(\mathbf{y}, \boldsymbol{\eta})\, \bar{\varepsilon}_{kl}(\mathbf{x}, \boldsymbol{\eta}) \\ &+ \sum_{I=1}^{N} \sum_{\alpha=1}^{n_I} {}^I \bar{E}_{ijkl}^{(\alpha)}(\mathbf{y}, \boldsymbol{\eta})\, {}^I \bar{\mu}_{kl}^{(a)}(\mathbf{x}, \boldsymbol{\eta}) \\ &+ \sum_{\xi=1}^{m} \bar{F}_{ij\hat{n}}^{(\xi)}(\mathbf{y}, \boldsymbol{\eta})\, \bar{\delta}_{\hat{n}}^{(\xi)}(\mathbf{x}, \boldsymbol{\eta}), \end{aligned} \tag{16}$$

where $t_{\hat{n}} = G\left(\bar{\delta}_{\hat{n}}\right)$ represents the traction along the interface. All the coefficient tensors are determined prior to nonlinear macro analysis (Yuan and Fish, 2009) and depend on the randomness of material elastic constitutive parameters.

3.2 Stochastic Collocation Method Using Sparse Grid

Consider a stochastic collocation method that approximates probability space in multidimensions by interpolation from a set of collocation points (referred to as realizations). Let $g\left(\eta_{j_1}^1, \eta_{j_2}^2, \cdots, \eta_{j_d}^d\right)$ be a deterministic solution of the two-scale problem (15)–(16) at a collocation

point $(\eta_{j_1}^1, \eta_{j_2}^2, \cdots, \eta_{j_d}^d)$ in the *d*-dimensional probability space, where j_k denotes the j_kth node index in k-direction (or *k*th random variable). Denote the total number of grid points in k-direction as m_k. The interpolated solution in random space is given by

$$\hat{g}(\boldsymbol{\eta}) = \sum_{j_1=1}^{m_1} \cdots \sum_{j_d=1}^{m_d} g\left(\eta_{j_1}^1, \cdots, \eta_{j_d}^d\right) N_{j_1}^1\left(\eta^1\right) \cdot N_{j_2}^2\left(\eta^2\right) \cdots N_{j_d}^d\left(\eta^d\right) \tag{17}$$

where $N_{j_k}^k$ is an interpolation function in the k-direction, such as Lagrange polynomials, satisfying the interpolation property $N_{j_k}^k\left(\eta_{j_s}^k\right) = \begin{cases} 1 \text{ if } j_s = j_k \\ 0 \text{ otherwise} \end{cases}$.

The quantities of interest are typically the statistical moments of $g(\boldsymbol{\eta})$. The pth statistical moment denoted by M_p can be calculated using numerical integration that takes advantage of the function evaluation at the collocation points

$$M_p = \sum_{j_1=1}^{m_1} \cdots \sum_{j_d=1}^{m_d} \left[g\left(\eta_{j_1}^1, \cdots, \eta_{j_d}^d\right)\right]^p f\left(\eta_{j_1}^1, \cdots, \eta_{j_d}^d\right) \cdot \left(w_{j_1}^1 \cdot w_{j_2}^2 \cdots w_{j_d}^d\right) \tag{18}$$

where $f\left(\eta_{j_1}^1, \cdots, \eta_{j_d}^d\right)$ is a joint probability density function; $\left(w_{j_1}^1 \cdot w_{j_2}^2 \cdots w_{j_d}^d\right)$ are weights at quadrature points $\left(\eta_{j_1}^1, \cdots, \eta_{j_d}^d\right)$.

To realize the enormous computational complexity of the tensor product rule in multidimensions, consider a tensor product of two random variables with 10 nodes in η_1 and η_2 directions, which has a complete polynomial order of up to 9. From the Pascal triangle it follows that there are 55 monomials forming complete polynomial expansion of up to order 9, yet the tensor product involves summation of 100 terms, i.e., 45% of terms are wasted. The percentage of wasted monomials grows exponentially with increase in the number of random variables. For instance, in 3d, 78% of terms are wasted, in 4d, it increases to 92%, and in 5d and 6d, the number of wasted terms reaches 97 and 99%, respectively. This is often referred to as a curse of dimensionality.

The basic idea of the *sparse grid* method, originally proposed by Smolyak (1963), is to construct a hierarchal basis of one-dimensional interpolants and then to consider a tensor product of interpolants that contribute only to the completeness of the polynomial we want to approximate.

Starting from a one-dimensional univariate condition, the hierarchical interpolation is given by

$$\hat{g}\left(\eta^i\right) = \sum_{j=1}^{m_i} g\left(\eta_j^i\right) N_j^i\left(\eta^i\right). \tag{19}$$

Here i denotes the interpolation level. Similarly, for the $(i-1)$th interpolation level, we have

$$\hat{g}\left(\eta^{i-1}\right) = \sum_{j=1}^{m_{i-1}} g\left(\eta_j^{i-1}\right) N_j^{i-1}\left(\eta^{i-1}\right), \tag{20}$$

where m_{i-1} and m_i denote the total number of basis nodes in levels $i-1$ and i, respectively. In the following we consider a Clenshaw–Curtis grid that provides a nested structure of basis nodes, i.e., the basis nodes in level $i-1$ are a subset of those in level i. Since level i interpolants can exactly represent $\hat{g}\left(\eta^{i-1}\right)$ we have

$$\hat{g}\left(\eta^{i-1}\right) = \sum_{j=1}^{m_i} N_j^i\left(\eta^i\right) \left[\sum_{k=1}^{m_{i-1}} g\left(\eta_k^{i-1}\right) N_k^{i-1}\left(\eta_j^{i-1}\right)\right]. \tag{21}$$

The difference between the two subsequent levels is defined as

$$\begin{aligned} \Delta^i &= \hat{g}\left(\eta^i\right) - \hat{g}\left(\eta^{i-1}\right) = \sum_{j=1}^{m_i} g\left(\eta_j^i\right) N_j^i\left(\eta^i\right) \\ &- \sum_{j=1}^{m_i} N_j^i\left(\eta^i\right) \left[\sum_{k=1}^{m_{i-1}} g\left(\eta_k^{i-1}\right) N_k^{i-1}\left(\eta_j^{i-1}\right)\right] \\ &= \sum_{j=1}^{m_i} \left[g\left(\eta_j^i\right) - \hat{g}\left(\eta_j^{i-1}\right)\right] N_j^i\left(\eta^i\right). \end{aligned} \tag{22}$$

Since $g\left(\eta_j^i\right) = \hat{g}\left(\eta_j^{i-1}\right)$ on m_{i-1} nodes of level $i-1$, Eq. (22) can be rewritten as

$$\begin{aligned} \Delta^i = \hat{g}\left(\eta^i\right) - \hat{g}\left(\eta^{i-1}\right) &= \sum_{j=1}^{m_i^\Delta} \left[g\left(\eta_j^i\right)\right. \\ &\left. - \hat{g}\left(\eta_j^{i-1}\right)\right] N_j^i\left(\eta^i\right), \end{aligned} \tag{23}$$

where $m_i^\Delta = m_i - m_{i-1}$ denotes the number of new nodes that are added to level i from level $i-1$.

The Smolyak algorithm constructs the sparse interpolation space in *d*-dimensions as follows. Let i_k, $k = 1, 2, \cdots, d$ be the interpolation level along the k-direction, and $i = (i_1, i_2, \cdots, i_d)$ the multi-index with $|\mathbf{i}| = i_1 + \cdots + i_d$. The Smolyak algorithm builds the interpolation function in multidimensions by adding a combination of one-dimensional functions of order i_k subject to the constraint $q - d + 1 \le |\mathbf{i}| \le q$, which yields

$$\hat{g}(\boldsymbol{\eta})|_q = \hat{g}(\boldsymbol{\eta})|_{q-1} + \sum_{|i|=q} \left(\Delta^{i_1} \otimes \cdots \otimes \Delta^{i_d}\right), \tag{24}$$

$$\begin{aligned}\left(\Delta^{i_1}\otimes\cdots\otimes\Delta^{i_d}\right)&=\sum_{j_1=1}^{m_1^{\Delta}}\cdots\sum_{j_d=1}^{m_d^{\Delta}}\Big[g\left(\eta_{j_1}^{i_1},\cdots,\eta_{j_d}^{i_d}\right)\\&-\hat{g}\left(\eta_{j_1}^{i_1},\cdots,\eta_{j_d}^{i_d}\right)|_{q-1}\Big]N_{j_1}^{i_1}\left(\eta^{i_1}\right)\\&\times N_{j_2}^{i_2}\left(\eta^{i_2}\right)\cdots N_{j_d}^{i_d}\left(\eta^{i_d}\right),\end{aligned}\tag{25}$$

where $q-d\geq 0$ denotes the sampling level in the sparse grid. Equation (24) states that given an approximation in the previous level $\hat{g}\left(\eta\right)|_{q-1}$, new sampling points are selected so that monomials that satisfy $|i|=q$ are added to the approximation in the new level q.

The Clenshaw–Curtis grid points are defined as

$$\begin{aligned}&\eta_{j_k}^{i_k}=-\cos\left(\frac{\pi\left(j_k-1\right)}{m_k-1}\right),\quad j_k=1,\cdots,m_k\\&\eta_1^{i_k}=0\ \text{ if }\ m_k=1.\\&m_1=1\ \text{ and }\ m_k=2^{i_k-1}+1\ \text{ for }\ i_k>1.\end{aligned}\tag{26}$$

Note that sparse grids are defined on a hypercube$[-1,1]^d$. A mapping function $\mathbf{T}$ is employed to translate points in the hypercube to the random space spanned by random variables η.

4. NONINTRUSIVE STOCHASTIC MULTISCALE DESIGN SYSTEM FOR COMPOSITE MATERIALS

In this section we describe a nonintrusive stochastic multiscale design system aimed at quantifying the influence of various uncertainties in the microstructure on the coarse-scale quantities of interest (QoI). The microstructural uncertainties include elastic constitutive parameters of phases (such as Young's modulus, Poisson ratio), inelastic constitutive parameters of phases and interfaces (such as damage law parameters), and geometric parameters describing material microstructure (such as volume fraction of fiber). The above uncertainties can either vary from one unit cell to another (random fields) or be constant throughout the macro domain (random variables), as shown in Fig. 1.

From a computational complexity point of view and in the context of a reduced-order homogenization method, we identify six levels of computational complexity (category I being of the highest computational complexity):

I. Microstructural geometry as random field

Since microstructural geometry defines residual-free fields in the unit cell, the influence functions will vary from point to point in the coarse-scale domain. Thus, the coefficient tensors of Eqs. (15) and (16) need to be evaluated on the fly during nonlinear simulation at each quadrature point in the macro domain.

II. Microstructural geometry as random variable

Even though the influence functions are constant over the coarse-scale domain, they have to be recomputed due to randomness of the unit cell geometry. This will require recreation of the unit cell computer aided design (CAD) and finite element models.

III. Elastic constitutive parameters of each phase as random fields

While fine-scale elastic properties affect the influence functions, they can be precomputed in the preprocessing stage and consequently reused with each nonlinear constitutive parameter of phases and interfaces. The influence functions also need to be computed on the fly for each macro domain's quadrature point during nonlinear macro simulation.

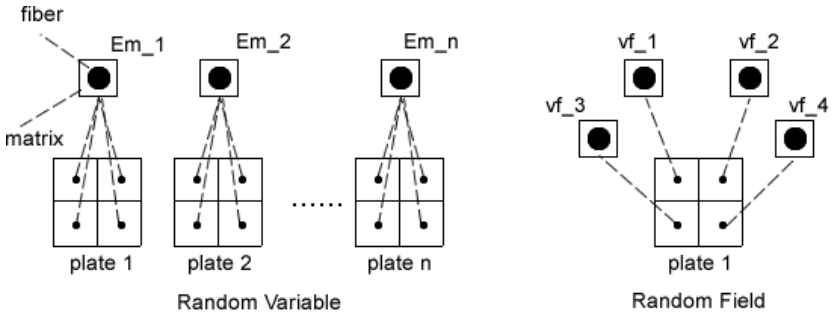

FIG. 1: Random variables and fields.

IV. Inelastic constitutive parameters of each phase/interface as random fields

If elastic properties and microstructural geometry are assumed to be deterministic, then the influence functions need to be computed only once throughout the entire stochastic analysis. The inelastic constitutive laws of micro-phases and micro-interfaces are allowed to vary in macro-domain.

V. Elastic constitutive parameters of each phase as random variables

These parameters affect the influence functions; however, in this case the influence functions are the same from one macro quadrature point to another.

VI. Inelastic constitutive parameters of each phase/interface as random variables

This level is the simplest and most inexpensive scenario.

The general framework of the nonintrusive stochastic multiscale design system (NSMDS) that can address all six levels of complexity is shown in Fig. 2. The NSMDS consists of the following building blocks:

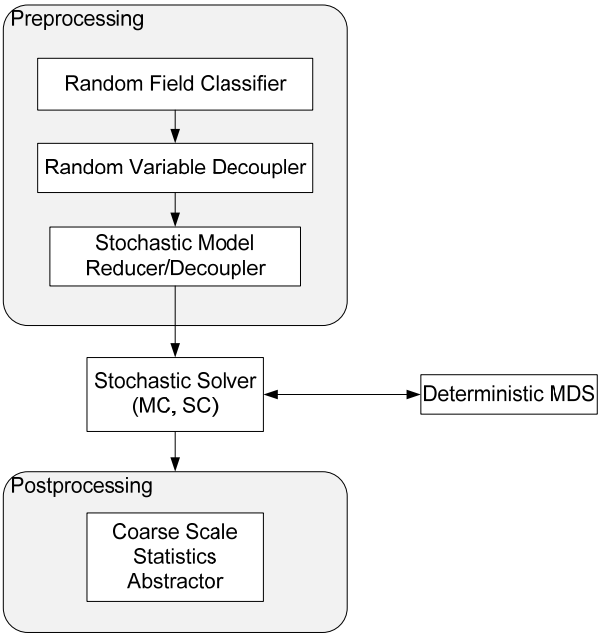

FIG. 2: Block diagram of nonintrusive stochastic multiscale design system.

Random field classifier—The stochastic partial differential equation is classified into one of the six categories described in the previous section.

Random variable decoupler—The original dependent random variables are transformed into independent random variables.

Stochastic model reducer/decoupler—The infinite-dimensional probability space is reduced to a finite-dimensional space of random variables commonly known as a "finite-dimensional noise assumption" using the Karhunen–Loeve (KL) expansion.

Stochastic solver—The Monte Carlo (MC) or stochastic collocation (SC) methods are applied to transform stochastic partial differential equations into deterministic equations in the physical space that can be solved by the deterministic multiscale design system (MDS).

Coarse-scale statistics abstractor—It provides estimation of statistical moments in the quantities of interest and failure probabilities.

In the present manuscript attention is restricted to study levels V and VI of complexity, i.e., we consider independent random elastic and inelastic constitutive variables. The algorithm for this case is summarized in the table below.

Algorithm: Nonintrusive stochastic solver based on sparse grid collocation and reduced order homogenization

1. Set level of the Clenshaw–Curtis sparse grid.
2. Construct sparse grid in hypercube $[-1,1]^d$ and apply mapping to translate grids onto the random variable space $\left[\eta_{lb}^1,\eta_{ub}^1\right]\otimes\cdots\otimes\left[\eta_{lb}^d,\eta_{ub}^d\right]$, where η_{lb}^k and η_{ub}^k are lower bound and upper bound of random variable η^k.
3. Group the grid points with the same elastic constitutive parameters $G_1^{el}\bigcup G_2^{el}\bigcup\cdots\bigcup G_n^{el}$, i.e.,
$$\underbrace{\left(\eta_1^{el_1},\cdots,\eta_{\mathbf{k_1}}^{el_1}\right)}_{G_1^{el}}\bigcup\underbrace{\left(\eta_1^{el_2},\cdots,\eta_{\mathbf{k_2}}^{el_2}\right)}_{G_2^{el}}\bigcup\cdots\bigcup\underbrace{\left(\eta_1^{el_n},\cdots,\eta_{\mathbf{k_q}}^{el_n}\right)}_{G_n^{el}},$$
where $\eta_j^{el_m}$ denotes the j^{th} point in the group G_m^{el}.
4. For each group $G_m^{el},\ \ 1\le m\le n$,
   1) Compute coefficient tensors for Eqs. (15) and (16).

2) For each grid point in the group, $\eta_j^{el_m}$, $1 \leq j \leq \mathbf{k}_m$,
   - update inelastic constitutive parameters and perform simulation,
   - record coarse-scale quantities of interest (QoI's) $g\left(\eta_j^{el_m}\right)$,
   - record joint probability $f\left(\eta_j^{el_m}\right)$ and integration weight $w\left(\eta_j^{el_m}\right)$.

5. Denote the total number of grid points as N, and compute statistical moment of QoIs by $M_p = \sum_{i=1}^{N} \left[g\left(\eta_i\right)\right]^p f\left(\eta_i\right) w\left(\eta_i\right)$.

To this end we compare the sparse grid and equal grid methods. In the uniform grid case, each direction is divided into equal intervals as shown in Fig. 3. We consider a probability density function having normal distribution $N\left(\mu, \sigma^2\right)^d$ in multidimensions. Let $\mu = 0$, $\sigma = 1/3$, and consider integration domain $[\mu - 3\sigma, \mu + 3\sigma]^d = [-1, 1]^d$. The analytical solution is $\left[erf\left(3/\sqrt{2}\right)\right]^d$.

Figure 4 compares the two methods for d ranging from 1 to 5. In all the cases, the sparse grid is found to have a faster convergence rate. However, for low accuracy, it can be seen that the equal grid has a lower computational cost than the sparse grid.

5. NUMERICAL EXAMPLES

We consider a fibrous composite microstructure as a fine-scale model and a 7-layer composite laminate

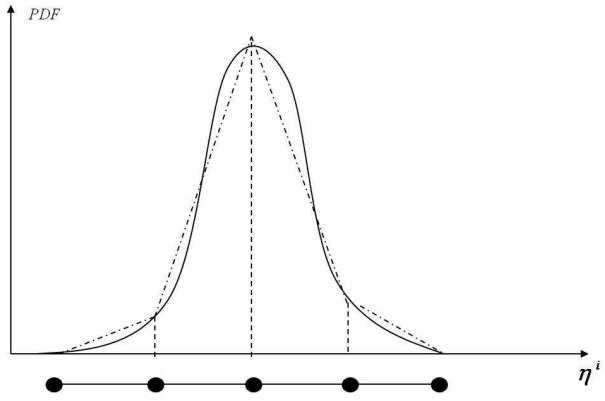

FIG. 3: Equal grid in 1D case.

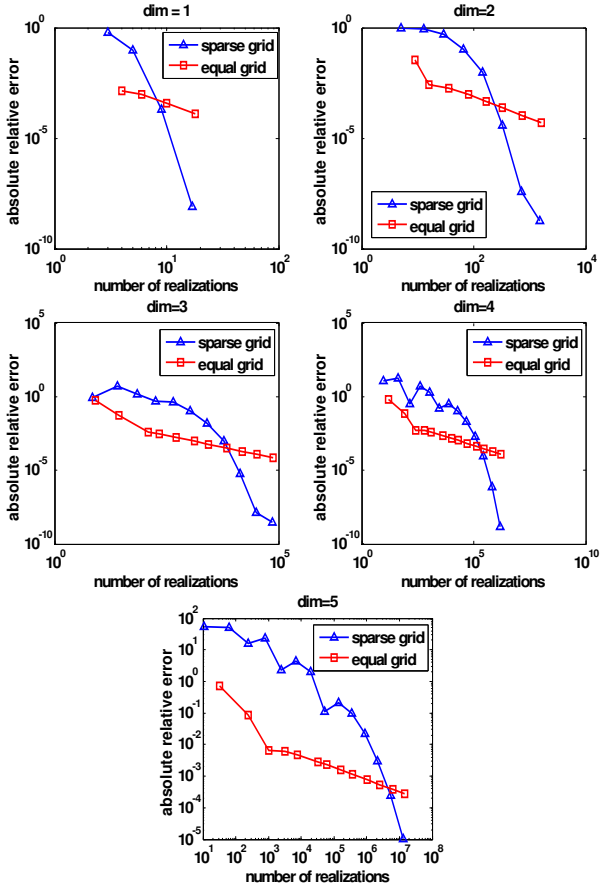

FIG. 4: Numerical integration of multidimensional normal distribution PDF.

0/90/90/0/90/90/0 subjected tensile loading as a coarse-scale model as shown in Fig. 5. For the constitutive model of microphases we consider an isotropic damage model as shown in Fig. 6, where S denotes the elastic proportional limit stress and G the strain energy per unit volume. The material properties considered are shown in Table 1.

A typical stress–strain curve is plotted in Fig. 7. We investigate the effect of variations in material inelastic parameters on the coarse-scale ultimate stress and the effect of variations in material elastic parameters on homogenization modulus. For the reference solution, we consider a Latin-hypercube Monte Carlo (LHMC) method with up to 10,000 sampling points.

Problem 1: Inelastic constitutive parameters as random variables with Gaussian distribution

Statistical properties of random variables are depicted Table 2 for problem 1.

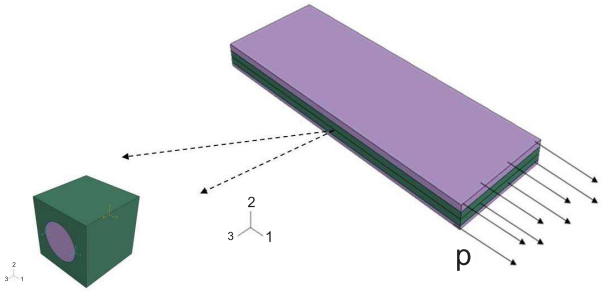

FIG. 5: Tensile test of 0/90/90/0/90/90/0 composite laminate (symmetric model).

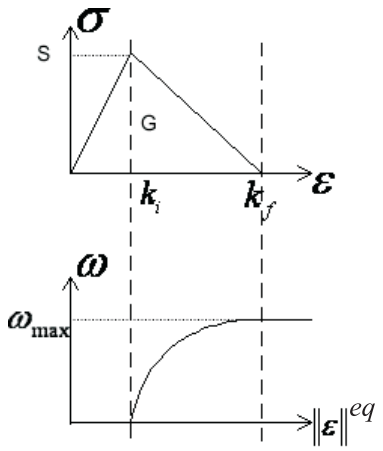

FIG. 6: Isotropic damage model for phase.

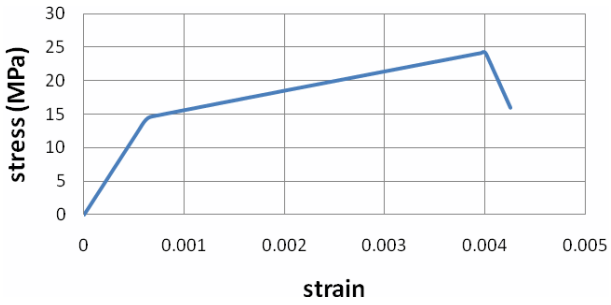

FIG. 7: Strain/stress curve of tensile test of composite laminate.

TABLE 1: Microstructural material properties

	E (MPa)	v	S (MPa)	G
Matrix	2.E+4	0.2	13	0.04
Fiber	4.E+4	0.2	160	0.1

Figure 8 compares the absolute relative error in the mean and variance of ultimate stress as obtained by the sparse grid, equal grid, and LHMC. Several observations are noteworthy. First, LHMC at 5000 realizations seems to converge, and the reference solution in the following examples is set as LHMC at 5000 points. Second, LHMC needs a larger number of realizations than the collocation methods, and the computational time of LHMC is about 5–6 times higher. Third, sparse grid and equal grid collocation methods converge to the reference solution as the number of realizations increases; however, the latter seems to oscillate at high accuracy level.

Problem 2: Inelastic constitutive parameters as random variables with Lognormal distribution

Statistical properties of random variables are depicted in Table 3 for problem 2. LHMC at 5000 points is used as a reference solution. The equal and sparse grid methods are compared in Fig. 9.

Problem 3: Elastic constitutive parameters as random variables with Lognormal distribution

Statistical properties of random variables are depicted in Table 4 for problem 3. In this example, an elastic homogenization modulus of coarse-scale model is selected as a quantity of interest. LHMC at 5000 sampling points is used as a reference solution. Figure 10 compares the equal and sparse grid methods.

Problem 4: Four-dimensional random space

We consider the inelastic properties of the two phases as random variables and the coarse-scale ultimate stress as a quantity of interest. Statistical properties of input variables are listed in Table 5. The sparse grid collocation method is studied in Fig. 11, but no comparison to the reference solution is made as it would require millions of LHMC realizations. It seems that the mean and variance reached a plateau value at relatively small number of realizations, but without having a reference solution this may or may not be a converged value.

6. SUMMARY

A nonintrusive stochastic multiscale design system (NS-MDS) was developed and limited numerical experiments were conducted to study its performance. The design system decouples stochastic partial differential equations into a set of deterministic equations, which are subsequently solved using a two-scale eigendeformation-based reduced-order homogenization method. A stochastic collocation method based on a sparse grid was seamlessly integrated into a deterministic multiscale design system, which employs ABAQUS as a coarse-scale solver. While

TABLE 2: Inelastic random variables for problem 1

	Mean	Standard deviation	COV(%)	Distribution
S of matrix	13	0.65	5	Gaussian
S of fiber	160	8	5	Gaussian

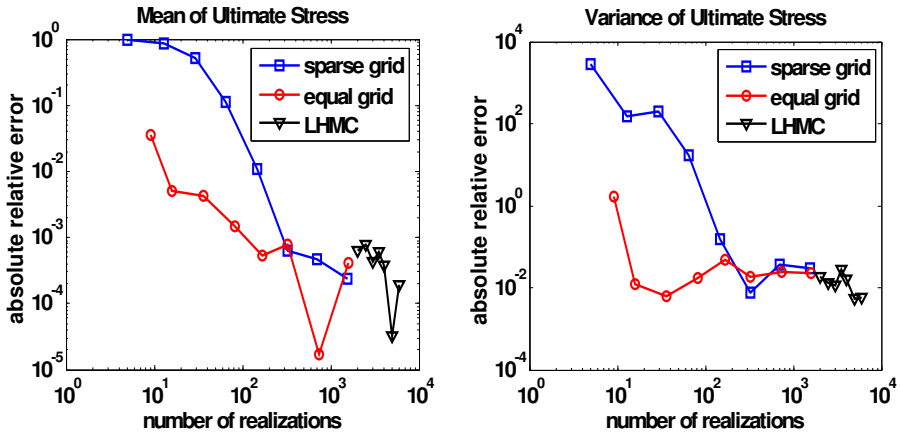

FIG. 8: Absolute relative error in mean and variance of ultimate stress for problem 1. Problem 2: Inelastic constitutive parameters as random variables with log normal distribution.

TABLE 3: Inelastic random variables for problem 2

	Mean	Standard deviation	COV(%)	Distribution
S of matrix	13	0.65	5	Log normal
S of fiber	160	8	5	Log normal

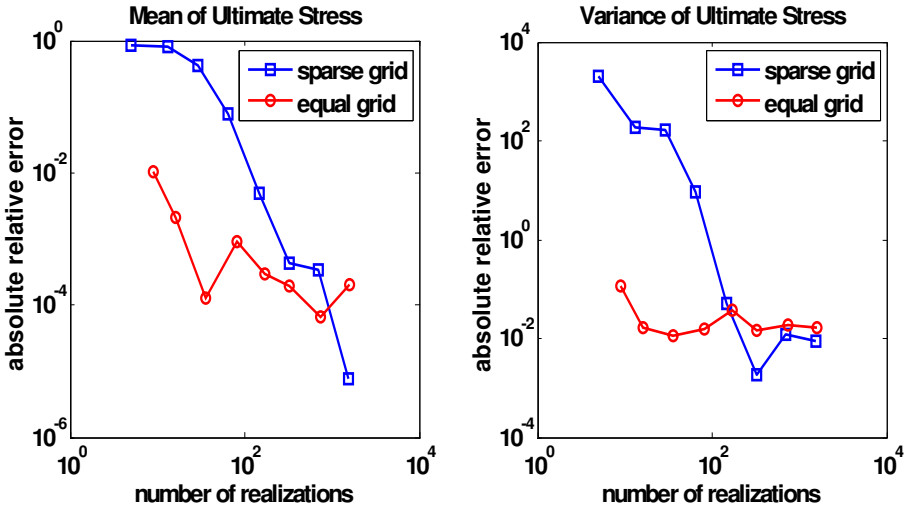

FIG. 9: Absolute relative error in mean and variance of ultimate stress for problem 2. Problem 3: Elastic constitutive parameters as random variables with log normal distribution.

TABLE 4: Elastic random variables for problem 3

	Mean	Standard deviation	COV (%)	Distribution
E of matrix	2.E+4	2.E+2	1	Log normal
E of fiber	4.E+4	4.E+2	1	Log normal

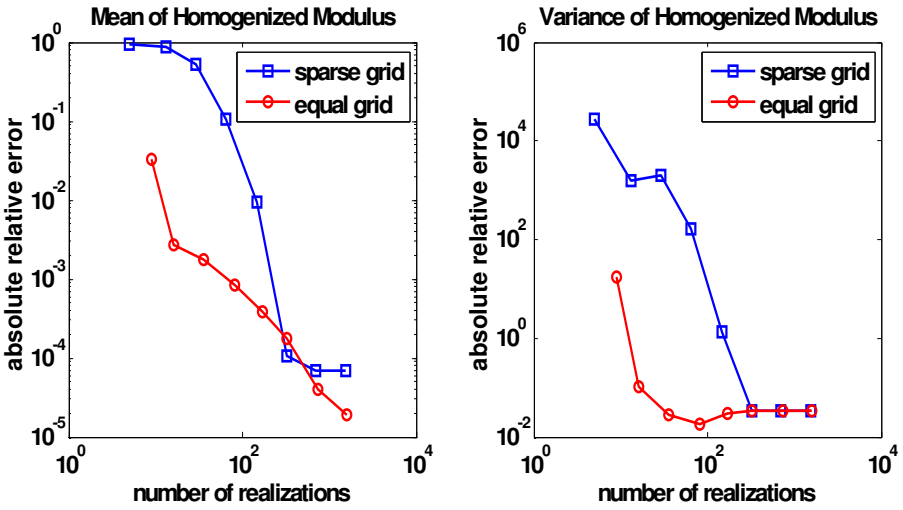

FIG. 10: Absolute relative error in mean and variance of homogenization modulus for problem 3.

TABLE 5: Inelastic random variables for problem 4

	Mean	Standard deviation	COV (%)	Distribution type
S of matrix	13	0.65	5	Gaussian
G of matrix	0.04	0.002	5	Uniform
S of fiber	160	8	5	Gaussian
G of fiber	0.1	0.005	5	Uniform

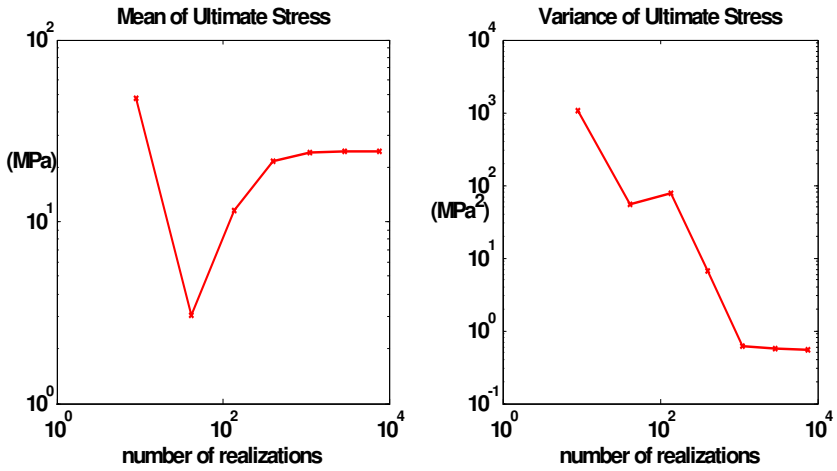

FIG. 11: Prediction of mean and variance of ultimate stress by stochastic collocation using sparse grid for problem 4.

we have demonstrated the feasibility of transforming a deterministic commercial finite element solver of choice into a stochastic solver, the overall performance was hindered by repeated calls to the license manager, which considerably slowed the overall solution process and thus limited our studies to problems of low computational complexity with a limited number of random variables representing microscopic material constitutive parameters.

In our future studies we will consider problems of considerably higher computational complexity (levels I–IV) by replacing the commercial deterministic solver with an in-house developed finite element solver.

ACKNOWLEDGEMENTS

This work was supported by the Office of Naval Research, grant no. N000140310396.

REFERENCES

Cao, Y., Gillespie, D., and Petzold, L., Multiscale stochastic simulation algorithm with stochastic partial equilibrium assumption for chemically reacting systems, *J. Comput. Phys.*, vol. **206**(2), pp. 395–411, 2005.

DeVolder, B., Glimm, J., Grove, J. W., Kang, Y., Lee, Y., Pao, K., Sharp, D. H., and Ye, K., Uncertainty quantification for multiscale simulations, *J. Fluids Eng.*, vol. **124**, pp. 29–41, 2002.

Eldred, M. and Burkardt, J., Comparison of non-intrusive polynomial chaos and stochastic collocation methods for uncertainty quantification, in *47th AIAA Aerospace Sciences Meeting*, Orlando, FL, 2009.

Fish, J. and Yuan, Z., N-scale model reduction theory, in *Bridging the Scales in Science and Engineering*, J. Fish, Ed., New York: Oxford University Press, 2009.

Ganapathysubramanian, B. and Zabaras, N., Sparse grid collocation schemes for stochastic natural convection problems, *J. Comput. Phys.*, vol. **225**, pp. 652–685, 2007.

Ganapathysubramanian, B. and Zabaras, N., Modeling multiscale diffusion processes in random heterogeneous media, *Comput. Methods Appl. Mech. Eng.*, vol. **197**(43–44), pp. 3560–3573, 2008.

Gerstner, T. and Griebel, M., Numerical integration using sparse grids, *Numer. Algorithms*, vol. **18**, pp. 209–232, 1998.

Ghanem, R. G. and Spanos, P. D., *Stochastic Finite Elements—A Spectral Approach*, Rev. ed., Dover Publications, 2003.

Griebel, M., Adaptive sparse grid multilevel methods for elliptic PDEs based on finite differences, *Computing*, vol. **6**, pp. 151–179, 1998.

Iman, R. L. and Conover, W. J., Small sample sensitivity analysis techniques for computer models with an application to risk assessment, *Commun. Statist.*, vol. **A9**, pp. 1749–1842, 1980.

Klimke, W. A., *Uncertainty Modeling Using Fuzzy Arithmetic and Sparse Grids*, PhD Thesis, University Stuttgart, 2005.

Mathelin, L. and Hussaini, M. Y., A stochastic collocation algorithm for uncertainty analysis, NASA Langley Research Center, Tech. Report NASA/CR-2003–212153, 2003.

Oskay, C. and Fish, J., Eigendeformation-based reduced order homogenization, *Comput. Methods Appl. Mech. Eng.*, vol. **196**, pp. 1216–1243, 2007.

Shi, J. and Ghanem, R., A stochastic nonlocal model for materials with multiscale behavior, *Int. J. Multiscale Comput. Eng.*, vol. **4**(4), pp. 501–519, 2006.

Smolyak, S. A., Quadrature and integration formulas for tensor products of certain classes of functions, *Soviet Math. Dokl.*, vol. **4**, pp. 240–243, 1963.

Walters, R. W., Towards stochastic fluid mechanics via polynomial chaos, in *41st AIAA Aerospace Sciences Meeting and Exhibit*, Reno, NV, 2003.

Wu, W., *Nonintrusive Stochastic Multsicale Design System*, PhD Thesis, Rensselaer Polytechnic Institute, 2010.

Xiu, D. and Karniadakis, G. E., The Wiener–Askey polynomial chaos for stochastic differential equations, *SIAM J. Sci. Comput.*, vol. **24**(2), pp. 619–644, 2002.

Xu, X. F., A multiscale stochastic finite element method on elliptic problems involving uncertainties, *Comput. Methods Appl. Mech. Eng.*, vol. **196**, pp. 2723–2736, 2007.

Yuan, Z. and Fish, J., Multiple scale Eigendeformation-based reduced order homogenization, *Comput. Methods Appl. Mech. Eng.*, vol. **198**, pp. 2016–2038, 2009.

Journal for Multiscale Computational Engineering 8(6), 561–584 (2010)

TAILORING CRYSTALLINITY AND NANOMECHANICAL PROPERTIES OF CLAY POLYMER NANOCOMPOSITES: A MOLECULAR DYNAMICS STUDY

Debashis Sikdar, Dinesh R. Katti, Kalpana S. Katti,* & Rahul Bhowmik

Department of Civil Engineering, North Dakota State University, Fargo, ND 58105, USA

*Address all correspondence to Kalpana S. Katti E-mail: Kalpana.Katti@ndsu.edu

Polymer clay nanocomposites (PCNs) synthesized using different organic modifiers show enhanced nanomechanical properties and difference in percentage crystallinity of polymer in the PCN. It appears that organic modifiers have an influence on the nanomechanical properties and crystallinity of PCNs. Tailoring crystallinity and nanomechanical properties of PCNs to required mechanical behavior of PCN is a promising technology. In addition, this is essential for robust multiscale modeling of nanocomposites through a hierarchical modeling approach, wherein nanomechanical behavior from experiments and molecular simulations are incorporated into finite element models. To evaluate the influence of molecular structure of organic modifiers on the crystallinity and nanomechanical properties of PCN, five organic modifiers have been selected in this study in such a way that either they have identical end functional groups but different backbone chain lengths or identical backbone chain length with different functional groups. The PCNs synthesized with the same polymer (polyamide 6) and clay (sodium montmorillonite) but different organic modifiers show significant difference in the crystallinity and nanomechanical properties. In this work molecular models of PCNs based on these organic modifiers have been built and interaction energies between different constituents of PCNs have been evaluated using molecular dynamics simulation. By comparing the interaction energies with experimental results, important insight is obtained regarding the crystallinity and nanomechanical properties of PCNs. It is observed that interactions between the polymer and the organic modifier are key to controlling the nanomechanical properties of PCNs, and by varying the backbone chain length of the organic modifiers, the nanomechanical properties and crystallinity of a particular polymer-based PCN can be tailored to a significant extent. Also by changing the functional groups of modifiers, the crystallinity and nanomechanical properties of PCNs can be altered.

KEY WORDS: *polymer-clay nanocomposite, molecular dynamics, molecular modeling*

1. INTRODUCTION

Polymer clay nanocomposites (PCNs) show enhanced mechanical (Okada et al., 1990; Ray and Okamoto, 2003; Ma et al., 2003; Vaia et al., 2002; Sikdar et al., 2007) and thermal properties (Hsueh and Chen, 2003; Zhang and Wilkie, 2003; Meneghetti and Qutubuddin, 2006) in comparison to pristine polymer. However, the mechanism for enhancement of physical properties (mechanical or thermal) of PCNs in comparison to pristine polymer is not well understood. This knowledge is important for tailoring the properties of PCNs into desired specification. Since the development of PCN in 1990 by Toyota Research Laboratory, almost all common varieties of polymer have been undertaken by the researchers for synthesis of PCNs (Ray and Okamoto, 2003). Sodium montmorillonite (MMT) is most commonly used as clay for synthesis of PCN, which is hydrophilic in nature. To enhance the miscibility of hydrophobic polymer with MMT, organic modifiers are usually used for treating MMT, which transforms MMT from hydrophilic into hydrophobic and organically modified montmorillonite (OMMT) is obtained. Hence it appears that the primary function of organic modifiers is to enhance the miscibility of hy-

1543–1649/10/$35.00

drophilic MMT with hydrophobic polymer. From our previous work (Sikdar et al., 2007) it is found that PCNs synthesized with the same polymer and MMT but with three different organic modifiers results in different elastic modulus and dynamic mechanical properties in the nanometer length scale. Ma et al. (2003) in a separate work showed that PCNs synthesized with the same set of polymers (polyamide 6), clay, and three different organic modifiers resulted in different improvements of bulk scale properties (mechanical and thermal) in comparison to pristine polymer. Thus, in addition to the enhancement of miscibility of hydrophilic clay with hydrophobic polymer, organic modifiers have a significant role in the enhancement of physical properties of PCNs. In our previous work (Sikdar et al., 2008b) multiscale modeling of PCNs was carried out using steered molecular dynamics, atomic force microscopy imaging, nanoindentation, and finite element analysis. Our previous work indicates that there exists an altered phase region in the polymer around individual clay particles resulting from nonbonded interactions (van der Waals, electrostatic interactions) of about 250 Å (Sikdar et al., 2008b). Thus, in PCNs, where nanosized clay particles are uniformly dispersed, a significant volume of polymer is influenced by clay. Hence, the enhanced (altered) mechanical behavior of polymers, as a result of molecular interactions between different constituents (clay–modifier–polymer), is key to modeling the mechanical behavior of PCNs. Based on this multiscale approach, we vary molecular interactions by changing both the length and functional group of the modifier, since the multiscale approach clearly indicates the large impact of the molecular interactions on macroscale properties. Researchers have also used Monte Carlo methods to model inclusions as spherical entities and studied the interactions between inclusions and polymers, as well as physical characteristics of the polymer (Dionne et al., 2005, 2006).

Our previous molecular dynamics study (Sikdar et al., 2008a) shows that in the crystallinity and enhancement of nanomechanical properties of PCNs, interactions between polymers and modifiers are the key. The study further showed that backbone chains as well as functional groups of organic modifiers both have a specific role with regard to crystallinity and enhancement of nanomechanical properties of PCNs. However, knowledge regarding controlling the crystallinity and nanomechanical properties of particular polymer-based PCNs and the influence of organic modifiers on the structure and nanomechanical properties of PCNs is not well understood. Molecular dynamics (MD) is a useful technique for studying structure, dynamics and interactions between different constituents of PCNs (Vaia et al., 2002; Ginzburg et al., 2000; Vaia and Giannelis, 1997). Thus, in this work to address the issues regarding tailoring the structure and nanomechanical properties of PCNs and the influence of organic modifiers on the structure and nanomechanical properties of PCNs, using MD, we have studied interactions between the constituents of typical PCNs synthesized with identical polymer (polyamide 6) and clay (sodium montmorillonite) but different organic modifiers. Our previous work using multiscale modeling and experiments (Sikdar et al., 2008b, 2009) has clearly shown the role of molecular interactions between clay–modifier–polymer systems on altering the polymer and clay phases to a very large extent, thus significantly impacting the mechanical properties. In this work, we further investigate the effectiveness of this concept by changing the clay–polymer–modifier interactions by varying the modifier chain length and functional group.

In this work, for constructing the molecular model of polyamide 6 (PA6)–based PCNs, we have chosen five typical organic modifiers (n-dodecylamine, hexadecylamine, octadecylamine, dodecyl trimethyl ammonium bromide, and hexadecyl trimethyl ammonium bromide), similar to those of our previous experimental work (Sikdar et al., 2009). For the convenience of representation, the organic modifiers in this work have been named dodecyl, hexadecyl, octadecyl, dodecyl-Br, and hexadecyl-Br, respectively. The molecule of organic modifier has two parts in its structure: (i) backbone chain and (*ii*) end functional groups. The molecular structure of organic modifiers showing backbone chain length and end functional groups is given in Table 1(a). To evaluate the influence of organic modifiers on the crystallinity and nanomechanical behavior of PCNs more precisely, we have grouped the modifiers into two different sets as follows: (i) in the first set only the backbone chain length of modifiers varies, keeping the end functional group the same as shown in Table 1(b), and (*ii*) in the second set, only one end functional group of modifier varies, keeping the backbone chain identical as shown in Table 1(c).

The properties of composites are largely influenced by the interactions between constituents (Sikdar et al., 2009). Interaction energy is a measure of interactions between different constituents of PCNs. Hence, in this paper, using MD, we have constructed the representative molecular model of five different PCNs and have calculated interaction energies between different constituents of PCNs in order to evaluate interactions between different constituents of PCNs. By comparing the results ob-

TABLE 1(a): Molecular structure of organic modifiers showing backbone chain length, end functional group, and partial charges on the atoms of the amine functional group.

Organic modifiers	Backbone	Functional groups		Partial charges of atoms of amine functional groups		
				N	C	H
Dodecyl	$(CH_2)_{11}$	(CH_3)	(NH_3)	-0.051	-	+0.176
Dodecyl-Br	$(CH_2)_{11}$	(CH_3)	$N(CH_3)_3$	+0.206	-0.285	+0.133
Hexadecyl	$(CH_2)_{15}$	(CH_3)	(NH_3)	-0.193	-	+0.235
Hexadecyl-Br	$(CH_2)_{15}$	(CH_3)	$N(CH_3)_3$	-0.055	-0.180	+0.113
Octadecyl	$(CH_2)_{17}$	(CH_3)	(NH_3)	-0.204	-	+0.227

TABLE 1(b): Comparison of the molecular structure of organic modifiers with increasing backbone chain length.

Organic modifiers	Backbone	Functional groups	
Dodecyl	$(CH_2)_{11}$	(CH_3)	(NH_3)
Hexadecyl	$(CH_2)_{15}$	(CH_3)	(NH_3)
Octadecyl	$(CH_2)_{17}$	(CH_3)	(NH_3)

TABLE 1(c): Comparison of molecular structure of organic modifiers with identical backbone but different functional groups.

Organic modifiers	Backbone	Functional groups	
Dodecyl-Br	$(CH_2)_{11}$	(CH_3)	$N(CH_3)_3$
Dodecyl	$(CH_2)_{11}$	(CH_3)	(NH_3)
Hexadecyl-Br	$(CH_2)_{15}$	(CH_3)	$N(CH_3)_3$
Hexadecyl	$(CH_2)_{15}$	(CH_3)	(NH_3)

tained from MD simulations of these PCNs with the crystallinity and nanomechanical properties of the same set of PCNs obtained from previous experimental work (Sikdar et al., 2009), we get valuable information about the role of organic modifiers with regard to the structure and nanomechanical properties of PCNs. Our study further shows that through the selection of an appropriate organic modifier, the structure and nanomechanical properties of PCNs containing specific polymers can be tailored to a significant extent by controlling interactions between the constituents of PCNs.

2. COMPUTATIONAL METHODOLOGY

The polymer and clay used for synthesis of PCNs are polyamide 6 (PA6) and MMT, respectively. The organically modified montmorillonite (OMMTs) synthesized with organic modifiers dodecyl, hexadecyl, octadecyl, dodecyl-Br, and hexadecyl-Br are named in this work OMMT-dodecyl, OMMT-hexadecyl, OMMT-octadecyl, OMMT-dodecyl-Br, and OMMT-hexadecyl-Br, respectively, and PCNs synthesized using organically modified montmorillonite OMMT-dodecyl, OMMT-hexadecyl, OMMT-octadecyl, OMMT-dodecyl-Br, and OMMT-hexadecyl-Br are named PCN-dodecyl, PCN-hexadecyl, PCN-octadecyl, PCN-dodecyl-Br, and PCN-hexadecyl-Br, respectively. By comparing the results obtained from PCN-dodecyl, PCN-hexadecyl, and PCN-octadecyl, the effect of the backbone chain of the modifier on the crystallinity and nanomechanical behavior of PCNs can be obtained. By comparing the results of PCN-dodecyl with PCN-dodecyl-Br, and PCN-hexadecyl with PCN-hexadecyl-Br, the effect of the functional group of the modifier on the crystallinity and nanomechanical behavior of the PCNs can be obtained.

The structure of the polymer, clay, and organic modifiers used in this paper were constructed using the module Builder^{TM} of InsightII 2005 of Biosym Technologies, Inc. (San Diego, CA, USA). The force field parameters used in polymer and organic modifiers were obtained from CHARMm 27 (Brooks et al., 1983). For the atoms of the polymer, the standard partial charges obtained from the library of CHARMm 27 were used. The partial charges on the polymer atoms are shown in Fig. 1. The chemical structure of a unit cell of isomorphically ion substituted MMT is $[NaSi_{16}(Al_6FeMg)O_{40}(OH)_8]$. In the MMT unit cell, an aluminum octahedral layer is sandwiched between two silica tetrahedra layer. The coordinates of atoms lying in the MMT unit cell were obtained from the work of Skipper et al. (1995a, 1995b). The partial charges on the atoms of the MMT unit cell were obtained from the work of Teppen et al. (1997). In our earlier work (Katti et al., 2005), the CHARMm force field parameters of MMT were derived using the standard parameters of clay in consistent force field (CFF) and those derived parameters were used in the present work for clay. The molecular structure of the polymer and organic modifiers was minimized initially using InsightII. Using these energy-minimized structures of polymer and organic modifiers, the initial models of OMMT and PCN were constructed using visual molecular dynamics (VMD) (Humphrey et al., 1996). The synthesis procedure of different OMMTs and PCNs is described in our earlier work (Sikdar et al., 2007, 2009; Katti et al., 2006).

3. CALCULATION OF PARTIAL CHARGES ON THE ATOMS OF ORGANIC MODIFIERS USING THE AB INITIO METHOD

Ab initio calculations were conducted using the quantum chemistry program Gaussian98 (Frisch et al., 1995) in order to calculate the charges on the atoms of the molecules of organic modifiers used for synthesizing organically modified montmorillonite and polymer clay nanocomposites. The structures used for the charge calculations were dodecylamine, hexadecylamine, and octadecylamine with hydrochloric acid (HCl), and dodecylamine and hexadecylamine with tri methyl bromide. All the structures were first minimized with the Hartree–Fock method with 6–31 G** basis set (HF/6–31 G**). After minimization, the first three structures with HCl form protonated dodecylamine, hexadecylamine, and octadecylamine, whereas the last two structures form dodecyl trimethyl ammonium and hexadecyl trimethyl ammonium. The final minimized structures of organic modifiers are shown in Fig. 2, which shows that organic modifiers maintain almost linear structure. Snapshots of the end functional group (amine and trimethyl amine) of octadecylamine and hexadecyl trimethyl ammonium bromide before and after minimization are shown in Fig. 3. From Figs. 2 and 3 it is observed that dodecyl, hexadecyl, and octadecyl form $(R–NH_3)^+Cl^-$, whereas dodecyl-Br and hexadecyl-Br form $[R–N(CH_3)_3]^+Br^-$. Here R represents the alkyl groups which depend upon the starting molecular structures of organic modifiers.

The atom-centered charges were calculated using Merz–Singh–Kollman method (Singh and Kollman, 1984; Besler et al., 1990). In this method, atomic charges are fitted to reproduce the molecular electrostatic potential at several points around the calculated molecule. The atomic charges are calculated in such a way that the total charge equals the molecular charge. In our work, the overall charge on a molecule of each organic modifier was considered as 0. The Merz–Singh–Kollman method has been used with B3LYP/cc-pVDZ electric potential. The schematic diagrams of the organic modifiers are shown in Fig. 4. The partial charges on the atoms of organic modi-

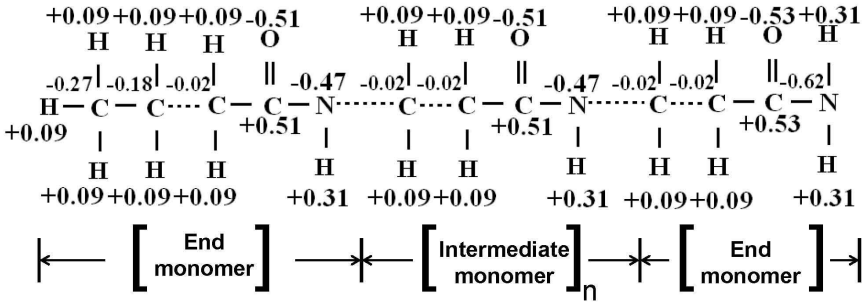

FIG. 1: Partial charges on the atoms of a polymer (polyamide 6).

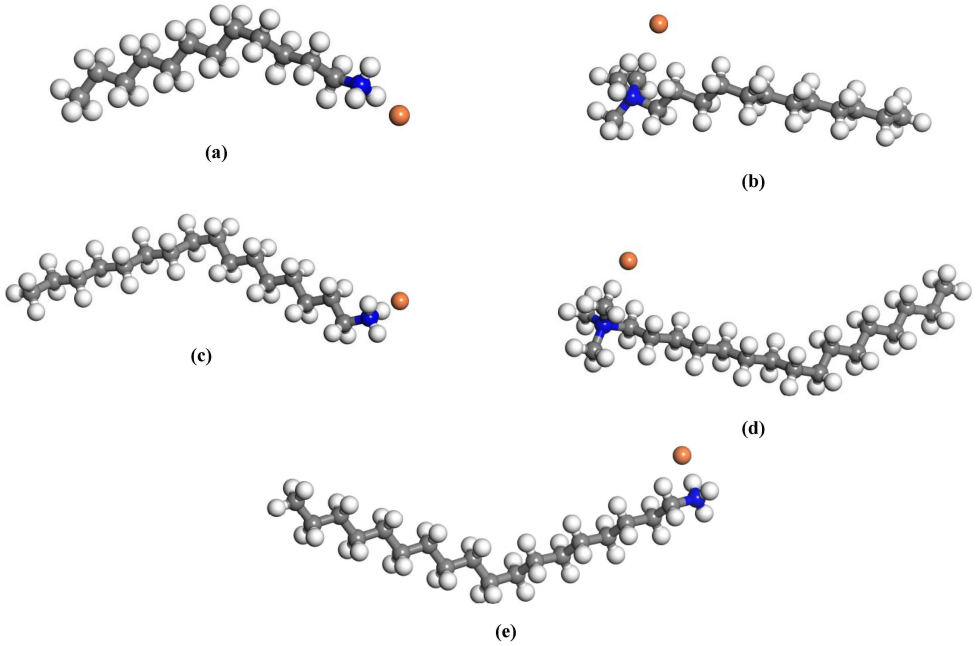

FIG. 2: Snapshots showing minimized structures of different organic modifiers: **(a)** n-dodecylamine, **(b)** dodecyl trimethyl ammonium bromide, **(c)** n-hexadecylamine, **(d)** hexadecyl trimethyl ammonium bromide, **(e)** n-octadecylamine (C = grey, H = white, N = blue, orange = Cl/Br).

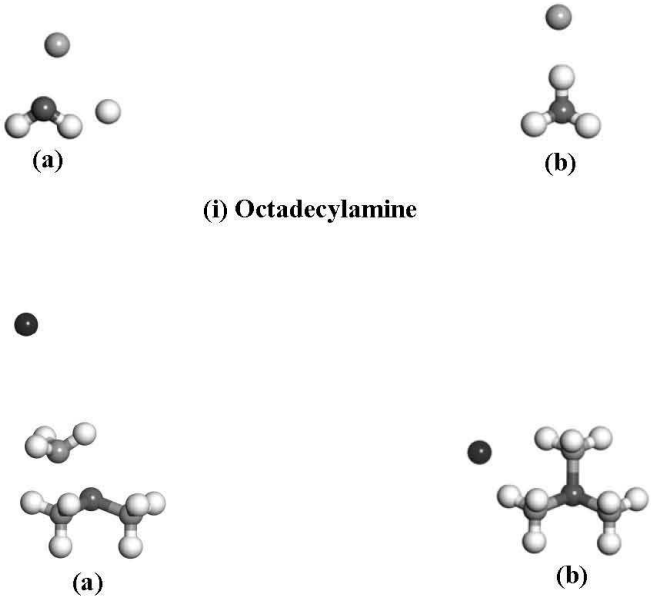

FIG. 3: The amine groups in the molecules of octadecylamine and hexadecyl trimethyl ammonium bromide **(a)** before minimization and **(b)** after minimization. (For (i): N = black, H = white, Cl = gray. For (ii): N = dark gray, C = light gray, Br = black, H = white.)

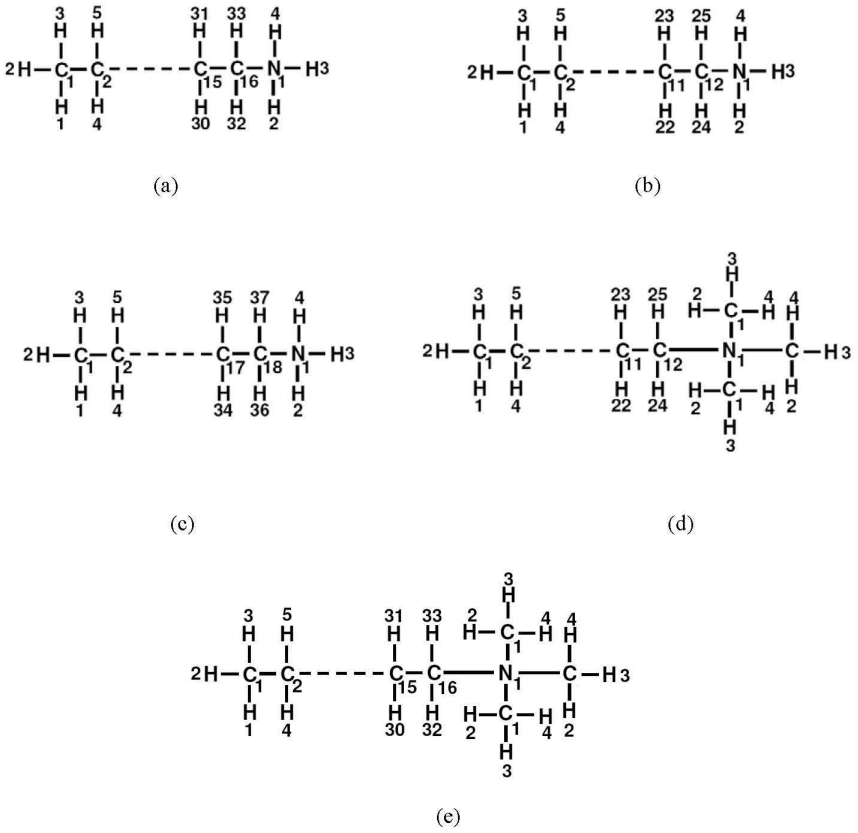

FIG. 4: Schematic diagrams showing the molecular structure of different organic modifiers: **(a)** n-dodecylamine, **(b)** hexadecylamine, **(c)** octadecylamine, **(d)** dodecyl trimethyl ammonium bromide, and **(e)** hexadecyl trimethyl ammonium bromide.

fiers are shown in Table 2. The serial number of different atoms (C, H, and N) of modifiers used in Table 2 were taken from the atom serial as shown in the schematic diagram of modifiers in Fig. 4. From ab initio charge calculation, the net partial charge on the molecule of protonated organic modifiers was found to be +0.70 in all the cases.

4. SIMULATION DETAILS OF THE OMMT AND PCN MODELS

Molecular dynamics (MD) software, NAMD 2.5 (**Kalé** et al., 1999), was used for conducting MD of OMMT and PCN. The Varlet algorithm was applied for running MD. The isothermal-isobaric ensemble, constant number, pressure, and temperature (NPT) simulation was used in the MD simulation. For van der Waals interaction, switch and cutoff distances applied were 20 and 22 Å, respectively, in all OMMT and PCN models. The particle mesh Ewald simulation method was used for electrostatic interactions between the atoms of OMMT and PCN models (Karasawa and Goddard, 1989). The Nose'–Hoover Langevin piston and Langevin dynamics were used in the simulation for controlling model pressure and temperature, respectively (Martyna et al., 1994; Feller et al., 1995). A time step of 0.5 femtosecond was used in the simulation. The change of temperature during MD simulation was maintained following the synthesis route of OMMT and PCN. For OMMT, first, the model is minimized for a duration of 5 picoseconds (ps) (10^{-12} second) at 0 K temperature and 0 bar pressure. Then MD of OMMT was conducted by increasing the temperature of the system to 300 K while keeping the pressure at 0 bar. By keeping the temperature at 300 K, the pressure of the system increased to 1 atmospheric (1.013 bar) pressure in four equal steps in order to bring the temperature and pressure of the OMMT model to ambient con-

TABLE 2: The partial charge on each atom of different organic modifier molecules (here numbering of different atoms of modifiers is taken from Fig. 4).

Atom type	**Partial charge on the atoms of different organic modifier molecules**				
Terminal and backbone carbon atoms	n-Dodecyl amine	Hexadecylamine	Octadecylamine	Dodecyl trimethyl ammonium bromide	Hexadecyl trimethyl ammonium bromide
C1	-0.212	-0.200	-0.210	-0.203	-0.228
C2	+0.186	+0.179	+0.191	+0.182	+0.175
C3	-0.004	+0.002	+0.029	+0.003	+0.044
C4	+0.012	-0.017	-0.008	+0.016	-0.069
C5	+0.081	+0.129	+0.072	+0.061	+0.201
C6	-0.004	-0.049	+0.078	+0.006	-0.090
C7	+0.066	+0.046	+0.027	+0.028	+0.061
C8	-0.110	-0.018	+0.000	+0.040	-0.028
C9	-0.027	-0.030	+0.085	-0.002	-0.050
C10	+0.148	+0.074	-0.047	-0.108	+0.078
C11	-0.177	-0.019	-0.029	+0.204	-0.063
C12	+0.167	+0.027	+0.074	-0.174	+0.061
C13		+0.099	-0.052		+0.044
C14		-0.101	+0.028		+0.066
C15		+0.131	+0.121		-0.239
C16		-0.057	-0.111		+0.354
C17			+0.152		
C18			-0.055		
Backbone hydrogen atoms					
H4	-0.038	-0.036	-0.041	-0.041	-0.035
H5	-0.038	-0.037	-0.042	-0.038	-0.036
H6	-0.007	-0.010	-0.016	-0.011	-0.019
H7	-0.007	-0.007	-0.016	-0.008	-0.015
H8	-0.016	-0.010	-0.015	-0.018	-0.004
H9	-0.016	-0.010	-0.016	-0.016	-0.004
H10	-0.023	-0.033	-0.030	-0.022	-0.046
H11	-0.030	-0.038	-0.025	-0.021	-0.054
H12	-0.005	+0.002	-0.027	-0.014	+0.008
H13	-0.004	+0.004	-0.028	-0.003	+0.009
H14	-0.017	-0.014	-0.016	-0.019	-0.015
H15	-0.005	-0.002	-0.023	0.000	-0.015
H16	+0.026	+0.003	-0.011	-0.017	0.006
H17	+0.032	+0.004	-0.009	-0.012	+0.008
H18	+0.018	+0.002	-0.027	+0.032	+0.011
H19	+0.014	+0.005	-0.008	0.000	+0.069
H20	-0.023	-0.024	-0.006	+0.032	-0.013
H21	-0.005	-0.006	+0.008	+0.012	-0.004
H22	+0.022	-0.003	+0.007	-0.002	+0.008
H23	+0.022	-0.001	+0.004	-0.029	+0.004

TABLE 2: (Continued) The partial charge on each atom of different organic modifier molecules (here numbering of different atoms of modifiers is taken from Fig. 4).

Atom type	**Partial charge on the atoms of different organic modifier molecules**				
Backbone hydrogen atoms	n-Dodecyl amine	Hexadecylamine	Octadecylamine	Dodecyl trimethyl ammonium bromide	Hexadecyl trimethyl ammonium bromide
H24	+0.036	-0.012	-0.015	+0.082	-0.010
H25	+0.029	-0.014	-0.006	+0.094	-0.025
H26		-0.031	+0.004		-0.017
H27		-0.003	+0.006		-0.010
H28		+0.031	-0.018		-0.018
H29		+0.009	-0.005		+0.027
H30		-0.007	-0.035		+0.094
H31		-0.002	-0.009		+0.037
H32		+0.100	+0.011		+0.021
H33		+0.042	+0.027		-0.093
H34			-0.005		
H35			-0.016		
H36			+0.041		
H37			+0.099		
Methyl hydrogen atoms					
H1	+0.044	+0.040	+0.041	+0.041	+0.047
H2	+0.044	+0.040	+0.041	+0.041	+0.047
H3	+0.044	+0.040	+0.041	+0.041	+0.047
Nitrogen atom (N1)	-0.051	-0.193	-0.204	+0.206	-0.055
Hydrogen atoms of protonated amine group					
H1	+0.175	+0.220	+0.223		
H2	+0.175	+0.220	+0.223		
H3	+0.175	+0.220	+0.223		
Trimethyl amine group atoms					
C				+0.285	-0.180
H2				+0.136	+0.113
H3				+0.136	+0.113
H4				+0.136	+0.113

dition. In the final heating cycle, by keeping the pressure at 1 atmosphere, the temperature of the OMMT model was further raised to 313 K and was subsequently lowered to 300 K. In each step of temperature and pressure change, the simulation was run for 25 ps. To equilibrate the OMMT model, the model was run for a duration of 200 ps at room temperature and pressure. The energy versus time plot of the OMMT model shows that the simulation time of 200 ps is sufficient to equilibrate the model. Keeping z-direction movement of MMT free from externally applied constraint, a force-constraint of 1 Kcal/mol-Å was applied to all the atoms of MMT in the x and y di-

rections. No constraining force was applied on the atoms of organic modifiers.

The simulation procedure of the PCN model was done following the synthesis route of PCNs as described in our previous work (Sikdar et al., 2007, 2009; Katti et al., 2006). The variation of temperature and pressure in the PCN model is similar to the OMMT model except the maximum temperature which is used in the simulation of the PCN model is 300 K, following its synthesis route. MD simulation is started for the PCN model with energy minimization at 0 bar pressure, and 0 K temperature. In the beginning, keeping the pressure at 0 bar, the temperature of the model is increased to 300 K, followed by increasing the pressure to 1 atmospheric level in four equal steps, keeping the temperature constant at 300 K. In each step of change in pressure and temperature during simulation of the PCN models, MD simulation is run for a duration of 25 ps. Finally, the whole PCN model is run for a duration of 200 ps to equilibrate the model. As before, the energy versus time plot shows that the 200 ps duration of simulation is sufficient for convergence of energy of the PCN model. Similar to the OMMT model, a force constraint of 1 Kcal/mol- Å is applied to all the atoms of MMT only in the x and y axis directions. The atoms of polymer and organic modifiers are kept free from any constraint in all directions. Additional details about the computational methodology and simulation procedure can be found in our earlier work (Sikdar et al., 2006a, 2006b, 2008).

4.1 Model of Organically Modified Montmorillonite (OMMT)

By comparing the experimental (X-ray diffraction [XRD] and photoacoustic Fourier transform infrared spectroscopy [PA-FTIR]) and modeling (d-spacing and minimum energy conformation) results, the OMMT models were formed. The construction details of the OMMTs are given in our earlier work (Sikdar et al., 2006a, 2008a). In the intercalated OMMT model there are two layers of clay. In each layer of clay, 18 unit cells of MMT are periodically replicated, out of which 6 unit cells are in the x direction and 3 are in the y direction. The net charge of each layer of clay is -9. The net charge for each molecule of organic modifiers found from ab initio calculation is +0.70. To make the whole OMMT model charge neutral, we placed 13 organic modifiers in the interlayer clay gallery of the OMMT model. From our earlier MD study (Katti et al., 2006; Sikdar et al., 2006b) it was found that orientation of organic modifiers is parallel to the clay gallery. Therefore, in our model the organic modifiers are initially placed parallel to the clay gallery. From the PA-FTIR study (Sikdar et al., 2009; Katti et al., 2006), it was found that organic modifiers have only nonbonded interactions with clay in the OMMT, and therefore no bond is formed between the clay and the modifier in OMMT models. The PA-FTIR study of OMMT shows that there are no water molecules in the OMMT interlayer (Katti et al., 2006; Sikdar et al., 2008c) and hence, no water molecules are incorporated in our initial OMMT model. The OMMT model is periodically replicated in the x, y, and z direction by applying periodic boundary conditions to replicate the periodic structure of clay in all directions. The initial d-spacings of OMMT models are selected as described in our earlier work (Sikdar et al., 2006a). For obtaining the final OMMT model, the MD simulation of the initial OMMT model is conducted following the synthesis route of OMMT (Sikdar et al., 2007; Katti et al., 2006). The following conditions were applied for selecting a representative OMMT model (Sikdar et al., 2006a, 2008b):

(1) The final d-spacing of OMMT models obtained after running MD simulations matches with experimentally observed d-spacing of respective OMMT obtained from XRD results.

(2) The OMMT model satisfies the minimum energy conformation.

The final models of OMMT-octadecyl and OMMT-hexadecyl-Br obtained after applying these above two criteria are shown in Fig. 5. The d-spacings of the final models of OMMTs obtained from XRD and MD simulation are shown in Table 3, showing good agreement in terms of d-spacing between modeling and experimental results.

4.2 Model of Polymer Clay Nanocomposites (PCNs)

The PCN models were constructed by comparing the results obtained from experiments (XRD and PA-FTIR) and MD simulation, as done in our earlier work (Sikdar et al., 2006a). A globally minimized polymer structure was obtained by annealing the polymer at high temperature (700 K), as described in detail in our previous work (Sikdar et al., 2006a). The initial models of PCNs containing five different OMMTs were constructed by inserting the annealed polymer chains inside the interlayer clay gallery of the final model of the respective OMMT.

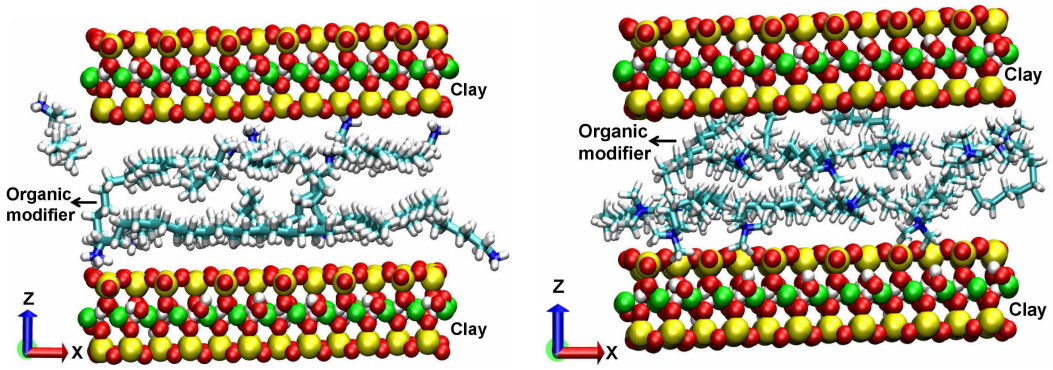

(a) (b)

FIG. 5: Molecular model of OMMT showing organic modifiers intercalated inside the interlayer clay gallery: **(a)** OMMT-octadecyl and **(b)** OMMT-hexadecyl-Br. Clay is in VDW rendering form and the organic modifier is in licorice rendering form.

TABLE 3: d-Spacing of OMMTs obtained from XRD and MD simulation.

OMMT Sample	d-spacing from XRD (Å)	d-spacing from MD simulation (Å)
OMMT–dodecyl	14.18	14.78
OMMT–dodecyl-Br	15.46	15.70
OMMT–hexadecyl	20.63	20.56
OMMT–hexadecyl-Br	18.55	19.30
OMMT–octadecyl	22.29	21.87

PA-FTIR study of PCNs showed that there are only nonbonded interactions between the different constituents of PCNs, and hence, in the PCN model no bond is between clay, organic modifier, or polymer. For obtaining the final OMMT model, the following conditions were applied, similar to the previous work (Sikdar et al., 2006a):

(1) The energy-minimized conformation of the annealed polymer fits perfectly in the interlayer clay spacing of the final OMMT model while making the initial PCN model.

(2) The final d-spacing of the PCN model obtained from MD simulation matches with the d-spacing of the PCN sample observed from XRD.

(3) The representative model of the PCN sample satisfies the minimum energy conformation.

The PCN model which has the largest polymer chain in the interlayer clay gallery and satisfies the above three conditions is considered the representative intercalated PCN model. Similar to OMMT models, the PCN models are replicated in the x, y, and z direction to replicate the periodic structure of clay in all directions. The size of the PCN model in the x and y directions is 33.55 and 28.902 Å, respectively, and the cellBasisVector applied to the simulation in the x and y directions is 40 and 34 Å, respectively. The cellBasisVector of the PCN models in the z direction is kept twice the d-spacing of the respective initial PCN model. For Van der Waals interaction, the switch and cutoff distance used for the models are 14 and 16 Å, respectively. The representative molecular models of PCN-octadecyl and PCN-hexadecyl-Br obtained after MD simulation are shown in Fig. 6. The representative model of PCN-dodecyl and PCN-dodecyl-Br contain an 8-monomer chain intercalated polymer, whereas the representative model of PCN-hexadecyl and PCN-hexadecyl-Br contains a 12-monomer-chain polymer. The largest polymer chain is found in the representative model of PCN-octadecyl, the length of which is 18 monomers long. The final models of PCNs are used for studying the interactions between different constituents of PCNs. The d-spacing of PCNs obtained from modeling and XRD

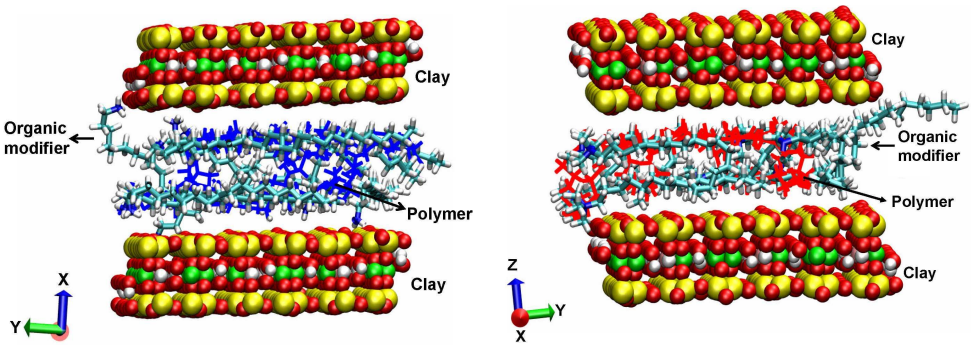

(a) (b)

FIG. 6: The molecular model of polymer clay nanocomposites showing polymer and organic modifiers intercalated inside the interlayer clay gallery: **(a)** PCN-octadecyl and **(b)** PCN-hexadecyl-Br. Clay is in VDW rendering form, polymer is in line rendering form, and the organic modifier is in licorice rendering form.

TABLE 4: d-Spacing of PCNs obtained from XRD and MD simulation.

PCN Sample	d-spacing from XRD (Å)	d-spacing from MD simulation (Å)
PCN–dodecyl	14.52	14.62
PCN–dodecyl-Br	14.08	15.49
PCN–hexadecyl	17.48	19.68
PCN–hexadecyl-Br	17.35	18.36
PCN–octadecyl	18.06	20.77

are given in Table 4, which shows good agreement between the modeling and experimental results. From literature (Zin et al., 2005; Mitsunaga et al., 2003) it is seen that the d-spacing of PCN can be smaller than that of OMMT. Furthermore, from modulus mapping experiments the elastic modulus of PCNs are found significantly higher than that of pristine polymer in nanometer length scale, and the crystallinity percent of PCN is found to be significantly lower than that of pure polymer (Sikdar et al., 2009). The significant improvement of nanomechanical properties and reduction in crystallinity % of PCN in comparison to pristine polymer indicates the formation of polymer clay nanocomposite. Transformation of the crystalline form of polymer from α-crystalline form in pure polymer into γ-crystalline form in PCN is also indicative of formation of PCN (Vaia et al., 2002).

5. CALCULATION OF INTERACTION ENERGY

MDEnergy^{TM} of NAMD was used for studying interaction energies between different constituents of PCNs. The trajectory file of the whole molecular model is directly obtained from MD simulation. The interaction energies of any given set of atoms or between two given sets of atoms for a particular time span can be calculated using the trajectory file of the molecular system knowing their structural information, interaction parameters, cutoff, and switch distance. The interaction energies for any molecular system can be calculated for bonded and nonbonded energies separately. Furthermore, the bonded energy terms include bond, angle, and dihedral energies corresponding to the atoms under consideration within the molecular system. Similarly, the nonbonded energy can be calculated in the van der Waals category and electrostatic energies for any given set of atoms or between two sets of interacting atoms. To equilibrate the models, MD simulations of all OMMT and PCN models were run for a duration of 200 ps in the final stage, and the average of results for the last 25 ps was considered for calculating the interaction energy of the molecular models.

6. RESULTS AND DISCUSSION

The properties of the composites largely depend on the interactions between constituents (Brooks et al., 1983). Interaction energies are the measure of interactions between

different constituents of composites. The negative energy indicates attractive interaction, and positive energy represents repulsive interaction between two constituents of composites. To estimate the interactions between different constituents of composites, the interaction energies between different constituents of PCNs were evaluated. The PCNs in this study were synthesized with the same polymer (PA6) and clay (MMT) but with five different organic modifiers. The organic modifiers are categorized into two types as mentioned earlier: (i) modifiers having identical functional groups but different lengths of backbone chain, a comparison of molecular structures of which is shown in Table 1(b), and (*ii*) modifiers having different end functional groups with the same backbone length, a comparison between the molecular structure of which is presented in Table 1(c). To study the effect of organic modifiers on the properties of PCN, the study was constructed in two ways: (i) comparing the results of simulation and experiments between the PCNs synthesized with modifiers containing different backbone chain lengths but identical end functional groups, and (*ii*) comparing simulation and experimental results between the PCNs synthesized with modifiers having different end functional groups but identical backbone chains. This comparison gives valuable insight regarding the influence of organic modifiers on the structure and nanomechanical properties of PCNs, and tailoring the structure and nanomechanical properties of particular polymer-based PCNs by selecting a certain type of organic modifier.

6.1 Effect of Modifier Backbone Chain Length on Crystallinity and the Elastic Modulus of PCNs

The crystallinity of PCNs was evaluated in our earlier work using differential scanning calorimetry (Sikdar et al., 2009). In the same study (Sikdar et al., 2009), the elastic modulus of PCNs in the nanometer length scale was evaluated using nanoindentation. To study the effect of organic modifiers on the crystallinity and nanomechanical properties of PCNs, the PCNs are synthesized in that work (Sikdar et al., 2009) with same polymer and clay but with different organic modifiers, similar to the set of modifiers used in our current MD work. The comparison of crystallinity and elastic modulus of PCNs synthesized with identical functional groups but varying backbone chain length are shown in Table 5. From Table 5 it is evident that with the increase of backbone chain length of modifiers, the crystallinity of PCNs decreases and the elastic modulus increases. Thus, it is evident from the results of Table 5 that for particular polymer- and clay-based PCNs, by changing the backbone chain length of the organic modifier, the nanoscale structure and nanomechanical properties of PCNs can be varied to a significant extent, and this gives important insight regarding tailoring the properties of particular PCNs. Fourier transform infrared spectroscopy of PCNs shows that there are only nonbonded interactions between different constituents of PCNs (Sikdar et al., 2009). MD simulation has been used to evaluate the nonbonded interactions between different constituents of PCNs and their probable correlations with the crystallinity and elastic modulus of PCNs.

6.2 Effect of Functional Group Modifier on PCN Crystallinity and Elastic Modulus

The crystallinity and elastic modulus of PCNs synthesized with organic modifiers having the same backbone chain but different end functional groups are shown in Table 6. Here also we observe that by changing the functional group from a protonated amine (N^+H_3) to trimethyl amine [$N^+(CH_3)_3$] the crystallinity of PCNs and elastic modulus changes, indicating the significant influence of the modifier's functional group on the crystallinity and elastic modulus of the PCN.

6.3 Interactions in PCN-Dodecyl

The interphasial nonbonded interactions between different constituents (polymer, clay, and organic modifiers)

TABLE 5: Effect of backbone chain length of the organic modifier on the crystallinity and elastic modulus of polyamide 6–based PCNs.

PCN Samples	Structural difference		% Crystallinity from DSC	E (GPa)
	Backbone	Functional group		
PCN-dodecyl	$(CH_2)_{11}$	NIL	27.78	4.77
PCN-hexadecyl	$(CH_2)_{15}$	NIL	20.81	4.81
PCN-octadecyl	$(CH_2)_{17}$	NIL	19.81	5.06

TABLE 6: Effect of functional group of organic modifier on the crystallinity and elastic modulus of polyamide 6–based PCNs.

PCN Samples	Structural difference		% Crystallinity from DSC	E (GPa)
	Backbone chain	Functional group		
PCN-dodecyl-Br	NIL	$N(CH_3)_3$	27.95	4.36
PCN-dodecyl	NIL	(NH_3)	27.78	4.77
PCN-hexadecyl-Br	NIL	$N(CH_3)_3$	28.05	4.84
PCN-hexadecyl	NIL	(NH_3)	20.81	4.81

in polymer clay nanocomposites synthesized with an organic modifier, n-dodecylamine, are shown in Fig. 7. The attractive interactions are represented by the solid line and the repulsive interactions are represented by the dotted line. The highest nonbonded interactions are observed between the clay and the organic modifier, -596 Kcal/mol, followed by interactions between the clay and the polymer (-193 Kcal/mol) and the polymer and the organic modifier (-85 Kcal/mol). From Fig. 7 it is further observed that the functional group as well as the backbone chain of the organic modifier both have significant attractive interactions with the clay. The contribution of interactions coming from the modifier backbone is even larger than the interactions coming from the functional group of modifiers. As seen from Table 2, although the partial charges on the atoms of the modifier backbone are much less than the partial charges on the atoms of the end functional group of the organic modifier, the larger number of atoms present in the backbone of the modifier makes their total contribution high. Between the clay and the polymer, major interactions are observed between the clay and backbone of the polymer, which is -123 Kcal/mol. There is relatively feeble interaction (-70 Kcal/mol) between the clay and the functional group of the polymer. Between the polymer and the organic modifiers, the functional group of polymer has attractive interactions with the functional group as well as the backbone of the organic modifiers, whereas the polymer backbone has repulsive interactions with the backbone and functional groups of the organic modifier. The largest attractive interactions between the polymer and the organic modifier are observed between the functional group of the polymer and organic modifier functional group, which is -98 Kcal/mol, followed by attractive interactions between the functional group of the polymer and the modifier backbone (-55 Kcal/mol). The largest repulsive interactions are observed between the polymer backbone and the modifier backbone ($+47$ Kcal/mol), followed by interactions between the polymer backbone and the functional group of organic modifiers ($+21$ Kcal/mol).

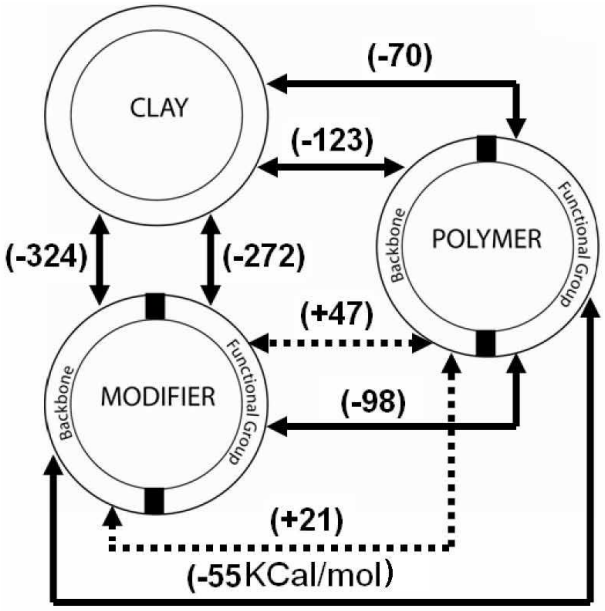

FIG. 7: Energy diagram showing nonbonded interaction energies between polymer, clay, and organic modifier in PCN synthesized with organic modifier, n-dodecylamine.

6.4 Interactions in PCN-Hexadecyl

The nonbonded interactions between different constituents of PCN-hexadecyl are shown in Fig. 8. Similar to PCN-dodecyl, the largest interactions between the different constituents are observed between the clay and the modifier (-600 Kcal/mol), followed by the clay and the polymer (-162 Kcal/mol), and the polymer and organic modifier (-156 Kcal/mol). For interactions between the clay and the organic modifier, the end functional group and backbone of organic modifiers both have significant

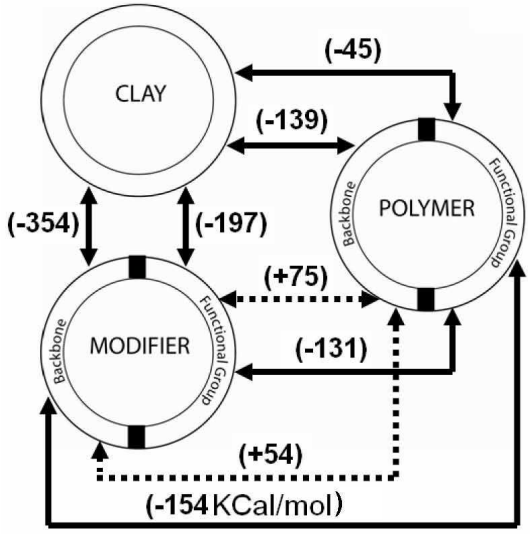

FIG. 8: Energy diagram showing nonbonded interaction energies between polymer, clay, and organic modifier in PCN synthesized with organic modifier, hexadecylamine.

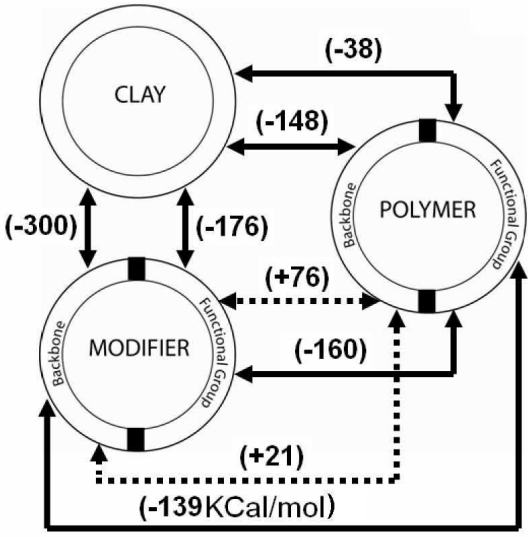

FIG. 9: Energy diagram showing nonbonded interaction energies between polymer, clay, and organic modifier in PCN synthesized with organic modifier, octadecylamine.

interactions with clay, -252 and -348 Kcal/mol, respectively. The interactions between the clay and the polymer are dominant through the backbone of the polymer, which is -128 Kcal/mol; the functional group of polymer has relatively weaker attractive interactions with clay (-34 Kcal/mol). Between the polymer and modifier, the backbone of polymer has repulsive interactions with the backbone as well as functional groups of the organic modifiers, which have magnitudes of $+87$ and $+76$ Kcal/mol, respectively. These interactions are represented by dotted lines in the diagram. The polymer functional groups have significantly strong attractive interactions with the backbone and functional groups of the modifier, which are -173 and -146 Kcal/mol, respectively.

6.5 Interactions in PCN-Octadecyl

The nonbonded interactions between the different constituents (clay, polymer, and organic modifier) of PCN-octadecyl are shown in Fig. 9. The nature of interactions observed in PCN-octadecyl are similar to PCN-dodecyl and PCN-hexadecyl, where the largest attractive nonbonded interactions are observed between the clay and the organic modifier (-476 Kcal/mol), followed by interactions between the polymer and clay (-186 Kcal/mol), and polymer and organic modifiers (-102 Kcal/mol). The interactions of polymer backbone with the backbone and functional groups of organic modifiers are found repulsive only in nature, which has a magnitude of +21 and +76 Kcal/mol, respectively, and these repulsive interactions are represented by a dotted line in the interaction diagrams. Between the polymer and the modifier, the attractive interactions are observed between the polymer functional group with the modifier functional group and backbone, -160 and -139 Kcal/mol, respectively. All attractive interactions between different constituents of PCN are represented by the solid lines in the interaction diagram. Between clay and the modifier, backbones as well as the functional group of the modifier both have significant attractive interactions with clay, -300 and -176 Kcal/mol, respectively. On the other hand, between clay and polymer, significant interactions are found between the polymer backbone and clay (-148 Kcal/mol); relatively weaker interactions (-38 Kcal/mol) are observed between the polymer functional group and clay.

6.6 Interactions in PCN-Dodecyl-Br

The interaction energies between different phases of PCN-dodecyl-Br are shown in Fig. 10. As seen from Table 1(c), the difference between PCN-dodecyl and PCN-dodecyl-Br is the presence of end functional groups in the organic modifiers, which is protonated amine in PCN-dodecyl and trimethyl amine in PCN-dodecyl-Br. The nature of interactions found in PCN-dodecyl-Br is similar to that of PCN-dodecyl, where it is observed that the

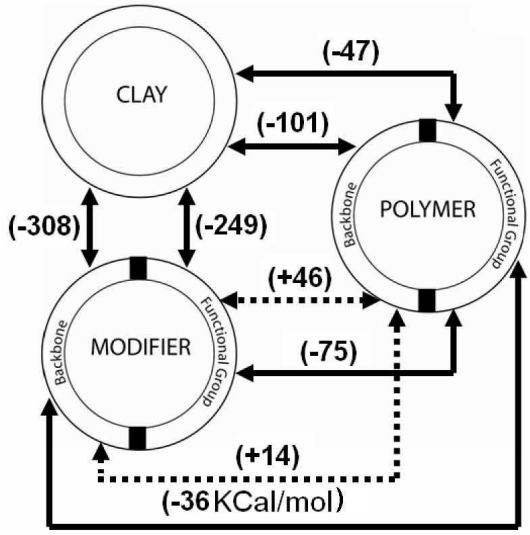

FIG. 10: Energy diagram showing nonbonded interaction energies between polymer, clay, and organic modifier in PCN synthesized with organic modifier, dodecyl trimethyl ammonium bromide.

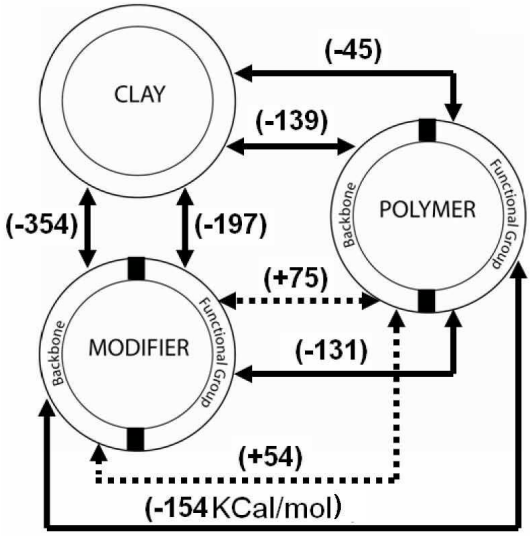

FIG. 11: Energy diagram showing nonbonded interaction energies between polymer, clay, and organic modifier in PCN synthesized with organic modifier, hexadecyl trimethyl ammonium bromide.

highest attractive interactions are between the clay and the modifier (-557 Kcal/mol), followed by interactions between clay and polymer (-148 Kcal/mol) and polymer and modifier (-51 Kcal/mol). Here also we find that clay has attractive interactions with the backbone (-308 Kcal/mol) and functional groups (-249 Kcal/mol) of the modifier, whereas clay has significant interactions with the backbone of polymer (-101 Kcal/mol) and relatively weaker interactions with the polymer functional group (-47 Kcal/mol). Between the polymer and organic modifier, the repulsive as well as attractive, both types of interactions exist which are represented by dashed and solid lines, respectively, in the interaction diagrams. The polymer backbone has repulsive interactions with the modifier backbone and functional group, which are $+14$ and $+46$ Kcal/mol, respectively, in PCN-dodecyl-Br. The polymer functional group has significant stable interactions with the functional group and backbone of modifier which are -75 and -36 Kcal/mol, respectively.

6.7 Interactions in PCN-Hexadecyl-Br

The nonbonded interactions between different constituents (polymer, clay, and organic modifier) of PCN-hexadecyl-Br are shown in Fig. 11. The nature of nonbonded interactions observed between different constituents of PCN-hexadecyl-Br is similar to those of other PCNs. The magnitude of attractive interactions between different constituents of PCN from higher to lower magnitude are in the order of clay–modifier, clay–polymer, and polymer–modifier, and these have the magnitude of -551, -184, and -156 Kcal/mol, respectively. All the interactions are attractive in nature, except the interactions of backbone of polymer with backbone and functional group of polymer. All the attractive and repulsive interactions are represented in solid and dotted lines, respectively, in the interaction diagram. As seen from Fig. 11, the backbone of polymer has repulsive interactions of $+75$ and $+54$ Kcal/mol, with the functional group and backbone of organic modifiers, respectively, in PCN-hexadecyl-Br. The functional group of polymer has attractive interactions with the functional group and backbone of organic modifier, having magnitudes of -131 and -154 Kcal/mol, respectively. Between all the interactions, the highest attractive interactions are observed between the clay and modifier backbone (-354 Kcal/mol) followed by the interactions between clay and the organic modifier functional group (-197 Kcal/mol). Between the clay and polymer, the significantly stronger attractive interactions are observed between the backbone of polymer and clay (-139 Kcal/mol), and relatively weaker interac-

tions are observed between the polymer functional group and clay (-45 Kcal/mol).

6.8 Comparison of Interactions between Polymer and Modifier in PCNs

Polymer is the most abundant constituent of PCNs in which nanoclay inclusions are dispersed in the polymer matrix. Being a major constituent of PCNs, the structure and properties of polymer must have significant impact on the overall structure and properties of nanocomposites. In composite material the interactions between the different constituents play a major role in the structure and properties of composites. Thus, the interphasial interactions of polymer with other constituents (modifier and clay) must have a significant role in the structure and nanomechanical properties of PCN. Furthermore, from Fig. 6 it is evident that in intercalated PCNs, the polymer and organic modifier enter into the interlayer clay spacing of MMT and lie in close association, indicating that interactions between the polymer and organic modifier are important for the structure and nanomechanical properties of PCNs. The interphasial interactions between the backbone and functional groups of polymer and organic modifiers present in PCNs are presented in Table 7(a), where it is observed that the presence of different organic modifiers results in different amounts of interactions between the polymers and organic modifiers in PCNs. Again from Tables 5 and 6 it is observed that the presence of different modifiers in PCNs results in different amounts of crystallinity of polymers in PCNs, indicating that interactions between polymers and organic modifiers have a significant influence on the crystalline structure and nanomechanical properties of PCNs. For studying the effect of backbone chain length of the modifier on interphasial interactions between the polymer and modifier and evaluating its effect on the structure and nanomechanical properties of PCNs, in Table 7(b) we have furnished the interactions between different parts of the modifier and polymer of three PCNs (PCN-dodecyl, PCN-hexadecyl, and

TABLE 7(a): Nonbonded interaction energies between the backbone and functional groups of the polymer and modifier in different PCNs.

Sample	Modi function–poly function (Kcal/mol)	Modi back–poly back (Kcal/mol)	Modi function–poly back (Kcal/mol)
PCN–dodecyl	-98	+21	+47
PCN–dodecyl-Br	-75	+14	+46
PCN–hexadecyl	-146	+87	+76
PCN–hexadecyl-Br	-131	+54	+75
PCN–octadecyl	-160	+21	+76

TABLE 7(b): Effect of chain length of modifier on the interactions between polymer and modifier in PCNs.

Sample	Modi function–poly function (Kcal/mol)	Modi back–poly back (Kcal/mol)	Modi function–poly back (Kcal/mol)
PCN–dodecyl	-98	+21	+47
PCN–hexadecyl	-146	+87	+76
PCN–octadecyl	-160	+21	+76

TABLE 7(c): Effect of functional group of modifier on the interactions between polymer and modifier in PCNs.

Sample	Modi function–poly function (Kcal/mol)	Modi back–poly back (Kcal/mol)	Modi function–poly back (Kcal/mol)
PCN–dodecyl-Br	-75	+14	+46
PCN–dodecyl	-98	+21	+47
PCN–hexadecyl-Br	-131	+54	+75
PCN–hexadecyl	-146	+87	+76

PCN-octadecyl). These PCNs are synthesized with three different organic modifiers (dodecyl, hexadecyl, and octadecyl) having identical end functional groups but different backbone chain lengths, which are 11, 15, and 17 methylene units in dodecyl, hexadecyl, and octadecyl, respectively. From Table 7(b) it is observed that with the increase of the backbone chain length of the modifier, attractive nonbonded interactions between the polymer functional group and the modifier increase. It appears that the polymer functional group anchors on the functional group of the organic modifiers and with the increase of modifier backbone chain length the anchoring strength increases. On the other hand, the polymer backbone has repulsive interactions with the modifier functional group and backbone, and with the increase of the modifier backbone chain length, the repulsive interactions between the polymer backbone and modifier functional group increase. From Table 5 it is observed that with the increase in modifier backbone chain length the PCN crystallinity decreases. Thus, in comparing the results of Tables 5 and 7(b), it appears that combination of attractive and repulsive interactions between polymer and organic modifiers results in the disruption of normal periodic conformations of polymer and subsequently diminishes the crystallinity of polymer in PCNs. As seen from Table 7(b), the higher the backbone chain length of the modifier, the higher are the intensities of attractive and repulsive interactions between selected parts of the polymer and organic modifier, resulting in a higher disruption of the periodic structure of the polymer in PCNs and subsequently, reduction in the crystallinity of the PCN.

In studying the effect of modifier functional groups on the crystallinity and nanomechanical properties of PCNs, the interphasial interactions between different parts of polymer and organic modifiers lying in four typical PCNs (PCN-dodecyl with PCN-dodecyl-Br, and PCN-hexadecyl with PCN-hexadecyl-Br) are compared in Table 7(c). The differences in constituents in these PCNs are due to the presence of organic modifiers, and as seen from Table 1(c), the difference in the molecular structure of the organic modifiers is due to the different end functional group. Between these organic modifiers, dodecyl and hexadecyl have protonated amine, whereas dodecyl-Br and hexadecyl-Br have trimethyl amine as the functional group of one end of the modifier. In comparing the interactions between PCN-dodecyl and PCN-dodecyl-Br from Tables 1(c) and 7(c), it is observed that due to the change of the amine (NH_3)functional group in dodecyl into a trimethyl amine [$N(CH_3)_3$] functional group in dodecyl-Br, the attractive interactions between the polymer functional group with the modifier functional group significantly increase and subsequently, repulsive interactions of polymer backbone with the modifier backbone and functional group also increase considerably. The same trend is observed in PCN-hexadecyl and PCN-hexadecyl-Br, where due to changing the functional group from protonated amine in hexadecyl into the trimethyl amine functional group in hexadecyl-Br, the attractive interactions between the polymer functional group with the modifier functional group as well as the repulsive interactions of polymer backbone with the modifier backbone and functional group significantly increase. As seen from Table 1(a), because the partial charges on the atoms of the amine and trimethyl amine functional groups of the respective modifiers are different, they result in a different amount of interactions in these PCNs. Now from Table 6, it is observed that the crystallinity in PCN-dodecyl and PCN-hexadecyl is lower with respect to that of PCN-dodecyl-Br and PCN-hexadecyl-Br, respectively. Comparing the results of Tables 6 and 7(c), it appears that due to larger attractive interactions between the polymer functional group and the modifier functional group, as well as larger repulsive interactions of polymer backbone with the functional group and backbone of the modifier in PCN-dodecyl and PCN-hexadecyl, there is relatively greater disruption in the normal conformation of polymer and a subsequent reduction in the crystallinity of polymer in comparison to PCN-dodecyl-Br and PCN-hexadecyl-Br, respectively. Thus, by changing only the functional group of the modifier the interactions between the different constituents of PCNs can be changed considerably, which seemingly results in differing amounts of polymer crystallinity in PCNs. This is further evidence that by selecting a suitable modifier functional group, the crystallinity of PCNs can be tailored to a significant extent.

Modulus mapping images of PCN-octadecyl and PCN-hexadecyl-Br are shown in Fig. 12, in which lighter shades represent polymer and darker shades represent the clay plates in PCNs. From the figure it is observed that clay platelets are uniformly dispersed in the polymer matrix. The localized interactions between the nanoclay particles and polymer also result in the disruption of crystallinity of polymer in PCNs.

The mechanical properties of composite materials largely depend on their interphasial interactions. Negative interactions indicate attractive or stable interactions between the constituents of composite. As seen from Table 7(b), the highest attractive interactions between polymer and modifier functional groups are observed in PCN-octadecyl, followed by PCN-hexadecyl and PCN-

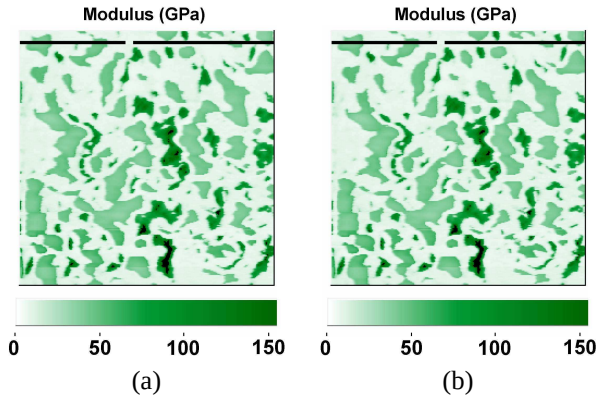

FIG. 12: Modulus mapping image of **(a)** PCN-octadecyl and **(b)** PCN-hexadecyl-Br showing dispersion of submicron-size clay particles in the polymer matrix in polymer clay nanocomposites. Dark shades show clay particles and lighter shades show polymer matrix.

dodecyl. On the other hand, from Table 5, the highest elastic modulus of PCN is observed in PCN-octadecyl followed by PCN-hexadecyl and PCN-dodecyl. Thus, comparing the results of Tables 5 and Table 7(b), it seems that with an increase in modifier backbone chain length, the attractive interactions between the polymer functional group and the modifier functional group increase, which results in stronger docking between the polymer functional group and the modifier functional group, and subsequently results in the higher elastic modulus of PCN. From the above discussion it is further observed that by changing the backbone chain length or functional group of the modifier, the elastic modulus of a particular polymer-based PCN can be changed, which is a result of change in attractive interactions between the the functional group of the polymer and the functional group of the modifier present in PCNs.

Comparing results in Tables 6 and 7(c), it is observed that due to the presence of a protonated amine group instead of a trimethyl amine group in the modifier, the relatively larger attractive interactions between the functional group of polymer and the functional group of the modifier are observed in PCN-dodecyl and PCN-hexadecyl in comparison to those in PCN-dodecyl-Br and PCN-hexadecyl-Br, respectively. These larger attractive interactions result in greater docking strength between the polymer functional group and the modifier functional group, causing a change in the elastic modulus in PCN-dodecyl and PCN-hexadecyl in comparison to that of PCN-dodecyl-Br and PCN-hexadecyl-Br, respectively. However, it appears that the effect of modifier functional groups on the PCN elastic modulus is not as prominent as the change in backbone chain length of modifiers.

6.9 Comparison of Interactions between Clay and Polymer in PCNs

The interactions between different parts (backbone and functional group) of polymer and clay in PCNs are shown in Table 8(a). To evaluate the effect of backbone chain length of the polymer on the crystallinity and nanomechanical properties of PCNs, in Table 8(b) the polymer–clay interaction energies between PCN-dodecyl, PCN-hexadecyl, and PCN-octadecyl are compared. As seen from Table 8(b) it is evident that both the backbone and functional group of polymer have dominantly van der Waals interaction with clay. The differences in interaction energies between the clay and polymer in PCNs are primarily due to the difference in van der Waals interaction. The van der Waals interaction energy solely depends on the distance between interacting atoms. The presence of different organic modifiers in PCNs results in different amounts of interactions between the constituents (clay, polymer, and organic modifier) of PCNs, which seems to result in different distances between clay and polymer. Thus, the difference in interaction energies between polymer and clay in PCNs is due to the presence of different organic modifiers.

In order to evaluate the effect of the modifier functional group on the interactions between the polymer and the clay in PCNs and evaluating the influence of polymer–clay interactions on the structure and nanomechanical properties of PCNs, the interaction energies between polymer and clay in PCN-dodecyl and PCN-dodecyl-Br, and PCN-hexadecyl and PCN-hexadecyl-Br are compared in Table 8(c). From Table 8(c) we observe that differences in interaction energies between different parts (backbone and functional group) of the polymer and clay in corresponding PCNs are due to the difference in van der Waals energies, which essentially occurs due to the presence of different organic modifiers in the PCNs. Thus, the differences in structure and nanomechanical properties observed in different PCNs are the result of interactions between the backbone chain and functional groups of polymer and organic modifiers present in PCNs.

6.10 Comparison of Interactions between Clay and Organic Modifiers in PCNs

The interaction energies between clay and different parts of organic modifiers in PCNs are shown in Table 9. As

TABLE 8(a): Nonbonded interaction energies between different parts of polymer and clay in PCNs.

Sample	Clay–poly back (Kcal/mol)			Clay–poly function (Kcal/mol)			Clay–poly (Kcal/mol)		
	VDW	Elec	Total non-bond	VDW	Elec	Total non-bond	VDW	Elec	Total non-bond
PCN–dodecyl	-125	+2	-123	-70	0	-70	-195	+2	-193
PCN–dodecyl-Br	-97	-4	-101	-40	-7	-47	-137	-11	-148
PCN–hexadecyl	-112	-16	-128	-52	+18	-34	-164	+2	-162
PCN–hexadecyl-Br	-121	-18	-139	-55	+10	-45	-176	-8	-184
PCN–octadecyl	-127	-21	-148	-57	+19	-38	-184	-2	-186

TABLE 8(b): Effect of modifier backbone chain length on the interactions between clay and polymer in PCNs.

Sample	Clay–poly back (Kcal/mol)			Clay–poly function (Kcal/mol)			Clay–poly (Kcal/mol)		
	VDW	Elec	Total non-bond	VDW	Elec	Total non-bond	VDW	Elec	Total non-bond
PCN–dodecyl	-125	+2	-123	-70	0	-70	-195	+2	-193
PCN–hexadecyl	-112	-16	-128	-52	+18	-34	-164	+2	-162
PCN–octadecyl	-127	-21	-148	-57	+19	-38	-184	-2	-186

TABLE 8(c): Effect of modifier functional group on the interactions between clay and polymer in PCNs.

Sample	Clay-poly back (Kcal/mol)			Clay–poly function (Kcal/mol)			Clay–poly (Kcal/mol)		
	VDW	Elec	Total non-bond	VDW	Elec	Total non-bond	VDW	Elec	Total non-bond
PCN–dodecyl-Br	-97	-4	-101	-40	-7	-47	-137	-11	-148
PCN–dodecyl	-125	+2	-123	-70	0	-70	-195	+2	-193

TABLE 9: Nonbonded interaction energies between clay and organic modifier in different PCNs.

Sample	Clay–modi back (Kcal/mol)			Clay–modi function (Kcal/mol)			Clay–modi (Kcal/mol)		
	VDW	Elec	Total non-bond	VDW	Elec	Total non-bond	VDW	Elec	Total non-bond
PCN–dodecyl	-270	-54	-324	-58	-214	-272	-328	-268	-596
PCN–dodecyl-Br	-259	-49	-308	-122	-127	-249	-381	-176	-557
PCN–hexadecyl	-251	-97	-348	-35	-217	-252	-286	-314	-600
PCN–hexadecyl-Br	-255	-99	-354	-85	-112	-197	-340	-211	-551
PCN–octadecyl	-238	-62	-300	-33	-143	-176	-271	-205	-476

seen from Table 9, between the modifier backbone and the clay, the interaction is dominantly van der Waals in nature, whereas between the modifier functional group and clay, the interaction is dominantly electrostatic in nature. From Table 9 and interaction energy diagrams in Figs. 7–11, it is observed that attractive interactions between the modifier and clay are much stronger than the interaction between the clay and polymer or polymer and modifier in PCNs. The failure of composite materials occurs through the weakest interface of their constituents. The interface between clay and modifier is the strongest among the three interfaces in PCNs. Hence the interactions between the polymer and modifier have the most influence on nanomechanical properties of PCNs.

6.11 Summary of Results of PCNs Containing Organic Modifiers with Identical Functional Groups and Different Backbone Chain Lengths

The interaction energies, percentage of crystallinity, and nanomechanical properties of PCNs containing organic modifiers with dissimilar backbone chain lengths are summarized in Table 10(a), where we see that an increase in the backbone chain length of the modifier results in higher attractive interactions between the modifier and polymer functional groups,,as well as higher repulsive interactions between the polymer backbone and the modifier functional group. The combination of attractive and repulsive interactions between the polymer and organic modifier results in a reduction in crystallinity of the PCN, whereas the attractive interactions between the functional group of the polymer and the modifier results in an increase in the elastic modulus of PCNs. From the representative molecular model of PCNs we see that the sizes of the polymer chain intercalated inside the clay gallery in PCN-dodecyl, PCN-hexadecyl, and PCN-octadecyl are 8, 12, and 18 monomer units of polymer (PA6), respectively. Thus, PCN-hexadecyl and PCN-octadecyl have respectively 1.5 and 2.25 times the intercalated polymer inside the clay gallery than that of PCN-dodecyl. The larger the amount of polymer inside the clay gallery, the larger the direct interaction of polymer with the modifier and subsequently, the larger the disruption of polymer crystallinity in the PCN, which is also evidenced from Table 10(b). In Table 10(b) we provide the relative amount of interaction energies between the polymer and modifier in PCN-hexadecyl and PCN-octadecyl with respect to the amount of intercalated polymer in PCN-dodecyl. In column 8 of Table 10(b) the differences in repulsive and attractive interactions between the polymer and modifier in different PCNs is computed. As seen previously, repulsive as well as attractive interactions between polymer and modifier both contribute to disruption of polymer crystallinity in PCNs. Thus, the difference in repulsive and attractive interaction energies between the polymer and modifier is largest in PCN-octadecyl, and the lowest crystallinity is observed in PCN-octadecyl, followed by PCN-hexadecyl and PCN-dodecyl.

The differences in the relative amount of repulsive and attractive interaction energies, percentage of crystallinity, and the elastic modulus of different PCNs containing modifiers with varying backbone chain lengths are plotted in Fig. 13. From Fig. 13 it is evident that with the increase in backbone chain length of the modifier, the difference in the relative interaction energies in PCNs increases, which results in a reduction of polymer crystallinity in PCNs in the order of PCN-octadecyl, PCN-hexadecyl, and PCN-dodecyl. Furthermore, attractive interaction energies between polymer and modifier functional groups increases with increasing backbone chain length of the modifier, which results in a gradual increase in the elastic modulus of PCNs in the sequence PCN-dodecyl, PCN-hexadecyl, and PCN-octadecyl. Thus, it is observed that with increasing backbone chain length of the modifier, the crystallinity (structure) and nanomechanical properties of par-

TABLE 10(a): Summary of interactions between polymer and modifier and their relation with crystallinity and elastic modulus of PCN containing modifiers with increasing backbone chain length.

PCN Samples	Structural difference		Modi func–poly func (Kcal/mol)	Modi back–poly back (Kcal/mol)	Modi func-poly back (Kcal/mol)	% Crystallinity from DSC	E (GPa)
	Backbone	Functional group					
PCN-dodecyl	$(CH_2)_{11}$	NIL	-98	+21	+47	27.78	4.77
PCN-hexadecyl	$(CH_2)_{15}$	NIL	-146	+87	+76	20.81	4.81
PCN-octadecyl	$(CH_2)_{17}$	NIL	-160	+21	+76	19.81	5.06

TABLE 10(b): Summary of relative interaction energies between polymer and modifier equivalent to amount of intercalated polymer in PCN, and its relation with crystallinity and elastic modulus of PCNs containing modifiers with increasing backbone chain length.

PCN samples (col.1)	Structural difference			Relative estimation of interaction energies equivalent to amount of intercalated polymer in PCN				%	E (GPa)
	Organic modifier		No. of	Modi	Modi	Modi	Difference	Crystal-	Between
	Backbone (col. 2)	Functional group (Col.3)	monomers in intercalated polymer lying in PCN (col. 4)	func-poly func-tion (Col.5)	back-poly back (Col.6)	function-poly back (Col.7)	in energies between posi-tive and negative part (Col.8)= (Col.7) +(Col.6) -(Col.5)	linity from DSC (col. 9)	polymer and modifier (col. 10)
PCN-dodecyl	$(CH_2)_{11}$	NIL	8	-98	+21	+47	166	27.78	4.77
PCN-hexadecyl	$(CH_2)_{15}$	NIL	12	-219	+131	+114	464	20.81	4.81
PCN-octadecyl	$(CH_2)_{17}$	NIL	18	-360	+47	+171	578	19.81	5.06

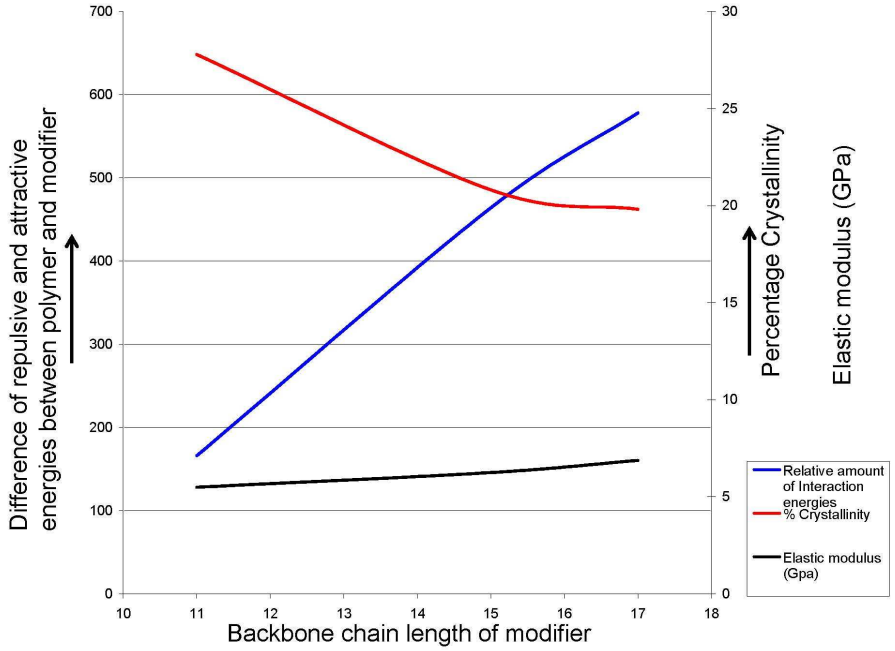

FIG. 13: Plot shows the relation between modifier backbone chain length with the differences in attractive and repulsive interaction energies, crystallinity, and elastic modulus of different PCNs.

TABLE 11: Summary of interactions between polymer and modifier and their relation with crystallinity and elastic modulus of PCN containing modifiers with different functional groups.

PCN samples	Structural difference		Modi func-poly func	Modi back-poly back	Modi func-poly back	% Crystallinity from DSC	E (GPa)
	Backbone	Functional group					
PCN-dodecyl-Br	NIL	$N(CH_3)_3$	-75	+14	+46	27.95	4.36
PCN-dodecyl	NIL	(NH_3)	-98	+21	+47	27.78	4.77
PCN-hexadecyl-Br	NIL	$N(CH_3)_3$	-131	+54	+75	28.05	4.84
PCN-hexadecyl	NIL	(NH_3)	-146	+87	+76	20.81	4.81

ticular polymer-based PCNs can be tailored to a significant extent by controlling the interaction between the intercalated polymer and the modifier in PCNs.

6.12 Summary of Results of PCNs Containing Organic Modifiers with Identical Backbone Chain and End Functional Groups

The interaction energies, percentage of crystallinity, and nanomechanical properties of PCNs containing organic modifiers with different end functional groups are summarized in Table 11. Here it is observed that by selecting an appropriate functional group in the modifier (in this case protonated amine in place of trimethyl amine), the attractive interactions between the polymer functional group and the modifier functional group, and repulsive interactions between the polymer backbone and the modifier functional group can be changed significantly, which in effect changes the crystallinity and elastic modulus of PCNs. However, the effect of the modifier functional group on the crystallinity and elastic modulus of PCNs is not as conclusive as the effect of backbone chain length of organic modifiers.

7. CONCLUSIONS

The backbone chain length of organic modifiers has significant influence on the crystallinity and elastic modulus of PCNs in the nanometer length scale. By increasing the backbone chain length of the modifier, the attractive interactions between the modifier functional group and the polymer functional group as well as repulsive interactions between the polymer backbone and modifier functional group can be significantly increased. The combination of attractive and repulsive interactions between the polymer and modifier determines the crystallinity of polymer in PCNs. The elastic modulus of PCNs depends on attractive interactions between the functional groups of the polymer and modifier. Thus, through the selection of an appropriate modifier backbone chain length during synthesis of PCNs, interfacial interactions between the intercalated polymer and the organic modifier in PCNs can be controlled, which in turn helps in tailoring the percentage crystallinity and nanomechanical properties (elastic modulus in nanometer length scale) of particular polymer-based PCNs to a considerable extent.

The modifier functional group also has an influence on the percentage of crystallinity and elastic modulus of PCNs in the nanometer length scale. By incorporating an appropriate functional group in the modifier, the interphasial interactions between the intercalated polymer and the organic modifier can be controlled to a great extent, which in turn can alter the percentage crystallinity and the elastic modulus of particular polymer-based PCNs.

ACKNOWLEDGEMENTS

The authors would like to acknowledge use of the computational resources at the Center for High Performance Computing (CHPC), NDSU, and the Biomedical Research Infrastructure Network (BRIN). We thank Dr. Gregory H. Wettstein for his assistance in providing hardware and software facilities. Author D.S. acknowledges the support of an NDSU doctoral fellowship award.

REFERENCES

Besler, B. H., Merz, K. M., and Kollman, P. A., Atomic charges derived from semiempirical methods, *J. Comput. Chem.*, vol. **11**, pp. 431–439, 1990.

Brooks, B. R., Bruccoleri, R. E., Olafson, B. D., States, D. J., Swaminathan, S., and Karplus, M., CHARMM: A program for macromolecular energy, minimization, and dynamics calculations, *J. Comp. Chem.*, vol. **4**, pp. 187–217, 1983.

Dionne, P. J., Ozisik, R., and Picu, C. R., Structure and dynamics of polyethelene nanocomposites, *Macromolecules*, vol. **38**, pp. 9351–9358, 2005.

Dionne, P. J., Picu, C. R., and Ozisik, R., Adsorption and desorption dynamics of linear polymer chains to spherical nanoparticles: A Monte Carlo investigation, *Macromolecules*, vol. **39**, pp. 3089–3092, 2006.

Feller, S. E., Zhang, Y., Pastor, R. W., and Brooks, B. R., Constant pressure molecular dynamics simulation: The Langevin piston method, *J. Comput. Phys.*, vol. **103**, pp. 4613–4621, 1995.

Frisch, M. J., Trucks, G. W., Schlegel, H. B., Scuseria, G. E., Robb, M. A., Cheeseman, J. R., Zakrzerwski, V. G., Montgomery, J. A., Jr., Stratmann, R. E., Burant, J. C., Dapprich, S., Millam, J. M., Daniels, A. D., Kudin, K. N., Strain, M. C., Farkas, J., Tomasi, J., Barone, V., Cossi, M., Cammi, R., Mennucci, B., Pomelli, C., Adamo, C., Clifford, S., Ochterski, J., Petersson, G. A., Ayala, P. Y., Cui, Q., Morokuma, K., Malick, D. K., Rabuck, A. D., Raghavachari, K., Foresman, J. B., Cioslowski, J., Ortiz, J. V., Baboul, A. G., Stefanov, B. B., Liu, G., Liashenko, A., Piskorz, P., Komaromi, I., Gomperts, R., Martin, R. L., Fox, D. J., Keith, T., Al-Laham, M. A., Peng, C. Y., Nanayakkara, A., Gonzalez, C., Challacombe, M., Gill, P. M. W., Johnson, B., Chen, W., Wong, M. W., Andres, J. L., Gonzalez, C., Head-Gordon, M., Replogle, E. S., and Pople, J. A., *Gaussian 98*, rev. A.7, Pittsburgh, PA: Gaussian, Inc, 1995.

Gaudel-Siri, A., Brocorens, P., Siri, D., Gardebien, F., Bredas, J. L., and Lazzaroni, R., Molecular dynamics study of ϵ-caprolactone intercalated in wyoming sodium montmorillonite, *Langmuir*, vol. **19**, pp. 8287–8291, 2003.

Ginzburg, V. V., Singh, C., and Balazs, A. C., Theoretical phase diagrams of polymer/clay composites: The role of grafted organic modifiers, *Macromolecules*, vol. **33**, pp. 1089–1099, 2000.

Hsueh, H. B. and Chen, C. Y., Preparation and properties of LDHs/epoxy nanocomposites, *Polymer*, vol. **44**, pp. 5275–5283, 2003.

Humphrey, W., Dalke, A., and Schulten, K., VMD—Visual molecular dynamics, *J. Molec. Graphics*, vol. **14**, pp. 33–38, http://www.ks.uiuc.edu/Research/vmd/, 1996.

Kalé, L., Skeel, R., Bhandarkar, M., Brunner, R., Gursoy, A., Krawetz, N., Phillips, J., Shinozaki, A., Varadarajan, K., and Schulten, K., NAMD2: Greater scalability for parallel molecular dynamics, *J. Comput. Phys.*, vol. **151**, pp. 283–312, http://www.ks.uiuc.edu/Research/namd/, 1999.

Karasawa, N. and Goddard, W. A., Acceleration of convergence for lattice sums, *J. Phys. Chem.*, vol. **93**, pp. 7320–7327, 1989.

Katti, D., Schmidt, S., Ghosh, P., and Katti, K., Modeling the response of pyrophyllite interlayer to applied stress using steered molecular dynamics, *Clays Clay Minerals*, vol. **53**, pp. 171–178, 2005.

Katti, K. S., Sikdar, D., Katti, D. R., Ghosh, P., and Verma, D., Molecular interactions in intercalated organically modified clay and clay-polycaprolactam nanocomposites: Experiments and modeling, *Polymer*, vol. **47**, pp. 403–414, 2006.

Ma, C. C. M., Kuo, C. T., Kuan, H. C., and Chiang, C. L., Effects of swelling agents on the crystallization behavior and mechanical properties of polyamide 6/clay nanocomposites, *J. Appl. Polym. Sci*., vol. **88**, pp. 1686–1693, 2003.

Martyna, G. J., Tobias, D. J., and Klein, M. L., Constant pressure molecular dynamics algorithms, *J. Chem. Phys.*, vol. **101**, pp. 4177–4189, 1994.

Meneghetti, P. and Qutubuddin, S., Synthesis, thermal properties and applications of polymer-clay nanocomposites, *Thermochim. Acta*, vol. **442**, pp. 74–77, 2006.

Mitsunaga, M., Ito, Y., Ray, S. S., Okamoto, M., and Hironaka, K., Intercalated polycarbonate/clay nanocomposites: Nanostructure control and foam processing, *Macromol. Mater. Eng*., vol. **288**, pp. 543–548, 2003.

Okada, A., Kawasumi, M., Usuki, A., Kojima, Y., Kurauchi, T., and Kamigaito, O., Nylon 6-clay hybrid, *Mater. Res. Soc. Symp. Proc.*, vol. **171**, pp. 45–50, 1990.

Qin, H., Zhang, S., Zhao, C., and Yang, M., Zero-order kinetics of the thermal degradation of polypropylene/clay nanocomposites, *J. Polym. Sci., Part B: Polymer Phys.*, vol. **43**, pp. 3713–3719, 2005.

Ray, S. S. and Okamoto, M., Polymer/layered silicate nanocomposites: A review from preparation to processing, *Prog. Polym. Sci*., vol. **28**, pp. 1539–1541, 2003.

Sikdar, D., Katti, D. R., and Katti, K. S., A molecular model for ε-caprolactam based intercalated polymer clay nanocomposites: Integrating modeling and experiments, *Langmuir*, vol. **22**, pp. 7738–7747, 2006a.

Sikdar, D., Katti, D. R., Katti, K. S., and Bhowmik, R., Insight into molecular interactions between constituents in polymer clay nanocomposites, *Polymer*, vol. **47**, pp. 5196–5205, 2006b.

Sikdar, D., Katti, D., Katti, K., and Mohanty, B., Effect of organic modifiers on dynamic and static nanomechanical properties and crystallinity of intercalated clay-polycaprolactam nanocomposites, *J. Appl. Polym. Sci.*, vol. **105**, pp. 790–802, 2007.

Sikdar, D., Katti, D., and Katti, K., The role of interfacial interactions on the crystallinity and mechanical properties of clay polymer nanocomposites: A molecular dynamics study, *J. Appl. Polym. Sci.*, vol. **107**, pp. 3137–3148, 2008a.

Sikdar, D., Pradhan, S. M., Katti, D. R., Katti, K. S., and Mohanty, B., Altered phase model of polymer clay nanocomposites, *Langmuir*, vol. **24**, pp. 5599–5607, 2008b.

Sikdar, D., Katti, K. S., and Katti, D. R., Molecular interactions

alter clay and polymer structure in polymer clay nanocomposites, *J. Nanosci. Nanotechnol.*, vol. **8**, pp. 1–20, 2008c.

Sikdar, D., Katti, D., Katti, K., and Mohanty, B., Influence of backbone chain length and functional groups of organic modifiers on crystallinity and nanomechanical properties of intercalated clay-polycaprolactam nanocomposites, *Int. J. Nanosci. Nanotechnol.*, vol. **6**, pp. 568–592, 2009.

Singh, U. C. and Kollman, P. A., An approach to computing electrostatic charges for molecules, *J. Comput. Chem.*, vol. **5**, pp. 129–145, 1984.

Skipper, N. T., Sposito, G., and Chang, F. R., Monte Carlo simulation of interlayer molecular structure in swelling clay minerals, 1. Methodology, *Clays Clay Minerals*, vol. **43**, pp. 285–293, 1995a.

Skipper, N. T., Sposito, G., and Chang, F. R., Monte Carlo simulation of interlayer molecular structure in swelling clay minerals, 1. Monolayer hydrates, *Clays Clay Minerals*, vol. **43**, pp. 294–303, 1995b.

Teppen, B. J., Rasmussen, K., Bertsch, P. M., Miller, D. M., and Schafer, L., Molecular dynamics modeling of clay minerals, 1. Gibbsite, kaolinite, pyrophyllite, and beidellite, *J. Phys. Chem. B.*, vol. **101**, pp. 1579–1587, 1997.

Vaia, R. A. and Giannelis, E. P., Polymer melt intercalation in organically-modified layered silicates: Model predictions and experiment, *Macromolecules*, vol. **30**, pp. 8000–8009, 1997.

Vaia, R. A., Pinnavaia, T. J., and Beall, G. W., *Polymer-Clay Nanocomposites*, New York: John Wiley & Sons, Ltd., pp. 229–235, 2002.

Zhang, J. and Wilkie, C. A., Preparation and flammability properties of polyethylene-clay nanocomposites, *Polym. Degradation Stability*, vol. **80**, pp. 163–169, 2003.

Journal for Multiscale Computational Engineering 8(6), 585–595 (2010)

CONCRETE AS A HIERARCHICAL STRUCTURAL COMPOSITE MATERIAL

Weidong Wu,[1,*] Ahmed Al-Ostaz,[2] Alexander H.-D. Cheng,[3] & Chung R. Song[4]

[1]*Research Associate, Department of Civil Engineering, University of Mississippi, University, MS 38677, USA*

[2]*Associate Professor, Department of Civil Engineering, University of Mississippi, University, MS 38677, USA*

[3]*Professor, Department of Civil Engineering, University of Mississippi, University, MS 38677, USA*

[4]*Associate Professor, Department of Civil Engineering, University of Mississippi, University, MS 38677, USA*

[*]Address all correspondence to Weidong Wu E-mail: wwu3@olemiss.edu

A multiscale modeling methodology that relates the nanostructure of concrete to its micro and macro properties is presented. This work attempts to establish a framework for understanding the relations among chemical composition, microstructure morphology, and the macroscale mechanical properties of concrete constituents. The simulation is based on four levels of a hierarchal structural model, starting from the molecular dynamics simulation of hydrated cement solid nanoparticles (e.g., C–S–H, and calcium hydroxide), all the way up to concrete. To validate the theoretical model, a nondestructive testing technique, resonant ultrasound spectroscopy (RUS), is used to measure the elastic constants of hydrated cement paste. The results showed good agreement between theoretically predicted and experimentally measured properties.

KEY WORDS: *multiscale, concrete simulation, mechanical properties, C–S–H, molecular dynamics, microporomechanics*

1. INTRODUCTION

Cement concrete is one of the world's most widely used materials. Unfortunately, the production of cement involves a thermal process that accounts for 5–10 percent of the world's total CO_2 emissions. Constantinides and Ulm (2007) studied the cement paste and found that the macroscopic strength of concrete appears to be linked to the nano-granular structure of its constituents, particularly the calcium–silicate–hydrate (C–S–H) units and not to its chemistry. They argued that if one can replace the constituents of conventional Portland cement with materials of the same or similar nanostructure, which can be produced without an intensive thermal process, then it opens the door for a "green concrete" that can cut global CO_2 emission. Therefore, a basic understanding of the nano/micro structure of concrete constituents and how this relates to the macroscopic mechanical properties is essential to the design of a new class of concrete that is high strength, yet green. Macroscopic properties of concrete essentially depend on the nanostructure of concrete's major constituent, that is, C–S–H, and how C–S–H nanoparticles are organized (stacked). Studying macroscopic properties of concrete based on nanoscale constituent properties and the sub-micro and micro structure of major strength contribution may show how nanoscale constituents link to the macroscale materials. Another way to "green-up" is to study how to improve the nanos-

1543–1649/10/$35.00

tructure of the constituents, especially for C–S–H, to enhance the macro properties of concrete.

Many materials, including advanced nanocomposites as well as concrete, may be studied as multiscale materials. This has been the focus of many researchers. For example, Fish et al. (2000, 2002, 2010), Yuan and Fish (2009), and Li et al. (2008) employed multiscale modeling techniques to study advanced materials, and Jasiuk (2005) characterized and modeled trabecular bone as a five-structural-level hierarchical random composite material. Gates et al. (2005) outlined multiscale modeling methods used in simulating nanostructured materials.

Concrete may be considered as a composite material at a range of levels (scales). The lowest level is the C–S–H solids. Several microstructural models of the C–S–H gels have been proposed (Aligizaki, 2005). The milestone work for the C–S–H gel structure is credited to Powers and Brownyard (1948, 1960), where they proposed cement paste as a colloid composed of spheres where each sphere represents gel substance with its associated gel pores; in between the spheres are capillary pores outside the C–S–H gel. The C–S–H gel is composed of particles. The particles have a layered structure which is made up of two to three layers. Taylor's C–S–H gel model (Taylor, 1986, 1993) claimed that C–S–H has a disordered layer structure, mainly composed of structurally imperfect jennite and 1.4 nm tobermorite. Feldman and Sereda (1970) proposed a model similar to the Powers–Brownyard model. The difference lies in that C–S–H sheets in the Feldman–Sereda model do not have an ordered layered structure; they are an irregular array of single layers. Both the Powers–Brownyard and Feldman–Sereda models essentially describe a layered structure for the C–S–H gel. However, the C–S–H gel in models proposed by Wittmann (1979) and Jennings and Tennis (2000, 2004, 1994) has a colloid structure. The Wittmann C–S–H model has a three-dimensional network of amorphous colloid gel particles forming a xerogel, and the C–S–H gel particles are separated by strongly absorbed thin films of water. Jennings' recent C–S–H model (Tennis and Jennings, 2000; Jennings, 2000, 2004) proposed a new concept, "globules", which is the basic building block with structural water. C–S–H solid with different gel porosity forms two types of C–S–H: low-density (LD) and high-density (HD) C–S–H. In this paper we distinguish the "globules" and LD/HD C–S–H by two levels: a globules scale, i.e., nanoscale in this research, and an LD/HD C–S–H gel scale, i.e., sub-microscale in this work. LD/HD C–S–H particles, unreacted cement clinkers, large hexagonal crystalline calcium hydroxide (CH), and capillary cavities and voids, form an even higher level: microscale cement paste. For a microstructural model of a well-hydrated Portland cement paste see Mehta (1986). Modeling of concrete mechanical properties is given afterward.

There have been only a few successful attempts to model the macroscopic mechanical properties of cement paste and concrete from their microstructure, as reported in the literature. The challenges in simulation stem from the complex nanoporous structures, limited knowledge of the individual constituent properties, and the large variation in curing conditions. Among the few available research reports on concrete simulation, Bentz et al. (1995) developed a multiscale cement-based material model which consists of individual digital-image-based structural models for C–S–H at the nanometer level, cement paste at the micrometer level, and a mortar or concrete at millimeter level. Bernard et al. (2003) employed a multiscale micromechanics hydration model, combined with intrinsic material properties, to predict the early age elastic properties of cement-based materials. In another study, Ulm et al. (2004) treated concrete as a multiscale poroelastic material. Feng and Christian (2007) proposed a three-phase micromechanics model of cement paste using theories of composite and poromechanics to predict the properties of hardened cement pastes. They adopted existing literature values of solid phases, C–S–H, CH (calcium hydroxide), and cement. However, LD and HD C–S–H were not distinguished and cement paste was treated only as a three-phase composite (C–S–H, CH, and unreacted cement). Haecker et al. (2005) predicted elastic modulus as a function of degree of hydration using a finite-element-based "microstructure development model".

Research from this current study developed a multiscale modeling methodology to relate the nanostructural properties to the micro and macro performance of concrete. This study is built on a four-level microstructural model. At the molecular and nano scale, fundamental mechanical properties of constitutive mineral crystals of cement, hydrated cement paste (C–S–H globules), sand, and aggregate are calculated by molecular dynamics (MD) simulation. These nanoscale properties are used as the input for the computation of sub-microscale LD and HD C–S–H mechanical properties. At microscale, the effective properties of cement paste and mortar are predicted with the help of micromechanics of composite theory and the microstructural model of hydrated cement paste (HCP) developed by the authors as shown in Section 3. A void effect is introduced by an empirical porosity–elastic prop-

erty relation. To validate the model, resonant ultrasound spectroscopy (RUS) is used to measure the elastic properties, which are then compared to the simulation result for HCP. Finally, at macro (continuum) scale, both the lattice model and the generalized method of cells (GMC) are employed to compute the effective properties of concrete. The multiscale input and output for each scale are illustrated in Fig. 1.

2. MULTISCALE APPROACH FOR CEMENT CONCRETE

Figure 1 illustrates a four-level model to obtain macroscale properties for cement-based materials (Dormieux and Ulm, 2005). Level 1 represents the nanoscale C–S–H solid phase which includes globules and nanopores. Level 2 includes LD and HD C–S–H and the gel pores, which have a dimension of roughly larger than 16.6 nm diameter. Level is cement paste which is composed of C–S–H matrix, residual cement clinkers, CH, and macropores. Monosulfate hydrate (AFm phase) has a minor effect on the structural properties of cement paste, and for simplicity it was replaced with CH in this study. Level 4 is a composite which can be mortar or concrete.

Level 1 C–S–H plays a central role in the study of cement-based material properties. A widely accepted C–S–H colloidal model is by Jennings and co-worker (Tennis and Jennings, 2000; Jennings, 2000; 2004), in which

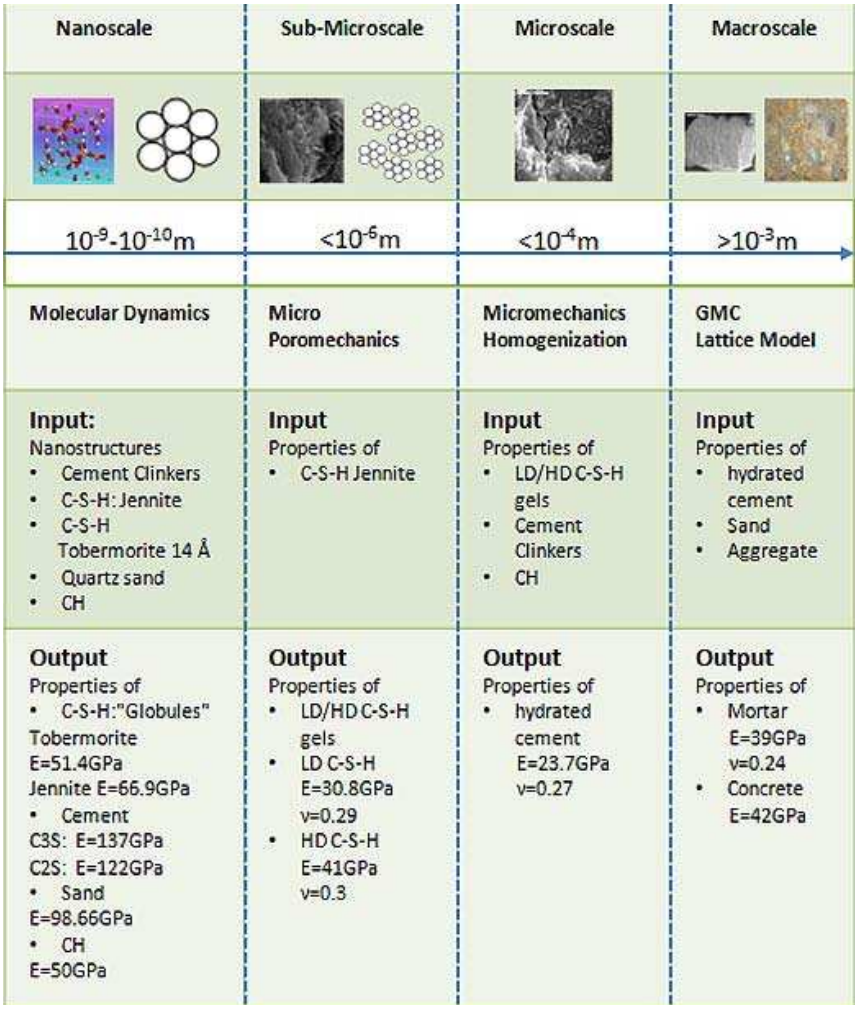

FIG. 1: Diagram of the multiscales, input and output.

they assumed that two types of C–S–H, LD and HD, exist in cement gel. LD and HD C–S–H have 37% and 24% gel porosity, respectively. Both LD and HD C–S–H are formed by the basic building blocks called globules, having a dimension of 5.6 nm and nanoporosity of 18%, which is usually filled with structural water.

Gel porosities of C–S–H and nanoporosity of globules are intrinsic properties of concrete. The volumetric proportion of LD C–S–H and HD C–S–H changes from one cement paste to another, depending on the water-to-cement ratio and curing condition. In the development of the microstructure of cement, HD C–S–H usually forms around residual cement clinkers while CH is generally formed in between LD C–S–H and is adjacent to macropores (Dormieux and Ulm, 2005).

There are two types of multiscale modeling techniques: hierarchical and concurrent. Hierarchical modeling starts the computation from lower level materials, such as the crystalline structure of C–S–H, and these computed lower level properties are used as input data for the next level computation, and so on. In the concurrent modeling, various methods, such as finite element (FE), molecular dynamics (MD), etc., are applied to regions of different scales of the material at the same time. Research for this paper employs the hierarchical modeling method to simulate cement-based materials (concrete and mortar) as shown in Fig. 2.

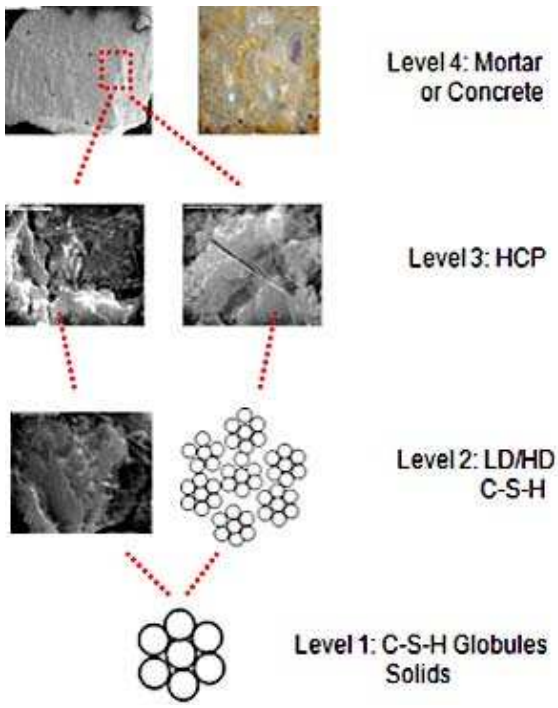

FIG. 2: Multilevel microstructure images of cement-based materials.

3. HYDRATED CEMENT PASTE AND MORTAR MODEL

The micromechanics model for cement paste and mortar discussed in this paper is based on the following two observations (Dormieux and Ulm, 2005): (1) unreacted cement is generally rimmed by HD C–S–H; and (2) CH tends to grow in between LD C–S–H sheets. The scheme for this proposed hydrated cement model is illustrated in Fig. 3. In this model, LD C–S–H and CH are assumed to form a LD/CH composite, which can then be the inclusion of the next level of hydrated cement composite (composite 2). Unreacted cement is enclosed by HD C–S–H to form a HD/cement composite (composite 1–1), which can be the matrix of composite 2. Mortar (composite 3) is considered to be composed of sand particles and composite 2.

For the multiscale computation, MD is utilized to simulate the mechanical properties of nanoscale solid phase C–S–H (C–S–H structural related mineral crystals tobermorite 14 Å and jennite), calcium hydroxide (CH), and sand (alpha quartz). Then the properties of LD and HD C–S–H gels are calculated using microporomechanics theories (Wu et al., 2008). Next, the effective properties of two-level composites—composite 1 (1–1, and 1–2) and composite 2—are calculated using the Mori-Tanaka method (M-T). Finally M-T theory was applied to obtain the homogenized properties of mortar (composite 3). In order to account for the presence of voids in the mortar (mortar porosity), empirical elastic properties–porosity relations are used to calculate the effective properties of mortar. However, the volumes of major phases in the cement paste model need to be determined prior to the homogenization process.

The volume of major hydrated cement phases was presented by Powers and Brownyard (1948, 1960) and Jennings and Tennis (1994). Whereas Powers' model can only predict the volume of unreacted cement, Jennings' model can estimate the relative amount of unreacted C–S–H and CH. Highlights of the Jennings model are summarized as Eqs. (1)–(4):

$$V_{\text{unreactedcement}} = c\,(1 - \alpha_{\text{total}}) \left(\frac{1}{\rho_{\text{cement}}} \right) \quad (1)$$

$$V_{\text{CH}} = c(0.189\alpha_1 p_1 + 0.058\alpha_2 p_2) \quad (2)$$

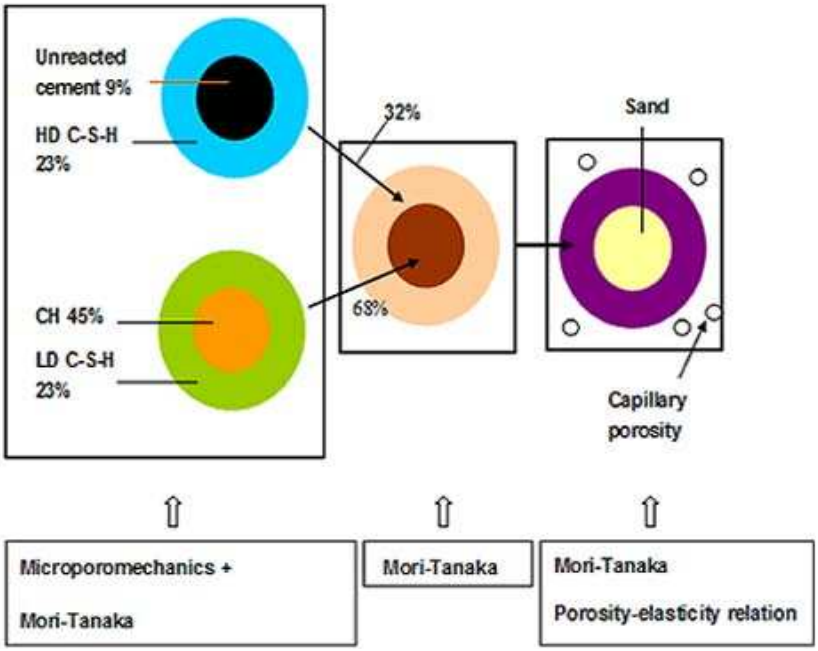

FIG. 3: Proposed cement paste and mortar model for w/c of 0.4.

$$V_{\mathrm{AFm}} = c(0.849\alpha_3 p_3 + 0.472\alpha_4 p_4) \tag{3}$$

$$V_{\mathrm{CSH\ Solid}} = c(0.278\alpha_1 p_1 + 0.369\alpha_2 p_2) \tag{4}$$

where $V_{\mathrm{unreacted\,cement}}$, V_{CH}, V_{AFm}, and V_{CSHsolid} are the volumes of unreacted cement, CH, AFm, and solid C–S–H material in 1 g of cement paste, respectively, and; is the initial weight of the cement, defined by

$$c = \frac{1}{1 + w_0/c} \tag{5}$$

where p_i is the percent of *i*th phase (C_3S: i = 1, C_2S: i = 2, C_3A: i = 3, and C_4AF: i = 4) in the unreacted cement, and α_i is the degree of hydration of the four cement constituents, expressed as

$$\alpha_i = 1 - \exp\left(-a_i\,(t - b_i)^{c_i}\right) \tag{6}$$

In the above, a_i, b_i, and c_i are constants determined by Taylor (1987), and t is the age of the hydrated cement. The composition of cement used in this paper is shown in Table 1. The water-to-cement ratio w_0/c used is 0.4. Two types of C–S–Hs can be distinguished with the ratio 1:1, based on Dormieux and Ulm (2005). The calculated volume fractions of different components using Jennings' model are shown in Fig. 3.

TABLE 1: Composition of cement constituents.

Phases	*WP* (%)	*VP* (%)
C_3S	73.9	73
C_2S	12.3	10
C_3A	6.3	8.8
C_4AF	7.5	8.2

WP: weight percentage
VP: volume percentage

4. NANOSCALE: MD SIMULATION OF NANOPARTICLES

Understanding the properties of basic constituents of materials is the first step in multiscale modeling. With the recent advancement in experimental techniques, more insight has been gained into concrete's nanostructure.

At nanoscale (see level 1 in Fig. 1), the mechanical properties of nanoparticles of C–S–H, CH, cement constituents, and sand are calculated using MD simulations. The corresponding crystalline structures of these materials are shown in Fig. 4.

MD is a computational technique that models the behavior of molecules. The force fields of computational chemistry and materials science are applied for studying

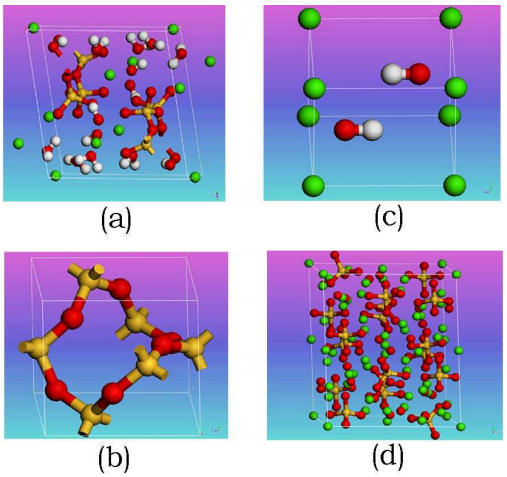

FIG. 4: Unit cell of crystalline structure of **(a)** jennite (C–S–H), **(b)** calcium hydroxide (CH), **(c)** alpha quartz (sand), and **(d)** C_3S (cement).

small chemical molecular systems and material assemblies. The common feature of molecular modeling techniques is that the system is at the atomistic level; this is in contrast to quantum chemistry which applies quantum mechanics and quantum field theory (Lowe, 1993). The main benefit to molecular modeling is in allowing more atoms to be considered compared to quantum chemistry during the simulation. This is accomplished by starting with a small number of molecules and persistently increasing the unit cell size until a periodic system is reached, which represents the full-scale material properties. The procedure recommends simulating unit cells with 3000 atoms or more in order to reach the periodic unit cell that represents the infinite system.

For MD simulation, commercially available software Materials Studio (Accelrys, Inc., 2008) was utilized to estimate the mechanical properties of nanoparticles of Portland cement and hydrated cement nanoparticles. More detail on MD simulations are reported in Wu et al. (2010a, b).

5. SUB-MICROSCALE: MICROPOROMECHANICS CALCULATION OF EFFECTIVE PROPERTIES OF LD AND HD C–S–H

Microporomechanics is a useful tool to study the mechanics and physics of multiphase porous materials (Dormieux et al., 2006). At the second level of this study (see Fig. 1), properties of C–S–H gels are computed using microporomechanics. C–S–H gel is a porous material with 37% (LD) and 24% (HD) porosity (Jennings, 2000). According to Dormieux and Ulm (2005) the poroelastic properties of LD and HD C–S–H can be calculated using the following relations:

$$K = G_s \frac{4\,(1-\phi_0)}{3\phi_0 + 4(G_s/K_s)} \tag{7}$$

$$G = G_s \frac{(1-\phi_0)\,(8G_s + 9K_s)}{6\phi_0(2G_s + K_s) + 8G_s + 9K_s} \tag{8}$$

where K and G are effective bulk and shear moduli; G_s and K_s are shear and bulk modulus of the solids obtained from MD simulation; and ϕ_0 is the porosity. The properties of LD and HD C–S–H are estimated in Wu et al. (2008a,b).

6. MICROSCALE: HOMOGENIZATION OF HD C–S–H WITH RESIDUAL CEMENT AND LD C–S–H WITH CH

The two-phase sphere micromechanics model (Abudi, 1991) is utilized to estimate the effective properties of level 3 composites: composite 1 (1–1, and 1–2). The volume fraction of unreacted cement in the composite 1–1 is given by

$$\begin{aligned} VF_{\text{unreacted cem}} &= \frac{VF_{\text{unreacted cem}}}{VF_{\text{unreacted cem}} + VF_{\text{HD CSH}}} \\ &= \frac{9\%}{9\% + 23\%} = 0.281 \end{aligned} \tag{9}$$

Obtained results for composite 1 (1–1, and 1–2) are shown in Table 2.

In order to compute the effective properties of cement paste, the M-T micromechanics model is used to homogenize two composites: unreacted cement-HD C–S–H and CH-LD CSH shown in Table 2. The volume fraction of inclusion (CH-LD CSH) in this model $VF_{\text{CH-LDCSH}}$ is taken as 0.68, since VF_{CH}=45% and $VF_{\text{LD-CSH}}$ = 23%. Therefore, the effective properties of cement paste with zero porosity (e.g., Young's modulus, E_o, Poisson's ratio, ν_o, bulk modulus, K_o, and shear modulus, G_o) are calculated as

$$E_0 = 43.1 \text{ GPa} \quad \nu_0 = 0.3 \quad K_0 = 35.9 \text{ GPa}$$
$$G_0 = 16.6 \text{ GPa}$$

TABLE 2: Computation of mechanical properties of composites: unreacted cement/HD CSH, and CH/LD C–S–H.

Composite (inclusion/matrix)	VF_i	E_i	ν_i	E_m	ν_m	E_{eff}	ν_{eff}
Unreacted cement/HD CSH	0.281	56.6§	0.29	41	0.3	44.87	0.3
CH/LD CSH	0.662	50.02	0.31	30.8	0.29	42.31	0.3

* The unit in this table is GPa except for *VF* and ν.

§ Cement particles porosity effect considered as $E = E_0 e^{-3.4\phi} = 137e^{-3.4(0.26)} = 56.6$ GPa.

7. MACROSCALE: EFFECTIVE PROPERTIES OF MORTAR AND CONCRETE

7.1 Elastic Properties–Porosity Relation

Porosity is one of the most important factors which affect the strength of cement paste. Many analytical or semianalytical equations may be used to describe the moduli-porosity relation of a porous material. A good summary of these equations is given by Yoshimura et al. (2007). For reference, selected relations are listed in Table 3.

Knudsen (1959) proposed an empirical equation to define the relation between mechanical strength and porosity. Relation no. 1 in Table 3 is the Knudsen law, which is the one most widely used. Porosity has a great influence on the effective properties of concrete, as stated by Mehta (1986).

The effective properties of hydrated cement paste calculated using Eqs. (1)–(4) in Table 3 are given in Table 4. The Young's moduli of hydrated cement paste (HCP) fall in the range of 15.4–23.7 GPa. Poisson's ratio computed by Eqs. (3) and (4) is 0.27. The results in Table 4 are used as the input parameters for next-level computation to obtain properties of mortar.

7.2 Effective Properties of Mortar

M-T micromechanics theory is used to compute the effective properties of composite mortar (composite 3 in Fig. 3) in which sand (alpha quartz) is considered the inclusion and cement paste is the matrix. The volume fraction of the sand used in the calculation is 1/3 of the total volume of mortar. The homogenization results for mortar are given in Table 5.

7.3 Effective Properties of Concrete

Two micromechanics models are used to calculate the effective properties of concrete: generalized method of cell

TABLE 3: Selected elastic constants-porosity relations (after Yoshimura et al. 2007).*

Eq.	Author (year)	Elastic constants–porosity relation
1	Knudsen (1959)	$E = E_0 e^{(-k\phi_0)}$
2	Helmuth and Turk (1966)	$E = E_0(1-\phi_0)^k k = 3$
3	Kerner (1952)	$G = G_0(1-\phi_0)(7-5\nu_0)/[\phi_0(8-10\nu_0)+7-5\nu_0]$ $K = 4K_0G_0(1-\phi_0)/(4G_0+3\phi_0K_0)$
4	Hashin (1962)	$E = E_0(1-\phi_0)/\{1+(1+\nu_0)(13-15\nu_0)\phi_0/[2(7-5\nu_0)]\}$ $G = G_0(1-\phi_0)/[1+2(4-5\nu_0)\phi_0/(7-5\nu_0)]$ $K = K_0(1-\phi_0)/\{1+(1+\nu_0)\phi_0/[2(1-2\nu_0)]\}$

*Constant *k* in Eq. (1) follows Velez et al. (2001) and *k* = 3.4. $-K_0$, G_0, and ν_0 are from the calculated results of cement paste in Section 6. Porosity in this study $\varphi_0 = 8.1\%$

TABLE 4: Effective properties of hydrated cement paste.

No.	E_0(GPa)	Eq. in Table 3	E_{hcp}(GPa)	ν_{hcp}
1	43.1	1	16.1	-
2		2	15.4	-
3		3	23.7	0.27
4		4	23.7	0.27

TABLE 5: Effective properties of mortar.

Case	Matrix (Cement paste)			Inclusion (sand)			Mortar	
	E	*K*	*G*	*E*	*K*	*G*	*E*	ν
1	23.7	17.17	9.33	98.66	42.05	44.48	47.4	0.21
2	23.7	17.17	9.33	62.5	42.05	44.48	39	0.24

Unit in this table is GPa, except for Poisson's ratio.

(GMC) (NASA, 2002; Aboudi, 1989; Aboudi, 1996) and the lattice model. Both methods may be applied to composites with irregular shape inclusions and different packing arrangements.

The lattice model (spring network) has been utilized to compute effective elastic moduli and simulate crack formation in materials (Ostoja-Starzewski, 2002; Alkateb et al., 2009). In this paper, regular triangular lattices with linear central springs (Fig. 5) are adopted. Elastic moduli of individual phases are mapped into spring stiffness according to the formula

$$C_{ijkl} = \frac{\alpha}{2\sqrt{3}} \sum_{n=1}^{6} l_i^n l_j^n l_k^n l_l^n \tag{10}$$

where $l_1 = \cos\theta$, $l_2 = \sin\theta$ are the direction of the spring, and α is the spring constant.

The springs' stiffnesses are assigned according to the following criteria: if the spring falls within the inclusion boundary it is assigned a stiffness k_i; if it falls within the matrix boundaries it is assigned a stiffness k_m; for any bonding spring connecting both phases, it is assigned a stiffness k_b. The values of k_i and k_m are calculated according to the individual phase's elastic properties according to Eq. (12):

$$C_{1111} = C_{11} = \frac{3\sqrt{3}}{8}\alpha, \quad C_{1122} = C_{12} = \frac{\sqrt{3}}{8}\alpha, \quad C_{1212} = C_{66} = \frac{\sqrt{3}}{8}\alpha \tag{11}$$

A lattice used in the computation is shown in Fig. 6.

The effective properties of concrete are computed by GMC and the lattice model, and are given in Table 6. The Young's moduli given by GMC and the lattice model are 42 GPa and 36.3 GPa, respectively.

8. RESULTS VALIDATION

To validate the numerical results of this study, RUS is employed to measure the elastic constants of hydrated cement paste. RUS is a modern nondestructive acoustic

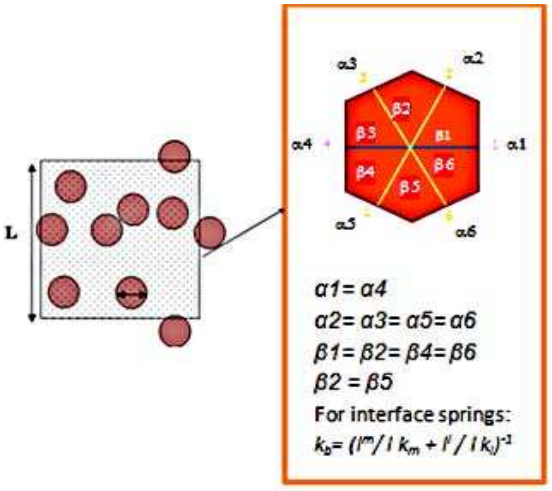

FIG. 5: Fine mesh spring network with a zoom-in for a unit cell.

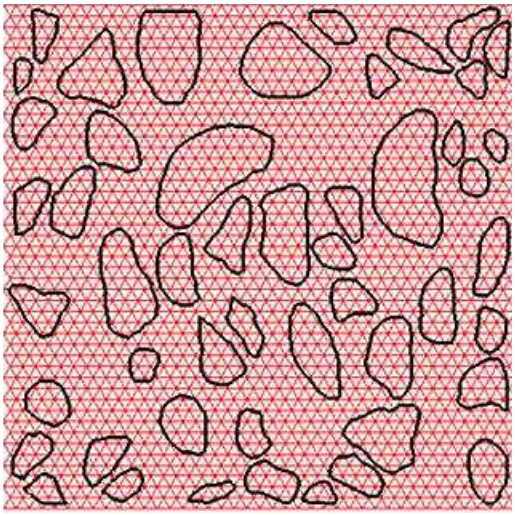

FIG. 6: Spring network mesh of concrete.

TABLE 6: Effective elastic moduli of concrete by GMC and lattice model.

E_{mortar}	39
E_{agg}	46.6*
$E_{\text{con eff}}$: GMC	42
$E_{\text{con eff}}$: lattice	36.3

*Properties of concrete estimated from elastic-porosity relation $\mathrm{E} = \mathrm{E}_0 e^{(-k\phi_0)} = 98.66e^{(-3)(0.25)} = 46.6$, where E_0 is the modulus of quartz, ϕ_0 is the porosity of aggregate, and $E_{\text{con\_eff}}$ is the effective Young's modulus of concrete. The unit in this table is GPa.

technique which can be used to measure the elastic properties of solids with high precision (Migliori et al., 1993, 1990). RUS measures the eigenmodes of vibration of parallelepiped, spherical, or cylindrical samples. An RUS instrument is shown in Fig. 7.

RUS test samples were prepared and cured according to ASTM standard C192. The water-to-cement ratio w_0: c is 0.4. The amount of cement used in each cubic meter cement paste is 325 kg. Although the samples can be of different shapes, this research used an accurately shaped parallelepiped sample. The water-to-cement ratio for the samples is the same as used in the concrete specimens, 0.4.

To perform the test, the two corners of the test sample were carefully placed between two transducers. Next, one of the two transducers applied the vibrations to the sample using the frequency sweeping technique and the other recorded the frequency amplitude of the sample's response in terms of the natural frequencies. Finally, the elastic constants were determined (Maynard, 1996).

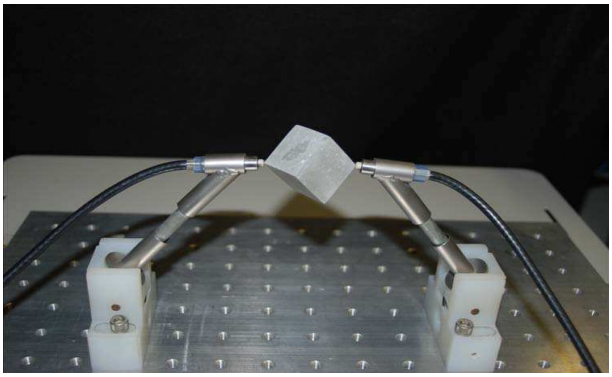

FIG. 7: A room temperature RUS system with a cement paste sample.

The elastic constants measured by RUS for a hydrated specimen with water-to-cement ratio of 0.4 and porosity of 8.1% are an elastic modulus E of 21.55 GPa, and the Poisson's ratio ν of 0.22, which agree quite well with the computed results in Table 3. More details on the RUS measurement of hydrated cement paste are reported in the authors' recent paper (Wu et al., 2009).

The Young's modulus of concrete was obtained by the ASTM C469 standard test method for static modulus of elasticity and Poisson's ratio of concrete in compression using a concrete compression machine. The volume of aggregate in unit volume of concrete is 0.72. Laboratory tests give the results of Young's modulus for concrete as 38.2 GPa, which matches the values given by GMC and lattice model: 42 and 36.3 GPa.

9. CONCLUSIONS

A multiscale simulation methodology was developed to relate the nanoscale constituent properties of cement concrete to its micro- and macroscale properties. Nanoscale properties were obtained using MD simulation; microscopic properties were obtained using microporomechanics theory; and macroscopic properties were obtained using M-T composite theory. Concrete properties were obtained using GMC/HFGMC approaches. Throughout these simulations, lower scale results were used as the input data for higher scale simulations. The input parameters for MD simulation were obtained from the fundamental physical–chemical properties of constituting elements. The simulated results are compared with experimental results and showed quite good agreement at each calculation level. Therefore, it is demonstrated that the hierarchical approach used in this study can be a powerful tool to investigate the properties of cement concrete from nanoscale to macroscale. Ultimately, the goal is to utilize such tools for the design of concrete that is stronger and more environmentally friendly.

ACKNOWLEDGEMENTS

This work was partially supported by funding received under a subcontract from the Department of Homeland Security–sponsored Southeast Region Research Initiative (SERRI) at the Department of Energy's Oak Ridge National Laboratory, USA.

REFERENCES

Aboudi, J., Micromechanical analysis of composites by the method of cells, *Appl. Mech. Rev.*, vol. **42**(7), pp. 193–221,

1989.

Aboudi, J., Micromechanical analysis of composites by the method of cells—Update, *Appl. Mech. Rev.*, vol. **49**(10), pp. S83–S91, 1996.

Abudi, J., *Mechanics of Composite Materials—A Unified Micromechanical Approach*, The Netherlands: Elsevier, 1991.

Accelrys, Inc., *Materials Studio 4.2* [software], San Diego, CA, 2007.

Aligizaki, K. K., Pore structure of cement-based materials: Testing interpretation and requirements (modern concrete technology), pp. 5–9, New York: Taylor & Francis, 2005.

Alkateb, H., Alzebdeh, K. I., and Al-Ostaz, A., Stochastic models for predicting the strength and crack propagation of random composites, *Composites: B*, vol. **40**(1), pp. 7–16, 2009.

Bentz, D. P., Garboczi, E. J., Jennings, H. M., and Quenard, D. A., Multi-scale digital-image-based modeling of cement-based materials, *Microstructure of Cement-Based Systems/Bonding and Interface in Cementitious Materials, Materials Research Society Symposium Proceedings*, vol. **370**, pp. 33–42, 1995.

Bernard, O., Ulm, F.-J., and Lemarchand, E., Multiscale micromechanics-hydration model for the early-age elastic properties of cement-based materials, *Cement Concrete Res.*, vol. **33**(9), pp. 1293–1309, 2003.

Constantinides, G. and Ulm, F.-J., The nanogranular nature of C–S–H, *J. Mech. Phys. Solids*, vol. **55**, pp. 64–90, 2007.

Dormieux, L. and Ulm, F.-J., *Applied Micromechanics of Porous Materials*, CISM Courses and Lectures, New York: Springer, Wien, 2005.

Dormieux, L., Kondo, D., and Ulm, F.-J., *Microporomechanics*, England: Wiley & Sons, 2006.

Feldman, R. F. and Sereda, P. J., A new model of hydrated cement and its practical implications, *Eng. J. Can.*, vol. **53**, pp. 53–59, 1970.

Feng, L. and Christian, M., Micromechanics model for the effective elastic properties of hardened cement pastes, *Acta Materiae Compositae Sinica*, vol. **24**(2), pp. 184–189, 2007.

Fish, J. and Shek, K., Multiscale analysis of composite materials and structures, *Compos. Sci. Technol.*, vol. **60**(12-13), pp. 2547–2556, 2000.

Fish, J. and Yu, Q., Computational mechanics of fatigue and life predictions for composite materials and structures, *Comput. Methods Appl. Mech. Eng.*, vol. **191**(43), pp. 4827–4849, 2002.

Fish, J., Wu, W., and Yuan, Z., Eigen deformation-based homogenization of concrete, *Int. J. Multiscale Comput. Eng.*, vol. **8**(1), pp. 1–15, 2010.

Gates, T. S., Odegard, G. M., Frankland, S. J. V., and Clancy, T. C., Computational materials: Multi-scale modeling and simulation of nanostructured materials, *Compos. Sci. Technol.*, vol. **65**, pp. 2416–2434, 2005.

Haecker, C.-J., Garboczi, E. J., Bullard, J. W., Bohn, R. B., Sun, Z., Shah, S. P., and Voigt, T., Modeling the linear elastic properties of Portland cement paste, *Cement Concrete Res.*, vol. **35**(10), pp. 1948–1960, 2005.

Hashin, Z., The elastic moduli of heterogeneous materials, *J. Appl. Mech.*, vol. **29**, pp. 143–162, 1962.

Helmuth, R. A. and Turk, D. H., Elastic moduli of hardened Portland cement and tricalci silicate paste: Effect of porosity, *Symp. Strict. Portland Cem. Paste Concr.*, pp. 135–144, 1966.

Jasiuk, I. M., Trabecular bone as a hierarchical material: Elasticity and fracture, *Proc. of the 2005 Summer Bioengineering Conf.*, pp. 908–909, 2005.

Jennings, H. M., A model for the microstructure of calcium silicate hydrate in cement paste, *Cement Concrete Res.*, vol. **30**, pp. 101–116, 2000.

Jennings, H. M., Colloid model of C–S–H and implications to the problem of creep and shrinkage, *Materials and Structures: Special Issue of Concrete Science and Engineering on Poromechanics of Cement Based Materials*, vol. **37**, pp. 59–70, 2004.

Jennings, H. M. and Tennis, P. D., Model for the developing microstructure in Portland cement pastes, *J. Am. Ceram. Soc.*, vol. **77**(12), pp. 3161–3172, 1994.

Kerner, E. H., The elastic and thermo-elastic properties of composite media, *Proc. Roy. Soc. (London) Ser.*, B69, pp. 808–813, 1952.

Knudsen, F. P., Dependence of mechanical strength of brittle polycrystalline specimens on porosity and grain size, *J. Am. Ceram. Soc.*, vol. **42**(8), pp. 376–387, 1959.

Leisure, R. G. and Willis, F. A., Resonant ultrasound spectroscopy, *J. Phys.: Condens. Matter.*, vol. **9**, pp. 6001–6029, 1997.

Li, A., Li, R., and Fish, J., Generalized mathematical homogenization: From theory to practice, *Comput. Methods Appl. Mech. Eng.*, vol. **197**(41–42), pp. 3225–3248, 2008.

Maynard, J., Resonant ultrasound spectroscopy, *Physics Today*, vol. **49**, pp. 26–31, 1996.

Mehta, P. K., *Concrete, Structure, Properties, and Msaterials*, Englewood Cliffs, NJ: Prentice-Hall, 1986.

Migliori, A., Sarrao, J. L., Visscher, W. M., Bell, T. M., Lei, M., Fisk, Z., and Leisure, R. G., Resonant ultrasound spectroscopic techniques for measurement of the elastic moduli of solids, *Physica B.*, vol. **183**, pp. 1–24, 1993.

Migliori, A., Visscher, W. M., Brown, S. E., Fisk, Z., Cheong, S.-W., Alten, B., Ahrens, E. T., Kubat-Martin, K. A., Maynard, J. D., Huang, Y., Kirk, D. R., Gillis, K. A., Kim, H. K., and Chan, M. H. W., Elastic constants and specific-heat measurements on single crystals of La_2CuO_4, *Phys. Rev. B.*, vol. **41**(4), pp. 2098–2102, 1990.

NASA John H. Glenn Research Center, *MAC/GMC* computer software, Cleveland, OH: Lewis Field, 2002.

Ostoja-Starzewski, M., Lattice models in micromechanics, *Appl. Mech. Rev*., vol. **55**(1), pp. 35–60, 2002.

Powers, T. C., Physical properties of cement paste, *Proc. of the Fourth Int. Symp. on the Chemistry of Cement*, pp. 577–613, 1960.

Powers, T. C. and Brownyard, T. L., Studies of the physical properties of hardened Portland cement paste, *PCA Bull.*, Issue 22, 1948.

Taylor, H. F. W., Proposed structure for calcium silicate hydrate gel, *J. Am. Ceram. Soc*., vol. **69**, pp. 464–467, 1986.

Taylor, H. F. W., A method for predicting alkali ion concentration in cement pore solutions, *Adv. Cem. Res*., vol. **1**(1), pp. 5–7, 1987.

Taylor, H. F. W., Nanostructure of C–S–H: Current status, *Advanced Cement Based Mater.*, vol. **1**, pp. 38–46, 1993.

Tennis, P. D. and Jennings, H. M., A model for two types of calcium silicate hydrate in the microstructure of Portland cement pastes, *Cement Concrete Res.*, vol. **30**(6), pp. 855–863, 2000.

Ulm, F.-J., Constantinides, G., and Heukamp, F. H., Is concrete a poromechanics material?—A multiscale investigation of poroelastic properties, *Mater. Struct./Concrete Sci. Eng.*, vol. **37**, pp. 43–58, 2004.

Velez, K., Maximilien, S., Damidot, D., Fantozzi, G., and Sorrebtino, F., Determination by nanoindentation of elastic modulus and hardness of pure constituents of Portland cement clinker, *Cement Concrete Res.*, vol. **31**(4), pp. 555–561, 2001.

Wu, W., Al-Ostaz, A., Cheng, A.H.-D., and Song, C. R., A molecular dynamics study on the mechanical properties of major constituents of Portland cement, *J. Nanomech. Micromech.*, 2010a.

Wu, W., Al-Ostaz, A., Cheng, A. H.-D., and Song, C. R., A molecular dynamics and microporomechanics study on the mechanical properties of major constituents of hydrated cement, *Composite B*, vol. **41**(7), pp. 543–549, 2010b.

Wu, W., Al-Ostaz, A., Gladden, J., Cheng, A., and Li, G., Measurement of mechanical properties of hydtated cement paste using resonant ultrasound spectroscopy, *J. ASTM Int.*, vol. **7**(5), DOI: 10.1520/JAI102657, 2010.

Yoshimura, H. N., Molisani, A. L., and Narita, N. E., Porosity dependence of elastic constants in aluminum nitride ceramics, *Mater. Res.*, vol. **10**(2), pp. 127–133, 2007.

Yuan, Z. and Fish, J., Hierarchical model reduction at multiple scales, *Int. J. Numer. Methods Eng.*, vol. **79**(3), pp. 314–339, 2009.

Journal for Multiscale Computational Engineering 8(6), 597–613 (2010)

EXTENDED MULTISCALE FINITE ELEMENT METHOD FOR MECHANICAL ANALYSIS OF PERIODIC LATTICE TRUSS MATERIALS

H. W. Zhang,* J. K. Wu, & Z. D. Fu

State Key Laboratory of Structural Analysis for Industrial Equipment, Department of Engineering Mechanics, Faculty of Vehicle Engineering and Mechanics, Dalian University of Technology, Dalian 116024, China

*Address all correspondence to H. W. Zhang E-mail: zhanghw@dlut.edu.cn

An extended multiscale finite element method (EMsFEM) is developed to study the equivalent mechanical properties of periodic lattice truss materials. The underlying idea is to construct the numerical multiscale base functions to reflect the heterogeneity of the unit cell of periodic truss materials. To consider the coupled effect among different directions in the multidimensional problems, the coupled additional terms of base functions for the interpolation of the vector fields are introduced. Numerical results show that the base functions constructed by linear boundary conditions will induce nonequilibrium of the boundary nodal forces and thus lead to a strong scale effect of the unit cell in the multiscale computation. Thus, more reasonable oscillatory boundary conditions are introduced by using the oversampling technique in the construction of the multiscale base functions of the unit cell. A special algorithm is introduced to improve the properties of the equivalent stiffness matrix of the unit cell to make the numerical results more accurate. The advantage of the developed method is that the downscaling computation could be realized easily and the stress and strain in the unit cell can be obtained simultaneously in the multiscale computation. Therefore, the developed method has great potential for strength analysis of heterogeneous materials.

KEY WORDS: *multiscale finite element method, truss material, homogenization method, downscaling computation, base function*

1. INTRODUCTION

Motivated by recent advances in manufacturing techniques, ultralight materials are becoming an essential part of present engineered materials, because they offer advantages such as light weight, ease of construction, high stiffness, and high strength (Evans et al. 2001). As one of the most attractive ultralight materials, lattice truss material has received more and more attention for its high stiffness-to-weight and strength-to-weight ratios in the past few years (Brittain et al., 2001; Wadley, 2006) and has been widely used in aeronautic engineering structures (Huybrechts et al., 2002). A lattice truss structure consists of only two force members which are connected together at their ends by pin joints [Fig. 1(a)]. It is composed of many periodic cells which can be decomposed in elementary bars [Fig. 1(b)]. Much research has already been done on mechanical properties of lattice truss materials. Deshpande et al. (2001) investigated the effective mechanical properties of the octet-truss lattice structured material, both experimentally and theoretically. They found that the strength and stiffness of the octet-truss material are stretching-dominated and compare favorably with the corresponding properties of metallic foams; thus, this material may become a substitute metallic foams in lightweight structures.

When a direct numerical method such as the finite element method (FEM) is used to solve large lattice truss structure problems, the degrees of freedom of the resulting discrete system will be too large to be managed, even with the help of high-speed modern computers. It will need a tremendous amount of memory storage and computing time. On the other hand, in engineering practice, it is often sufficient to predict the averaged effect of small

1543–1649/10/$35.00

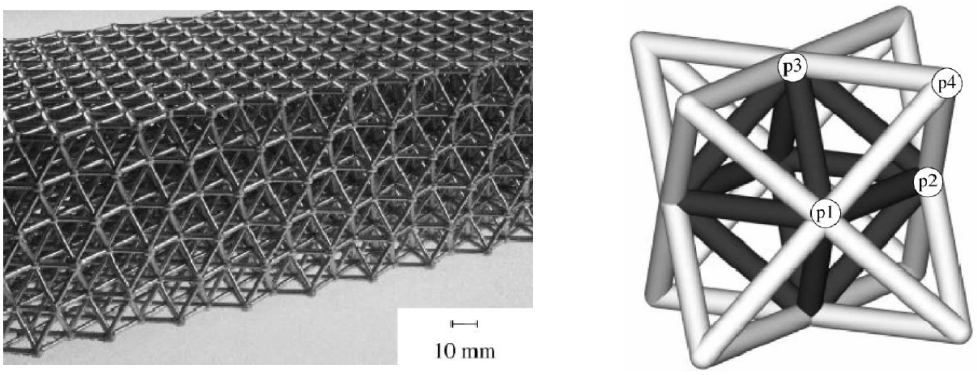

(a) (b)

FIG. 1: (a) Photograph of the octet-truss lattice structure. **(b)** A unit cell of the octet-truss lattice structure. The darkened rods represent an octahedral cell while the nodes labeled p1-p4 form a tetrahedral cell (Deshpande et al., 2001).

scales on large scales for mechanical analysis of complicated materials. Noor (1988) has summarized some commonly used approaches on continuum modeling of repetitive lattice structures. In recent decades, the homogenization method based on double-scale asymptotic expansions has been developed and widely used in multiscale computation of periodic materials (Benssousan et al., 1978; Hassani and Hinton, 1998; Yan et al., 2006; Fish et al., 1997; Yu and Fish, 2002). However, these methods have some limitations. Besides the local periodicity hypothesis, these methods request that the ratio between the small-scale length and the large-scale length be very small.

The multiscale finite element method (MsFEM) has been widely used for numerically solving second-order elliptic boundary value problems with high oscillating coefficients since it was proposed and improved by Hou and Wu (1997), Hou et al. (1999), Chen and Hou (2003), Efendiev and Hou (2007), and Chu et al. (2008). For example, the method has been generalized and successfully used for numerical simulation of two-phase flow in heterogeneous porous media (Hou, 2005; Efendiev et al., 2006; Aarnes, 2004; Aarnes et al., 2006). Recently, Dostert et al. (2008) investigated the MsFEM for the stochastic permeability field as well as application to uncertainty quantification. Moreover, several similar multiscale methods have been developed, such as the multiscale finite volume method (Jenny et al., 2003) and the finite volume multiscale finite element method (He and Ren, 2005). However, fewer works discuss vector field problems of computational solid mechanics. Zhang et al. (2009) seems to be the first work in which the MsFEM was developed for solving the coupling problems of consolidation of heterogeneous saturated porous media under external loading conditions. The main idea of the MsFEM is to construct finite element base functions numerically which can capture the small-scale information in each coarse-scale element by locally solving Dirichlet boundary value problems. The effect of small-scale properties is correctly captured via these base functions. Thus, the method provides an effective way to capture the large-scale solutions on a coarse-scale mesh without resolving all the small-scale features. However, it seems that the method will face some difficulties when it is extended to deal with the problems in solid mechanics where the bulk expansion/contraction phenomena need to be considered in the construction of the base functions.

In this paper, the extended multiscale finite element method (EMsFEM) is developed for numerical homogenization of lattice truss materials. To consider the coupled effect among different directions in the multidimensional problems, the coupled additional terms of base function for the interpolation of the displacement field are introduced. We demonstrate, through extensive numerical experiments, that the small-scale features induced by heterogeneities of truss stiffness can be well captured via this technique. However, from our computational experience, it can also be observed that the construction of base functions with linear boundary conditions will lead to scale effects in some cases. This is induced by nonequilibrium of the boundary nodal forces of the unit cells. To overcome this difficulty, an adaptive oversampling technique is proposed to construct more accurate boundary condi-

tions for unit cells in the construction of the multiscale base functions.

Different from other homogenization methods, the results obtained from the EMsFEM can not only represent the mean field solution of the heterogeneous materials in homogeneous level, but also reflect well the local mechanical behavior of the materials in the microlevel. That is to say, the method developed here can be directly used for downscaling computation, and the real stress and strain within the unit cell can be obtained simultaneously in the multiscale computation. Thus, the EMsFEM developed here has great potential for strength analysis of heterogeneous materials and is applicable to general nonlinear problems.

Our method can also be extended to solve nonperiodic solid materials. However, for simplicity and as the first step of the research work of the EMsFEM, only 2D periodic truss materials are considered in this paper, so that some basic properties of the method could be explored. The numerical experiments show that the results obtained by the EMsFEM agree well with the reference solutions. Moreover, it reduces the computational cost and memory storage drastically.

This paper is organized as follows: In the next section, a brief overview of the multiscale finite element is presented first, and then in Section 2 the construction process of the base functions with a linear boundary condition for the unit cell of lattice truss materials is discussed in detail, from which the unit cell's equivalent stiffness matrix is deduced. In Section 3, the representative volume element (RVE) method is briefly introduced. In Section 4, four representative numerical examples are carried out for the comparison of our multiscale method with the RVE method and standard finite element method. In Section 5 we analyze the scale effect and source of error of the EMsFEM with linear boundary conditions. Then more reasonable oscillating boundary conditions are constructed using the oversampling technique in Section 6, and a special numerical algorithm is applied to modify the equivalent stiffness matrix obtained with the oscillatory boundary conditions. In Section 7, downscaling computation is carried out to get internal forces of truss elements in fine-scale mesh. Finally, some discussion is presented.

2. EXTENDED MULTISCALE FINITE ELEMENT METHOD (EMSFEM)

In this section, the numerical procedure of the EMsFEM for mechanical analysis of periodic truss materials is described. We first briefly review the principle idea of the standard multiscale finite element method. Then the construction processes of the multiscale base functions for the unit cell of periodic truss materials are presented. Finally, the equivalent stiffness matrix of the unit cell is derived with the use of the base functions.

2.1 Overview of MsFEM

The MsFEM was first developed by Hou and Wu (1997) to solve the elliptic equations with multiscale coefficients. It provides an effective way to capture the large-scale solutions on a coarse-scale mesh without resolving all the small-scale features. This is accomplished by constructing the multiscale base functions that are adaptive to the local property of the differential operator. The small-scale information is then brought to the large scales through the coupling of the global stiffness matrix, and the effect of small scales on the coarse scales is correctly captured. Thus, the finite element method needs only to be handled on the coarse-scale meshes. It greatly reduces the degrees of freedom. The method is applicable to the general multiple-scale problems without restrictive assumptions. The construction of base functions is fully developed from element to element. Thus, the method is perfectly parallel and is naturally adapted to massively parallel computers. Motivated by previous works, in this paper the original MsFEM is extended to the mechanical analysis of truss materials.

2.2 The Base Functions of Unit Cell of Periodic Truss Materials

Since the solid deformation is cross-coupling among different spatial directions for the influence of Poisson's effect, the main difficulty of the EMsFEM is how to construct finite element base functions which can accurately capture the small-scale heterogeneities of the unit cell. For the displacement field of the truss unit cell, in order to consider the heterogeneity in the unit cell, the base functions must be constructed separately for each coordinate direction. In two-dimensional problems (2D), two kinds of base functions for interpolation of the displacement field of the 2D truss structures are constructed in which one is used for the displacement interpolation in x-direction and the other is used for y-direction. The base functions are constructed by solving the equilibrium equation in each fine-scale mesh within the unit cell with some specified boundary conditions. Hou and Wu et al. (1997, 1999) demonstrated that the boundary conditions of the base functions have a big influence on the accu-

racy of the multiscale method. This is also suitable for the computation of vector fields. Thus, the linear boundary conditions which were generally used in the standard Ms-FEM are studied here first, and then more accurate boundary conditions, i.e., oscillatory boundary conditions, are proposed to construct the base functions in Section 6.

Without loss of generality, take a truss unit cell as an example (see Fig. 2), where N_i denotes the base function of node i, which satisfies $N_i|_j = \delta_{ij}, (i, j = 1, 2, 3, 4)$, where δ is the Kronecker delta. In the two-dimensional vector field, N_{ix} and N_{iy} are constructed numerically and independently. First, let us consider the construction of N_{1x} as shown in Fig. 3. Our earlier research (Zhang et al., 2009) has introduced a simple method for the construction of base functions of a solid skeleton. As shown in Fig. 3(a), the displacements at all boundary nodes are not constraint in the *y*-axis direction except node 3, for which the displacements are fixed to zero in both coordinate directions in order to avoid rigid displacement. For the linear boundary conditions, a unit displacement is applied on node 1 in *x*-positive direction, and the values vary linearly along boundaries 12 and 14, just as in the standard bilinear (linear) base functions. At the same time, the nodes on boundary 34 and boundary 23 are constraint in the *x*-direction. Using the boundary conditions mentioned above, the internal displacement field of the unit cell can be solved directly by standard finite element analysis in fine-scale mesh, and the base function N_{1x} can be obtained. The rest of the base functions of the truss cell can be constructed in a similar way. It is easy to verify that the base functions constructed above satisfy $\sum_{i=1}^{4} N_{ix} = 1$ and $\sum_{i=1}^{4} N_{iy} = 1$ in the unit cell. In particular, for the homogeneous cell, the values of constructed base functions are equal to those of the standard bilinear base functions of a four-node rectangular element, i.e., for the coordinate system shown in Fig. 4, we have the following relationship when the unit cell is homogeneous

$$N_i = N_{ix} = N_{iy} = \frac{(a + x_0)(b + y_0)}{4ab} \qquad (1)$$

where $x_0 = x_i x/a$, $y_0 = y_i y/b$, and N_i is the bilinear base function of node i.

From our computational results, it can be seen that the construction method mentioned above cannot capture well the small-scale deformation information in the unit

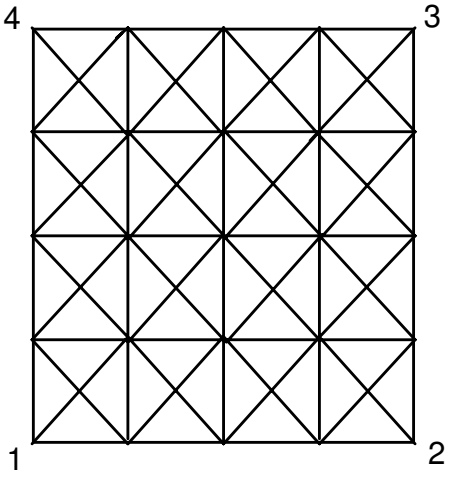

FIG. 2: A truss unit cell.

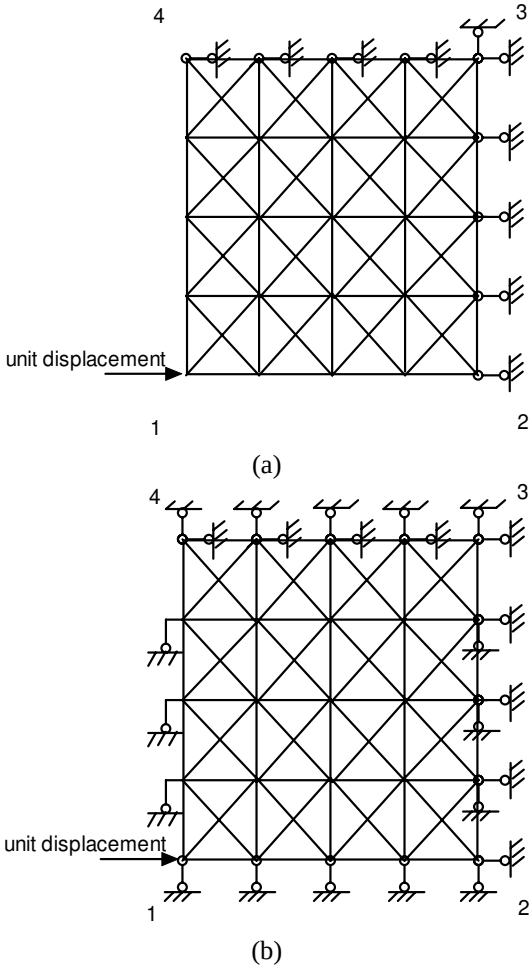

FIG. 3: The construction of base functions for a truss cell: **(a)** boundary constraints in literature (Zhang et al., 2009) and **(b)** boundary constraints in this paper.

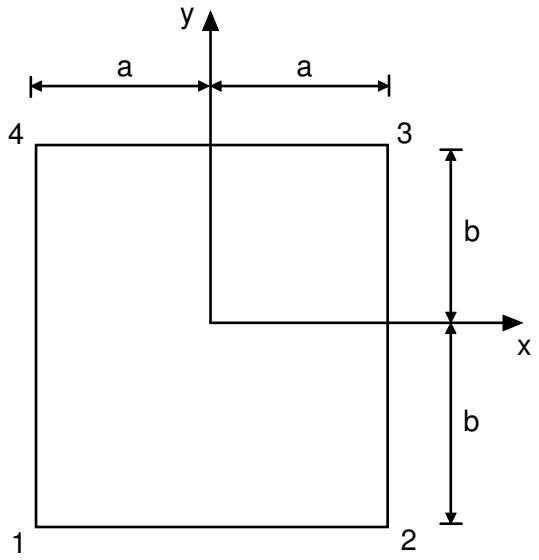

FIG. 4: Bilinear rectangular element.

cell due to Poisson's effect, especially for a heterogeneous unit cell. So in the present study, a new method for the construction of base functions is introduced. In order to consider the coupled effect among different directions in multidimensional problems, the coupled additional terms of base functions are introduced for the interpolation of the vector fields. Different from the previous boundary constraints, the boundary nodes of the cell are all constraint in the *y*-direction in the new construction method, as shown in Fig. 3(b). For the linear boundary conditions, a unit displacement is applied on node 1 in *x*-positive direction, and the values vary linearly along boundaries 12 and 14, just the same as the steps mentioned above. Thus, the base functions N_{1x} and N_{1xy} can be obtained. Unlike the original MsFEM, N_{ixy} is proposed here, which is a coupled additional term and means the displacement field in *y*-direction within the unit cell induced by unit displacement of node i in the *x*-direction.

It can been verified that the base functions constructed above satisfy

$$\begin{cases} \sum_{i=1}^{4} N_{ix} = 1, & \sum_{i=1}^{4} N_{iy} = 1 \\ \sum_{i=1}^{4} N_{ixy} = 0, & \sum_{i=1}^{4} N_{iyx} = 0 \end{cases} \tag{2}$$

which ensures the rigid displacement of the unit cell and the compatibility between the neighboring unit cells.

Once the base functions are constructed, the displacement fields within the unit cell can be expressed as

$$u = \sum_{i=1}^{4} N_{\mathrm{ix}} u'_{\mathrm{i}} + \sum_{i=1}^{4} N_{iyx} v'_i \tag{3}$$

$$v = \sum_{i=1}^{4} N_{\mathrm{iy}} v'_{\mathrm{i}} + \sum_{i=1}^{4} N_{ixy} u'_i \tag{4}$$

Equations (3) and (4) can be given in a unified form

$$\mathbf{u} = \mathbf{N}\mathbf{u}'_{\mathbf{E}} \tag{5}$$

where $\mathbf{N}$ is the base function matrix of the unit cell, $\mathbf{u}$ is the displacement vector of the nodes in the fine-scale mesh, and $\mathbf{u}'_{\mathbf{E}}$ is the displacement vector of the unit cell in macro level. They can be expressed as

$$\begin{aligned} \mathbf{u} &= \begin{bmatrix} u_1 & v_1 & u_2 & v_2 & \cdots & \cdots & u_n & v_n \end{bmatrix}^T \\ \mathbf{N} &= \begin{bmatrix} R_x(1)^T & R_y(1)^T & R_x(2)^T & R_y(2)^T \\ \cdots & \cdots & R_x(n)^T & R_y(n)^T \end{bmatrix}^T \\ \mathbf{u}'_{\mathbf{E}} &= \begin{bmatrix} u'_1 & v'_1 & u'_2 & v'_2 & u'_3 & v'_3 & u'_4 & v'_4 \end{bmatrix}^T \end{aligned} \tag{6}$$

where

$$\begin{aligned} R_x(i) = &\begin{bmatrix} N_{1x}(i) & N_{1yx}(i) & N_{2x}(i) & N_{2yx}(i) \\ & N_{3x}(i) & N_{3yx}(i) & N_{4x}(i) & N_{4yx}(i) \end{bmatrix} \\ R_y(i) = &\begin{bmatrix} N_{1xy}(i) & N_{1y}(i) & N_{2xy}(i) & N_{2y}(i) \\ & N_{3xy}(i) & N_{3y}(i) & N_{4xy}(i) & N_{4y}(i) \end{bmatrix} \end{aligned} \tag{7}$$

and n is the total node number of the fine-scale mesh within a unit cell.

We will demonstrate through extensive numerical examples that the new method is superior to the previous one for constructing base functions of a truss cell and can capture well the small-scale information within the unit cells.

2.3 Equivalent Stiffness Matrix of the Truss Unit Cell

The multiscale base functions are utilized to construct the equivalent stiffness matrix of the truss unit cell. Considering an arbitrary truss element within the unit cell shown in Fig. 5, in the local numbering scheme, the two nodes

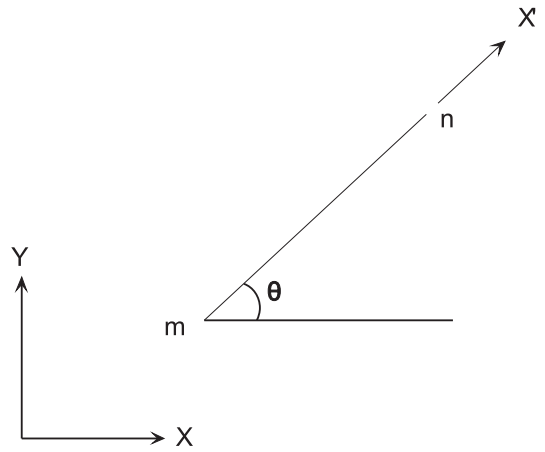

FIG. 5: A two-dimensional truss element.

of the element are numbered *m* and *n*. The global *X*, *Y*-coordinate system is fixed and does not depend on the orientation of the truss element. The element strain energy in local coordinate is given by

$$\pi_e = \frac{1}{2} k_e \Delta l^2 \tag{8}$$

where Δl is the length change of the element and k_e is the elastic coefficient. Both of them can be expressed as

$$\Delta l = \begin{bmatrix} -\cos\theta & -\sin\theta & \cos\theta & \sin\theta \end{bmatrix} \begin{Bmatrix} u_m \\ v_m \\ u_n \\ v_n \end{Bmatrix}, \tag{9}$$

$$k_e = \frac{EA}{l}$$

where E is Young's modulus, A is the element cross-sectional area, and l is the length of the element.

Using Eqs. (5), (6), and (7), we get

$$\begin{Bmatrix} u_m \\ v_m \\ u_n \\ v_n \end{Bmatrix} = \begin{bmatrix} R_x(m) \\ R_y(m) \\ R_x(n) \\ R_y(n) \end{bmatrix} \{\mathbf{u'_E}\} \tag{10}$$

By using Eq. (10), we find that Eq. (9) yields

$$\Delta l = [\mathbf{G}^e] \{\mathbf{u}'_E\} \tag{11}$$

where

$$[\mathbf{G^e}] = \begin{bmatrix} -\cos\theta & -\sin\theta & \cos\theta & \sin\theta \end{bmatrix} \begin{bmatrix} R_x(m) \\ R_y(m) \\ R_x(n) \\ R_y(n) \end{bmatrix} \tag{12}$$

Substituting Eqs. (11) and (12) into Eq. (8), we get

$$\pi_e = \frac{1}{2} \mathbf{u'^T_E} \mathbf{G^{eT}} k_e \mathbf{G^e} \mathbf{u'_E} \tag{13}$$

Adding up the strain energy of all the elements within the unit cell, the total strain energy is obtained as follows

$$\pi_E = \sum_{i=1}^{M} \pi_e^i = \frac{1}{2} \mathbf{u'^T_E} \left[\sum_{i=1}^{M} \mathbf{G^{eiT}} k_e^i \mathbf{G^{ei}} \right] \mathbf{u'_E} \tag{14}$$

where M is the total number of truss elements within the unit cell. It is obvious that the strain energy of the unit cell can be expressed by a displacement vector of four corner nodes, as shown in Eq. (14).

As mentioned above, the equivalent stiffness matrix of the truss unit cell can be expressed as

$$\mathbf{K}_E = \sum_{i=1}^{M} \mathbf{G^{eiT}} k_e^i \mathbf{G^{ei}} \tag{15}$$

Once the equivalent stiffness matrix is obtained, the standard FEM is then able to be implemented on the coarse-scale mesh, which clearly reduces the degrees of freedom in macro-level computation. In particular, for periodic materials, the equivalent stiffness matrix of the unit cell needs only to be solved one time.

3. REPRESENTATIVE VOLUME ELEMENT (RVE) METHOD

As a classical homogenization method, the representative volume element method has been widely used to predict the effective macroscopic property of the heterogeneous materials because of its clear mechanical conception and simplicity. In this paper, the numerical results obtained by the developed method are compared with those obtained by the RVE method. The RVE method has three types of classical boundary conditions: the uniform displacement boundary conditions (Dirichlet type), the uniform traction boundary conditions (Neumann type), and the periodic boundary conditions. Many authors (Yan et al., 2006; Kouznetsova, 2002; Terada et al., 2000; Pecullan et al., 1999) have demonstrated that the apparent properties obtained by application of uniform displacement boundary conditions on a microstructural cell usually overestimate the effective properties, while the uniform traction boundary conditions lead to underestimation. Compared with the above two conditions, the periodic boundary conditions provide a better estimation of the overall properties;

therefore, the periodic boundary conditions are adopted in this work.

The periodic conditions can be expressed as follows:

$$\vec{x}^{+} - \vec{x}^{-} = \mathbf{F_M} \cdot (\vec{X}^{+} - \vec{X}^{-}) \tag{16}$$

where $\mathbf{F_M}$ is the macroscopic deformation (gradient) tensor, $\vec{X}$ is the initial position vector (in the reference domain V_0), $\vec{x}$ is the actual position vector (in the current domain V), index "+" means along the positive X direction, and "-" means along the negative X direction, as shown in Fig. 6.

In the RVE method, the strain energy of effective homogeneous material of the unit cell, $\mathbf{\Phi}_{macro}$, is defined as

$$\mathbf{\Phi}_{macro} = \frac{1}{2}\int_{\mathbf{R}} \sigma : \varepsilon \mathbf{d\Omega} = \frac{1}{2}\bar{\varepsilon} : \mathbf{C} : \bar{\varepsilon} \tag{17}$$

where $\mathbf{C}$ is the effective elastic tensor and $\bar{\varepsilon}$ is the macrostrain of the unit cell.

At the same time, the strain energy of the corresponding truss unit cell is calculated by accumulating the energy of all the truss elements within the unit cell; thus, the equivalent elastic tensor $\mathbf{C}$ can be obtained under the conception of equivalence of strain energy.

4. NUMERICAL EXAMPLES

In this section, four representative numerical examples are presented. The numerical results obtained by the EMsFEM are compared with those obtained by direct finite element solution, which are regarded as reference values. Moreover, the problems are also solved by the RVE method with periodic boundary conditions for comparison, noting that the unit cells used in the EMsFEM and the RVE method are the same. For the EMsFEM, the base functions of the unit cell with linear boundary conditions are constructed by two kinds of methods mentioned in Section 2.2, respectively. Numerical results obtained by these numerical methods are designated as EMsFEM-L1, EMsFEM-L2, FEM-F, and RVE-P, respectively. Furthermore, all these numerical experiments are dimensionless.

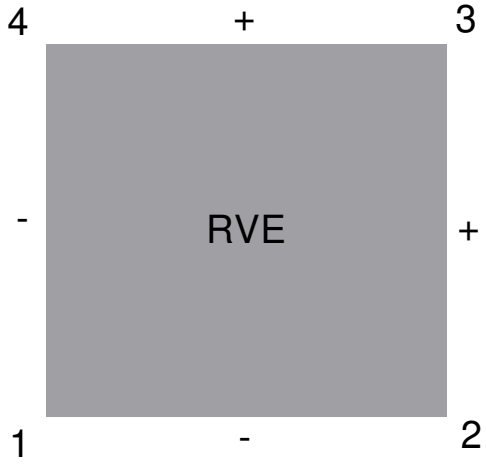

FIG. 6: A typical 2D representative volume element (RVE).

Example 1. For the first numerical example, we consider a truss structure which is composed of $n_x \times n_y = 30 \times 6$ unit cells, where n_x and n_y denote the number of unit cells in the X and Y directions, respectively. The internal elements of the unit cell have the same material properties and cross-sectional areas; thus, the unit cell is homogeneous. The sizes of truss elements in the unit cell are shown in Fig. 7(a). Young's modulus is used as the

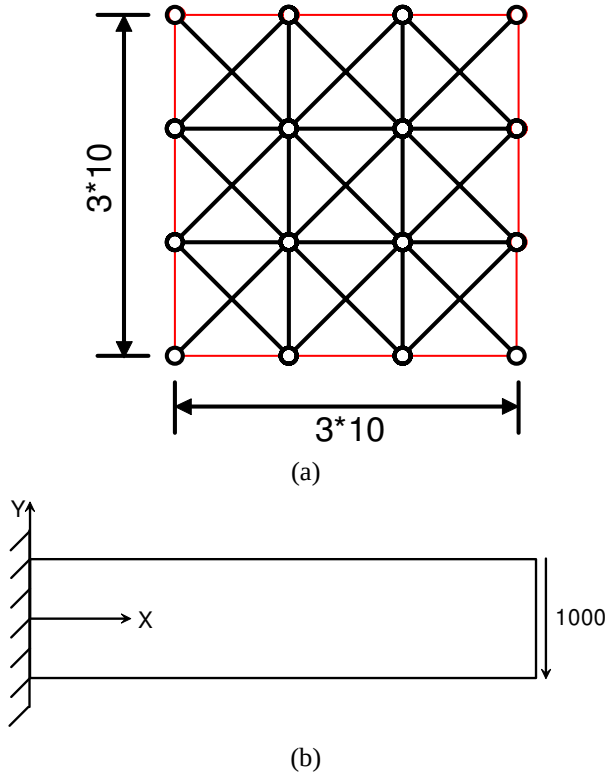

FIG. 7: A truss structure composed of periodic unit cells. **(a)** Homogeneous unit cell. Cross-sectional areas of the outer elements are 0.5, while for internal elements, they are 1.0. **(b)** The loading and constraint conditions.

same in all these examples with a magnitude of 1.0E6. The left side of the truss structure is fixed in the two axis directions, and a uniformly distributed load is applied on the right side, as illustrated in Fig. 7(b). Figure 8 shows the true truss structure and the coarse-scale mesh that is used by the EMsFEM and the RVE method. Figure 9 shows the results of the *Y*-direction displacement of the points on the centroidal plane of the cantilever beam. For the EMsFEM-L2, the maximum relative error is 0.79% compared to the FEM-F. It is superior to the EMsFEM-L1 and the RVE-P, whose errors are 1.90 and 1.80%, respectively, illustrating that the introduction of the coupled additional terms for construction of base functions is very effective. For the homogeneous unit cell, the base functions constructed by EMsFEM-L1 are equal to standard bilinear base functions of a four-node rectangular element. That is to say, for standard FEM, more accurate results will be obtained if the coupled additional terms can be considered in base functions.

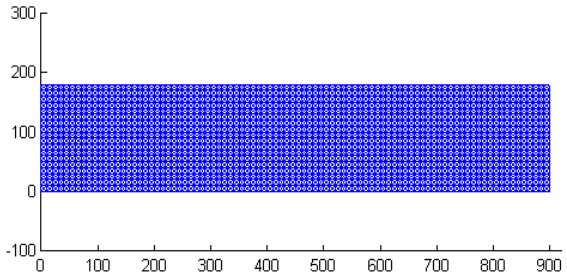

(a) fine-scale mesh

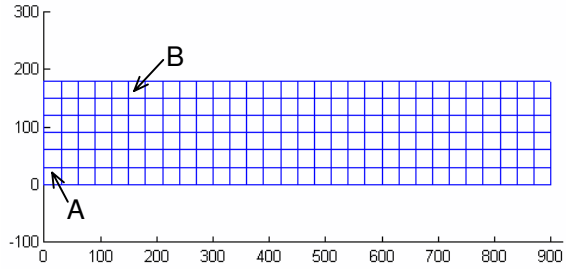

(b) coarse-scale mesh

FIG. 8: The fine- and coarse-scale meshes of the truss structure.

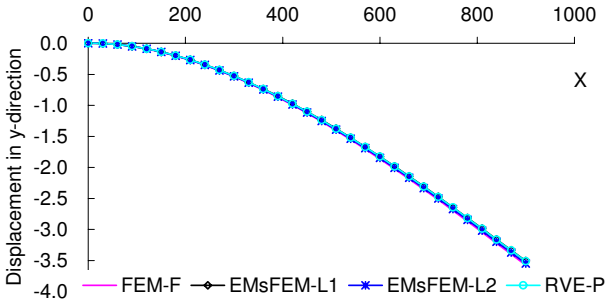

FIG. 9: *Y*-direction displacement of the points on the centroidal plane of cantilever beams.

Example 2. In this example, we consider the same model as example 1, just with the unit cell changed by a new one as illustrated in Fig. 10. The unit cell has only two nodes at each boundary. The numerical results are shown in Fig. 11. It shows that both the EMsFEM-L2 and the RVE-P method give identical results compared to those of the FEM-F, while the EMsFEM-L1 has some errors. For the unit cell with two nodes at each boundary, the boundary conditions do not affect the construction of base functions. So the displacement field within the unit cell is effectively captured by the new construc-

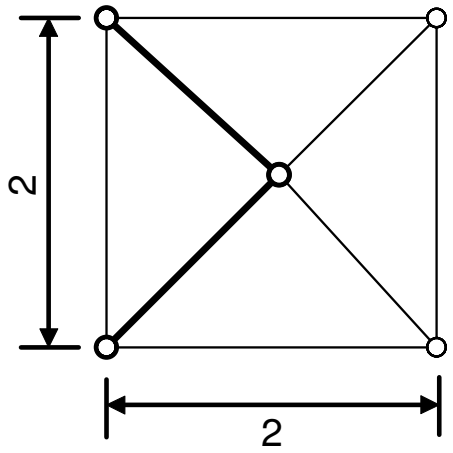

FIG. 10: Heterogeneous unit cell with two nodes at each boundary. Cross-sectional areas of the thinner truss elements are 0.2, while for the thicker ones they are 1.0.

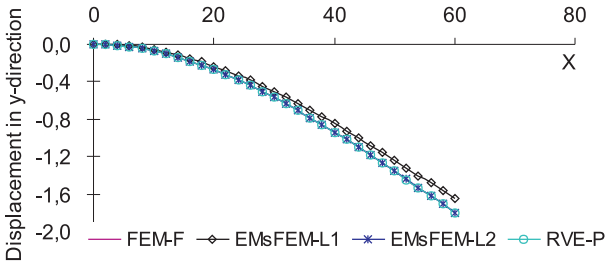

FIG. 11: *Y*-direction displacement of the points on the centroidal plane of cantilever beams.

tion method. It further illustrates that the instruction of coupled additional terms is more reasonable.

Example 3. In this example we investigate the unit cell with a hole in the center (see Fig. 12). The unit cell can be seen as a heterogeneous unit cell. The truss structure considered here is composed of $n_x \times n_y = 24 \times 8$ unit cells. The corresponding truss structure and coarse-scale mesh are shown in Fig. 13. The constraint and loading conditions are the same as example 1. Figure 14 illustrates the relative numerical results. The maximum relative error for the EMsFEM-L2 is 1.60% compared to the FEM-F, while for the EMsFEM-L1 it is 5.89%. The results obtained by the EMsFEM-L2 are fairly good and meet the accuracy requirement.

Example 4. For the truss structure considered in example 3, different loading and constraint conditions are applied in this example. As shown in Fig. 15, the left and right sides of the structure are fixed in the two axis directions, and a uniformly distributed load of 10,000 is applied on the top side. The results are shown in Fig. 16. Since the deformation within the unit cells is more complicated in this example than the previous ones, it can be seen that the structural stiffness values obtained by both the EMsFEM-L1 and EMsFEM-L2 are overestimated. On the other hand, by taking into account the periodic deformation in the boundary conditions, good results are achieved in the RVE-P.

From the four numerical examples given we can see that all the results obtained by EMsFEM-L2 are better than those of EMsFEM-L1, demonstrating that the construction method developed in this paper is more reason-

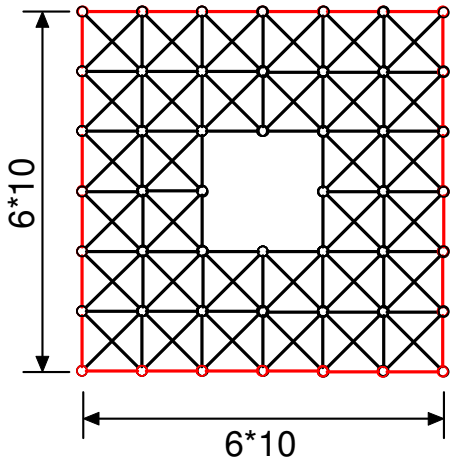

FIG. 12: Unit cell with a hole in the center. The outer element areas are 0.5 and internal element areas are 1.

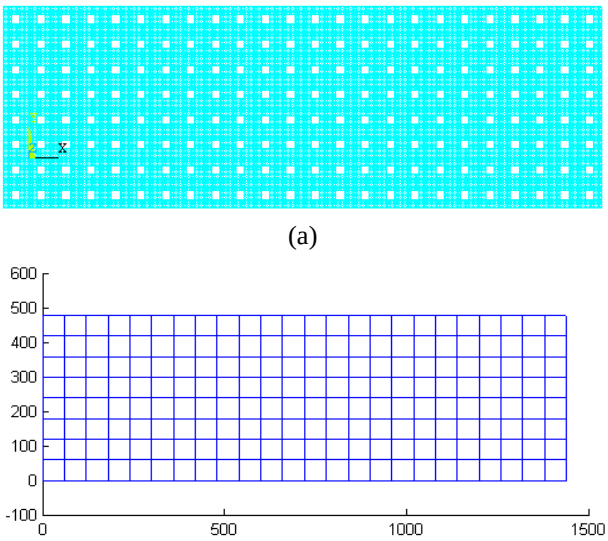

FIG. 13: The fine- and coarse-scale meshes of the truss structure.

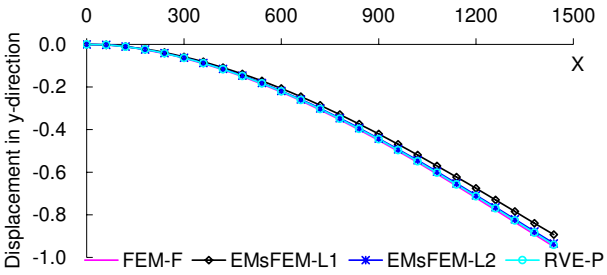

FIG. 14: Y-direction displacement of the points on the centroidal plane of cantilever beams.

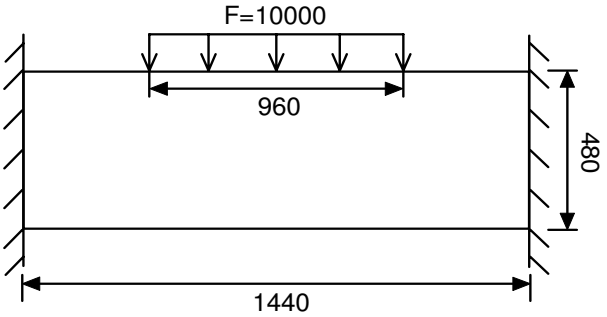

FIG. 15: The loading and constraint conditions.

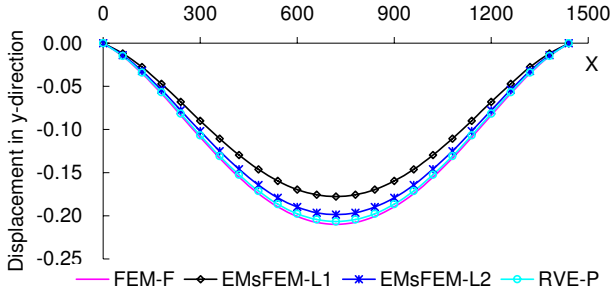

FIG. 16: *Y*-direction displacement of the points on the centroidal plane of the cantilever beam.

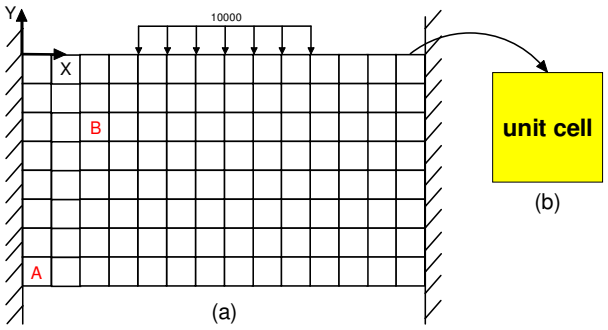

FIG. 17: Truss structure model: **(a)** truss structure and boundary conditions and **(b)** the unit cell.

able. Thus, in the rest of this article, we only use the new construction method and denote it as EMsFEM-L for simplicity. The source of error of the EMsFEM-L is analyzed in the next section, and then a special numerical technique is introduced to reduce the error.

5. SCALE EFFECT AND ERROR ANALYSIS

As shown in Figs. 9, 11, and 14, it is evident that the results obtained by the EMsFEM-L fit well with the reference results and the results of the RVE-P in the first three numerical examples. However, it is also observed that the stiffness of the structure can be overestimated by the EMsFEM-L under special constraints and loading conditions, such as the case in example 4. This is because the multiscale base functions in the EMsFEM-L are constructed with linear boundary conditions, which are dependent only on the boundary node coordinates and are independent of the stiffness distribution within the truss cell. That imposes a strong restriction for the boundary nodes and induces nonequilibrium nodal force on the boundary, especially for anisotropic truss cells. It is reasonable to believe that for a unit cell with more elementary cells, the boundary layers will have relative minor influences for the whole cell properties. So the error can be reduced by increasing the number of the elementary cells in the unit cell, as shown in the following example.

Example 5. The truss structure shown in Fig. 17 is composed of $n_x \times n_y = 24 \times 8$ unit cells. A uniformly distributed load of 10,000 is applied on the top side of the structure. To illustrate the scale effect, four kinds of unit cells are adopted, respectively, as shown in Fig. 18. Figure 18(a) shows a unit cell in which the cross-sectional areas of the truss elements are 0.2, except two thicker ones have areas of 1.0. The Young's modulus of all the truss elements in the unit cell is 1.0E6. The unit cell shown in

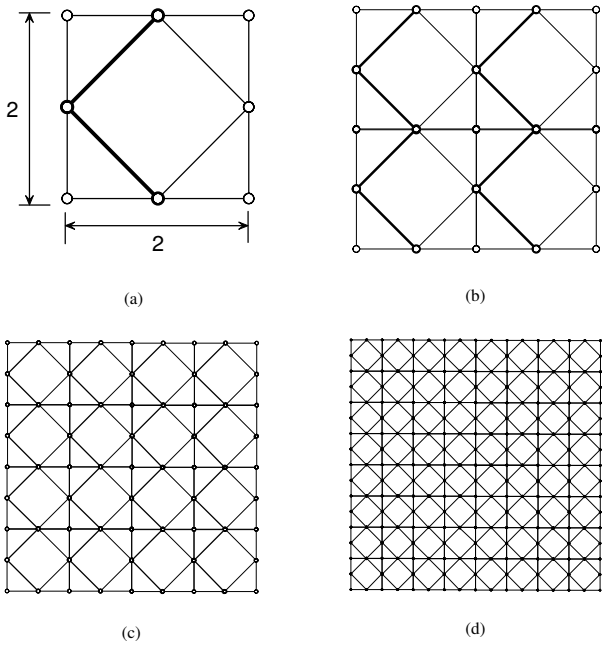

FIG. 18: Truss unit cell samples with different scale factors n: **(a)** the elementary cell with scale factor $n = 1$; **(b)**, **(c)**, and **(d)** unit cells composed of n^2 elementary cells, with $n = 2$, 4, and 8, respectively.

Fig. 18(a) is considered as an elementary cell. This cell structure is then repeated to form a series of unit cells with a scale factor n equal to 2, 4, and 8, respectively, as shown in Figs. 18(b)–(d). Also, in these figures we scale the elementary cell by the factor $1/n$, i.e., both the length and cross section of the truss elements in the elementary cell are scaled by the factor $1/n$. Thus, the size of the unit cell remains unchanged.

The displacements in the Y-direction on the top side of the structure with four different unit cells are shown in Figs. 19–22 in comparison with the reference solutions obtained by the FEM-F. It is obvious that the relative errors tend to decrease monotonically with the increasing scale factor n, as shown in Fig. 23.

For a strong heterogeneous unit cell, the nonequilibrium nodal forces, which is a key factor of errors in the EMsFEM-L, occur only at boundary nodes, and internal nodal forces are balanced automatically. It has been found in the RVE method with the Dirichlet-type boundary conditions (Yan et al., 2006; Pecullan et al., 1999; Huet, 1990; Hazanov and Huet, 1994; Ostoja-Starzewski, 1998; Kanit et al., 2003) that the influence of this nonequilibrium will become smaller and smaller with successively increasing scale factor. Based on this, it is easy to understand why the results obtained from the EMsFEM-L converge toward the reference solutions with increasing the scale factor n. This phenomenon can also be rechecked when the stiffness distribution within the unit cell tends to homogenous and the nonequilibrium nodal forces at boundary nodes will generally be decreased. For instance, if all the truss elements within the unit cell shown in Fig. 19 have the same cross-sectional area, then the displacements obtained in Y-direction on the top surface of the structure, as illustrated in Fig. 24, are of little differ-

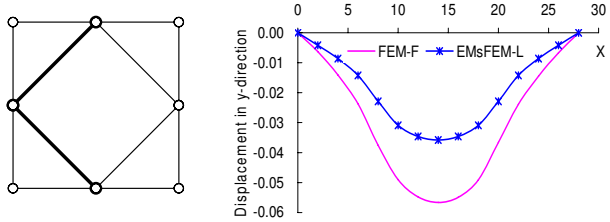

FIG. 19: Displacement in Y-direction on the top side of structure with scale factor $n = 1$. The maximum relative error is 36.75%.

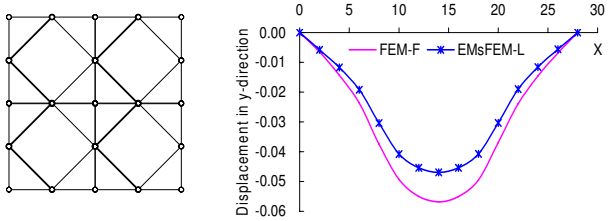

FIG. 20: Displacement in Y-direction on the top side of structure with scale factor $n = 2$. The maximum relative error is 17.43%.

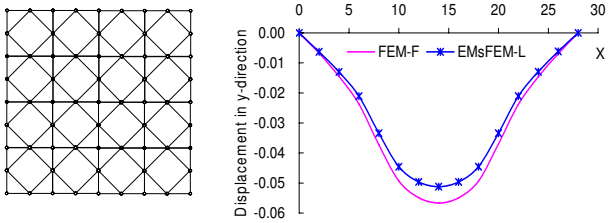

FIG. 21: Displacement in Y-direction on the top side of structure with scale factor $n = 4$. The maximum relative error is 9.70%.

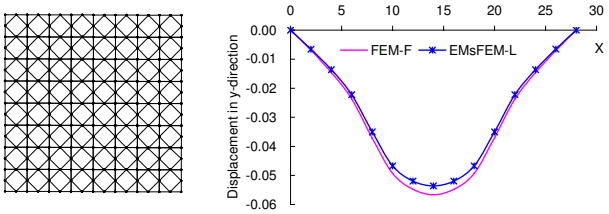

FIG. 22: Displacement in Y-direction on the top side of structure with scale factor $n = 8$. The maximum relative error is 5.30%.

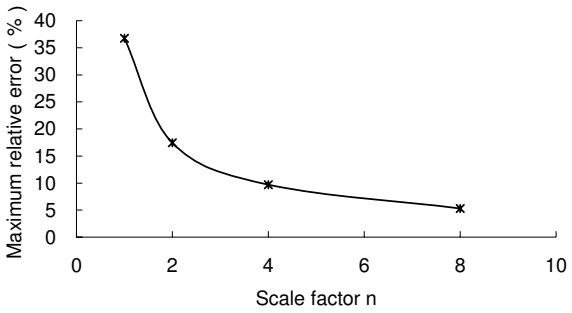

FIG. 23: Convergence of the maximum relative error with increasing scale factor n.

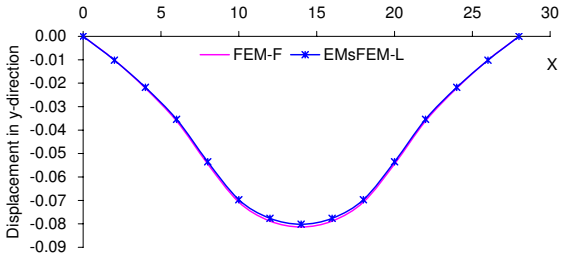

FIG. 24: Displacement in Y-direction on the top surface of structure with scale factor $n = 1$. The elements within the unit cell have the same cross-sectional areas 0.2.

ence in comparison with the results of the FEM-F. For the unit cell with only two nodes at each boundary, the nodal force equilibrium at cell boundaries is always satisfied and the errors are very small (see the results in example 2). To reduce the errors of the EMsFEM-L, in the following section an adaptive oversampling technique is adopted in the construction of the base functions.

6. THE OVERSAMPLING TECHNIQUE

6.1 Construction of Base Functions with the Oversampling Technique

From the above discussion we can see that the multiscale base functions constructed by linear boundary conditions impose too strong restrictions for the deformation of near boundary regions. Here the oversampling technique is adopted to generate more flexible oscillatory boundary conditions. The oversampling technique is proposed by Hou and Wu et al. (1997, 1999) for constructing more reliable base functions for the MsFEM. It uses the fine-scale solutions of a larger domain with specified boundary conditions to construct the base functions directly. By doing this, the influences of the boundary layers are greatly reduced in the constructed base functions. The numerical results (Hou and Wu et al., 1997, 1999) show that the oversampling technique does work well in the multiscale computations and provides an effective approach for removing the resonance effect between the mesh scale and the physical scale. In this section we inherit the basic idea of the oversampling technique and adopt it to construct the base functions for unit cells of periodic truss materials. Note that the adoptive oversampling technique here is different from the standard oversampling technique. In our method, we simply use the fine-scale solution of the oversampling region to form the boundary conditions for the base functions of the unit cells.

Consider a larger domain that covers the truss unit cell as illustrate in Fig. 25, in which $\Delta 1234$ is the unit cell (original element) and $\Delta 1'2'3'4'$ is the sampling element. Denote the temporary base functions for the original element as $\phi_i (i = 1, 2, 3, 4)$ and the temporary base functions for the sampling element as $\psi_{i'} (i' = 1, 2, 3, 4)$. Note that we utilize the oversampling technique only to obtain the oscillatory boundary conditions; the temporary base functions ψ and ϕ are constructed here without consideration of the coupled additional terms. First, temporary base functions ψ are constructed with the second method presented in Section 2.2. However, only $\psi_{i'x}$ and $\psi_{i'y}$ are used (i.e., the coupled additional terms $\psi_{i'xy}$ and $\psi_{i'yx}$ are not used in the next step). Then the temporary base functions ϕ are constructed from the linear combination of ψ as follows:

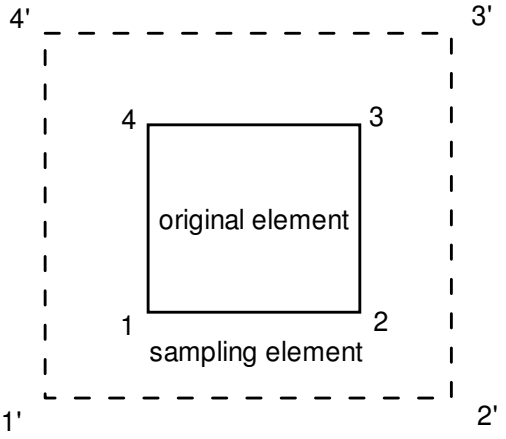

FIG. 25: Illustration of the oversampling technique.

$$\phi_i = \sum_{j=1}^{4} c_{ij} \psi'_j, (i = 1, 2, 3, 4) \tag{18}$$

where c_{ij} are the constants determined by the condition $\phi_i|_j = \delta_{ij}$ and δ is the Kronecker delta. Then we obtain the temporary base functions ϕ_{ix} and ϕ_{iy}, respectively. The values of ϕ_i at the unit cell's boundary are used as the oscillatory boundary conditions to construct the actual base functions $\mathbf{N}$ for the unit cell. In practice, the sampling domain should be large enough to avoid the influence of boundary layers. It is found that the final base functions, i.e., N_{ix}, N_{ixy}, N_{iy}, and N_{iyx} $(i = 1, 2, 3, 4)$ obtained by this way also satisfied Eq. (2). From the above analysis one can find that the oscillatory boundary conditions fully consider the heterogeneity of the unit cell's stiffness distribution. Thus, the nonequilibrium of the boundary nodal forces is reduced drastically. More accurate numerical results can be obtained with these base functions, as is seen in the next section. We denote the results obtained by the EMsFEM with the oscillatory boundary conditions as EMsFEM-O.

6.2 Modification of Stiffness Matrix

The equivalent stiffness matrix derived by the EMsFEM-O cannot satisfy rigid-body displacement completely. A numerical technique is applied to deal with this problem. In general, an element stiffness matrix $\mathbf{K}$ is symmetric and singular, i.e., it can be expressed as

$$\mathbf{K} = [\mathbf{X}]\,[\mathbf{\Lambda}]\,[\mathbf{X}]^{\mathbf{T}} \tag{19}$$

where $[\mathbf{X}]$ is the orthogonal matrix formed by the columns of eigenvectors of $\mathbf{K}$. For a 2D four-node element it can be written as

$$[\mathbf{X}] = \begin{bmatrix} \{X_1\} & \{X_2\} & \cdots & \{X_8\} \end{bmatrix} = \begin{bmatrix} X_{11} & X_{12} & \cdots & X_{18} \\ X_{12} & X_{22} & \cdots & X_{28} \\ \vdots & \vdots & \ddots & \vdots \\ X_{18} & X_{28} & \cdots & X_{88} \end{bmatrix} \tag{20}$$

and $[\mathbf{\Lambda}]$ is the diagonal matrix which is composed of the corresponding eigenvalues of $\mathbf{K}$ as follows:

$$[\Lambda] = \begin{bmatrix} \lambda_1 & & & \\ & \lambda_2 & & \\ & & \ddots & \\ & & & \lambda_8 \end{bmatrix} \tag{21}$$

assuming that $\lambda_1 > \lambda_2 > \cdots > \lambda_8$. In order to satisfy singularity (i.e., one element can have arbitrary rigid-body displacements), eigenvalues must have three zero values, i.e., $\lambda_6 = \lambda_7 = \lambda_8 = 0$. (Take a 2D plane element, for example; it contains two linear and one rotation displacements.) By observing the calculation results, we find that the eigenvalues of the equivalent stiffness matrix obtained by the EMsFEM-O have only two zero values, i.e., $\lambda_6 \neq 0$. Further investigation shows that the situation occurs because the rotation displacement cannot satisfy rigid-body displacement. The stiffness matrix $\mathbf{K}$ should be modified.

Ye et al. (2009) developed two methods to modify the stiffness matrix. They are the eigenvalues modified method (EMM) and the eigenvalues and eigenvectors modified method (EEMM). Numerical experiments show that application of the EMM and EEMM gives similar results for the situations considered here, so we chose the more convenient EMM to modify our stiffness matrix. In EMM, the nonzero eigenvalue λ_6 is set to zero with other eigenvalues and the eigenvector matrix $[\mathbf{X}]$ remains unchanged. Then the modified stiffness matrix can be expressed as

$$\mathbf{K}' = [\mathbf{X}]\,[\mathbf{\Lambda}']\,[\mathbf{X}]^{\mathbf{T}} \tag{22}$$

where $[\mathbf{\Lambda}']$ is the revised eigenvalue matrix in which λ_6 equals 0.

For the numerical example shown in Fig. 21, we solve it again with the EMsFEM-O and compare it with previous results. It is obvious that the results obtained by the EMsFEM-O fit fairly well with the FEM-F as shown in Fig. 26. Figure 27 shows the new numerical results of example 4. Improved accuracy is obtained by the EMsFEM-O in comparison with the EMsFEM-L. The results are shown in Fig. 28 for a homogeneous unit cell, i.e., the numerical example shown in Fig. 9. It shows that the results obtained by the EMsFEM-O and the EMsFEM-L are almost the same. Under this condition, the oscillatory boundaries obtained by the oversampling technique are almost linear and coincide with those of the EMsFEM-L.

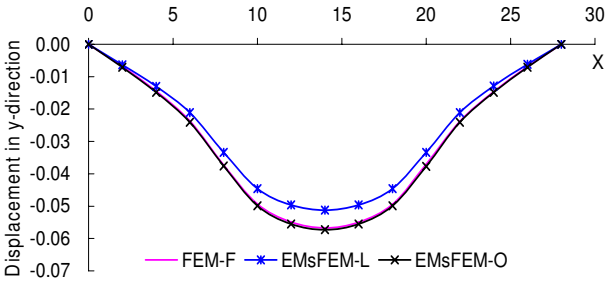

FIG. 26: Comparison between the EMsFEM-O and other methods shown in Fig. 21.

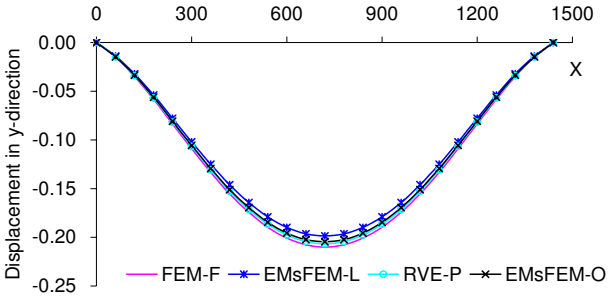

FIG. 27: Comparison between the EMsFEM-O and other methods shown in Fig. 16.

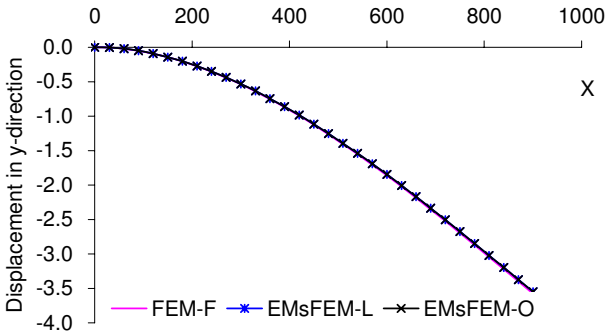

FIG. 28: Comparison between the EMsFEM-O and other methods shown in Fig. 9.

7. DOWNSCALING COMPUTATION

Different from the general homogenization methods, the EMsFEM constructs base functions to form the equivalent stiffness matrix of unit cells. These base functions reflect local fluctuations within unit cells and in return, can be used to construct the fine-scale solutions. Therefore, the EMsFEM is able to perform the downscaling computations. That is to say, the displacement solutions for the fine-scale structures can be obtained through macroscopic results and then the stress and strain solutions in the unit cells are obtained. These results are important and can be used for further investigations, i.e., for the nonlinear situations.

(a) As for the EMsFEM-L, the base functions are constructed with linear boundary conditions and the downscaling computations can be carried out directly. The internal force of the ith truss element within the unit cell can be written as

$$\overline{F}_i^e = k_e^i \Delta l_i \tag{23}$$

Using Eq. (11), we get

$$\overline{F}_i^e = \frac{E_i A_i}{l_i} \left[\mathbf{G^e}\right]_i \{\mathbf{u'_E}\} \tag{24}$$

where $\{\mathbf{u'_E}\}$ are the macroscopic results obtained by the EMsFEM-L.

Take unit cell A and unit cell B shown in Fig. 8(b), for example. The internal forces of truss elements in the unit cells are computed by both the EMsFEM-L and the FEM-F. The results are shown in Figs. 29 and 30, respectively. Note that a positive value implies tension and a negative value implies compression. It shows that the internal forces obtained by the EMsFEM-L fit well with those of the FEM-F in general.

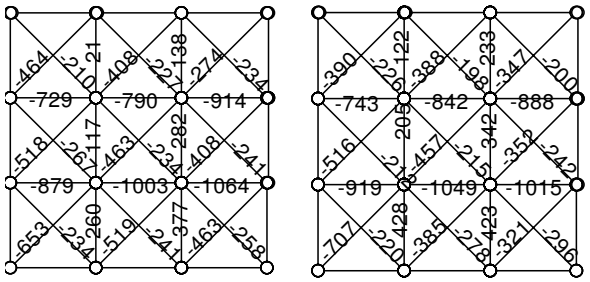

(a) EMsFEM-L (b) FEM-F

FIG. 29: Internal forces of truss elements of unit cell A.

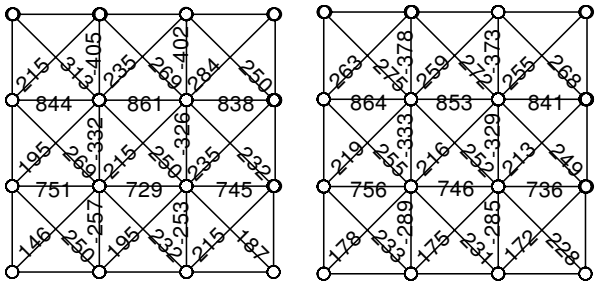

(a) EMsFEM-L (b) FEM-F

FIG. 30: Internal forces of truss elements of unit cell B.

(b) As for the EMsFEM-O, the base functions are constructed with oscillatory boundary conditions which are obtained by the oversampling technique. As the equivalent stiffness matrix has been modified, we assume that the modified stiffness matrix and the original one have the following relationship:

$$\mathbf{K'} = \mathbf{SKS^T} \tag{25}$$

where $\mathbf{S}$ is a 8×8 matrix and can be obtained by solving 64 nonlinear equations iteratively. Also for periodic materials, the matrix $\mathbf{S}$ needs to be solved only one time.

By taking into account Eq. (25), Eq. (14) yields

$$\pi'_E = \sum_{i=1}^{M} \pi_e^{i\prime} = \frac{1}{2} \mathbf{u'^T_E} \left[\sum_{i=1}^{M} \mathbf{S} \mathbf{G^{eiT}} k_e^i \mathbf{G^{ei}} \mathbf{S^T} \right] \mathbf{u'_E} \tag{26}$$

If we denote $\mathbf{G^{e\prime}} = \mathbf{G^e S^T}$, we get

$$\pi'_E = \sum_{i=1}^{M} \pi_e^{i\prime} = \frac{1}{2} \mathbf{u'^T_E} \left[\sum_{i=1}^{M} \mathbf{G^{ei\prime T}} k_e^i \mathbf{G^{ei\prime}} \right] \mathbf{u'_E} \tag{27}$$

By comparing Eq. (27) with Eq. (14), we can find that the mapping relations between internal nodes and corner nodes have been changed. The new mapping relations are used to calculate the internal forces of truss elements within unit cells.

Here we take unit cell A and unit cell B shown in Fig. 17 as examples and consider the unit cell shown in Fig. 18(c). The results obtained by the EMsFEM-O and the FEM-F are shown in Figs. 31 and 32.

For the numerical results presented above, one can find that: (1) relatively small relative errors are generated for the truss elements whose internal forces are relatively large; and (2) relatively large relative error is generated

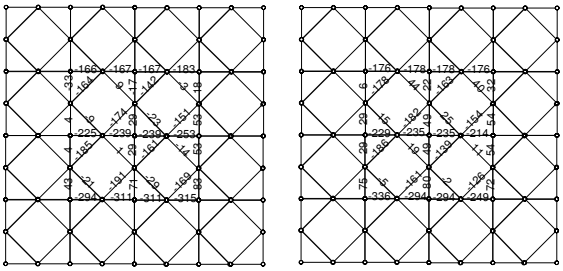

(a) EMsFEM-O (b) FEM-F

FIG. 31: Internal forces of truss elements of unit cell A.

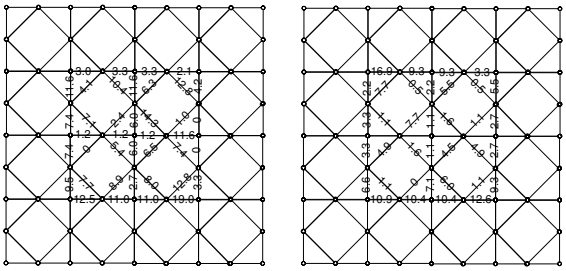

(a) Error of unit cell A (b) Error of unit cell B

FIG. 33: The errors of internal forces of truss elements (%).

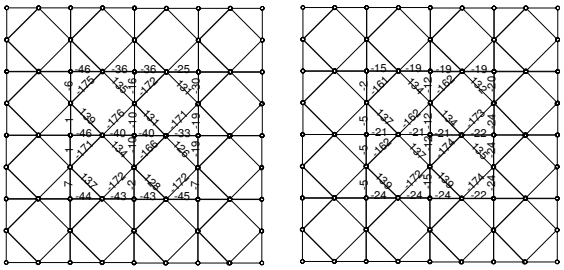

(a) EMsFEM-O (b) FEM-F

FIG. 32: Internal forces of truss elements of unit cell B.

for the truss elements with small internal forces. It is obvious that the truss elements having large internal forces play an important role for the performance of the truss structure, while those having small internal forces make small contributions. So the errors induced by relatively small internal forces can be ignored in strength analysis. If the error formula (28) is used, the error distributions corresponding to Figs. 31 and 32 are shown in Fig. 33. The results show that the errors of the internal forces in most of the elements are less than 10%:

$$Err_i = \frac{|F_{fi} - F_{Mi}|}{|F_{\max}|} \tag{28}$$

where F_{fi} is the internal force of the ith truss element obtained by the FEM-F, F_{Mi} is the internal force of the ith truss element obtained by the EMsFEM, and $|F_{\max}|$ is the absolute value of maximal internal force of all truss elements within the unit cell.

8. CONCLUSIONS

An extended multiscale finite element method is developed for solving the problems of periodic lattice truss materials. Multiscale base functions are constructed numerically for unit cells of different types to form the equivalent stiffness matrices. In order to deal with the coupled effects among different directions in the multidimensional problems, the coupled additional terms are introduced in the multiscale base functions. The base functions are constructed with both the linear and oscillatory boundary conditions. The oversampling technique is introduced in the generation of the oscillatory boundary conditions. It shows that for heterogeneous unit cells, the use of base functions constructed with the oscillatory boundary conditions generates more accurate numerical results in comparison with that of linear ones, for it can reduce the nonequilibrium nodal forces of the boundary nodes. Numerical experiments are carried out to examine the accuracy of the newly developed method, showing that for the numerical examples presented in this paper the numerical results obtained by the EMsFEM fit fairly well with the reference solutions. At the same time the developed method reduces the computational cost and memory storage drastically.

The EMsFEM can be used to perform downscaling computations which are superior to other homogenization methods. The actual stress and strain information in microscopic level can be obtained easily, which is important in engineering applications, especially for the nonlinear cases. Meanwhile, in our method the construction of base functions and downscaling computations are performed in each unit cell independently, that is to say, the method developed here can be extended for parallel computing in a simple way and has great potential in mechanical analysis of nonperiodic continuum problems.

ACKNOWLEDGEMENTS

Support from the National Natural Science Foundation (10721062, 11072051, 90715037, 10728205,

51021140004), the 111 Project (no. B08014), the Program for Changjiang Scholars and Innovative Research Team in University (PCSIRT), and the National Key Basic Research Special Foundation of China (2010CB832704) is gratefully acknowledged.

REFERENCES

Aarnes, J. E., On the use of a mixed multiscale finite element method for greater flexibility and increased speed or improved accuracy in reservoir simulation, *Multiscale Modeling Simulation*, vol. **2**, pp. 421–439, 2004.

Aarnes, J. E., Krogstad, S., and Lie, K. A., A hierarchical multiscale method for two-phase flow based upon mixed finite elements and nonuniform coarse grids, *Multiscale Modeling Simulation*, vol. **2**, pp. 421–439, 2006.

Benssousan, A., Lions, J. L., and Papanicoulau, G., Asymptotic analysis for periodic structures, Amsterdam, North Holland, 1978.

Brittain, S. T., Sugimura, Y., Schueller, O. J. A., Evans, A. G., and Whitesides, G. M., Fabrication and mechanical performance of a mesoscale space-filling truss system, *Microelectromechanical Syst*., vol. **10**, pp. 113–20, 2001.

Chen, Z. and Hou, T. Y., A mixed multiscale finite element method for elliptic problems with oscillating coefficients, *Math. Comput.*, vol. **72**, pp. 541–576, 2003.

Chu, J., Efendiev, Y., Ginting, V., and Hou, T. Y., Flow based oversampling technique for multiscale finite element methods, *Adv. Water Resources*, vol. **31**, pp. 599–608, 2008.

Deshpande, V. S., Fleck, N. A., and Ashby, M. F., Effective properties of the octet-truss lattice material, *J. Mech. Phys. Solids*, vol. **49**, pp. 1747–1769, 2001.

Dostert, P., Efendiev, Y., and Hou, T. Y., Multiscale finite element methods for stochastic porous media flow equations and application to uncertainty quantification, *Comput. Methods Appl. Mech. Eng*., vol. **197**, pp. 3445–3455, 2008.

Efendiev, Y., Ginting, V., Hou, T. Y., and Ewing, R., Accurate multiscale finite element methods for two-phase flow simulations, *J. Comput. Phys.*, vol. **220**, pp. 155–74, 2006.

Efendiev, Y. and Hou, T. Y., Multiscale finite element methods for porous media flows and their applications, *Appl. Numer. Math.*, vol. **57**, pp. 577–96, 2007.

Evans, A. G., Hutchinson, J. W., Ashby, M. F., and Wadley, H. N. G., The topological design of multifunctional cellular metals, *Prog. Mater. Sci*., vol. **46**, pp. 311–327, 2001.

Fish, J., Shek, K., Pundheeradi, M., and Shephard, M. S., Computational plasticity for composite structures based on mathematical homogenization: Theory and practice, *Comput. Meth. Appl. Mech. Eng.*, vol. **148**, pp. 53–73, 1997.

Hassani, B. and Hinton, E., A review of homogenization and topology optimization, I. Homogenization theory for media with periodic structure, *Comput. Struct.*, vol. **69**, pp. 707–717, 1998.

Hazanov, S. and Huet, C., Order relationships for boundary conditions effect in heterogeneous bodies smaller than representative volume, *J. Mech. Phys. Solids*, vol. **42**, pp. 1995–2011, 1994.

He, X. and Ren, L., Finite volume multiscale finite element method for solving the groundwater flow problems in heterogeneous porous media, *Water Resources Res*., vol. **41**, W10417 doi:10.1029/2004WR003934, 2005.

Hou, A. and Gramoll, K., Compressive strength of composite lattice structures, *J. Reinforced Plastics Compos*., vol. **17**, pp. 462–483, 1998.

Hou, T. Y. and Wu, X. H., A multiscale finite element method for elliptic problems in composite materials and porous media, *J. Comput. Phys.*, vol. **134**, pp. 169–89, 1997.

Hou, T. Y., Wu, X. H., and Cai, Z. Q., Convergence of a multiscale finite element method for elliptic problems with rapidly oscillating coefficients, *Math. Comput.*, vol. **68**, pp. 913–943, 1999.

Hou, T. Y., Multiscale modelling and computation of fluid flow, *Int. J. Numer. Methods Fluids*, vol. **47**, pp. 707–719, 2005.

Huet, C., Application of variational concepts to size effects in elastic heterogeneous bodies, *J. Mech. Phys. Solids*, vol. **38**, pp. 813–841, 1990.

Huybrechts, S. M., Meink, T. E., Wegener, P. M., and Ganley, J. M., Manufacturing theory for advanced grid stiffened structures, *Compos. Part A: Appl. Sci. Manuf*., vol. **33**, pp. 155–161, 2002.

Jenny, P., Lee, S. H., and Tchelepi, H. A., Multi-scale finite volume method for elliptic problems in subsurface flow simulation, *J. Comput. Phys.*, vol. **187**, pp. 47–67, 2003.

Kanit, T., Forest, S., Galliet, I., Mounoury, V., and Jeulin, D., Determination of the size of the representative volume element for random composites: Statistical and numerical approach, *Int. J. Solids Struct.*, vol. **40**, pp. 3647–3679, 2003.

Kouznetsova, V., *Computational Homogenization for the Multi-Scale Analysis of Multi-Phase Materials*, PhD Thesis, Technical University of Eindhoven, Eindhoven, 2002.

Noor, A. K., Continuum modeling for repetitive lattice structures, *Appl. Mech. Rev*., vol. **41**, pp. 285–296, 1988.

Ostoja-Starzewski, M., Random field models of heterogeneous materials, *Int. J. Solids Struct.*, vol. **35**, pp. 2429–2455, 1998.

Pecullan, S., Gibiansky, L. V., and Torquato, S., Scale effects on the elastic behavior of periodic and hierarchical two-dimensional composites, *J. Mech. Phys. Solids*, vol. **47**, pp. 1509–1542, 1999.

Terada, K., Hori, M., Kyoya, T., and Kikuchi, N., Simulation of

the multi-scale convergence in computational homogenization approach, *Int. J. Solids Struct.*, vol. **37**, pp. 2285–2311, 2000.

Wadley, H. N. G., Multifunctional periodic cellular metals, *Philos. Trans. Royal Soc. London Series A*, vol. **364**, pp. 31–68, 2006.

Yan, J., Cheng, G. D., Liu, S. T., and Liu, L., Comparison of prediction on effective elastic property and shape optimization of truss material with periodic microstructure, *Int. J. Mech. Sci.*, vol. **48**, pp. 400–413, 2006.

Ye, H. F., Wang, J. B., and Zhang, H. W., Numerical algorithms for prediction of mechanical properties of single-walled carbon nanotubes based on molecular mechanics model, *Comput. Mater. Sci*., vol. **44**, pp. 1089–1097, 2009.

Yu, Q. and Fish, J., Multiscale asymptotic homogenization for multiphysics problem with multiple spatial and temporal scales: A coupled thermo-viscoelastic example problem, *Int. J. Solids Struct.*, vol. **39**, pp. 6429–6452, 2002.

Zhang, H. W., Fu, Z. D., and Wu, J. K., Coupling multiscale finite element method for consolidation analysis of heterogeneous saturated porous media, *Adv. Water Resources*, vol. **32**, pp. 268–279, 2009.

Journal for Multiscale Computational Engineering 8(6), 615–629 (2010)

ON THE CANONICAL STRUCTURE OF THE EIGENDEFORMATION-BASED REDUCED-ORDER HOMOGENIZATION

Wei Wu,[1] Zheng Yuan,[1] Jacob Fish,[1,] & Venkat Aitharaju[2]*

[1]*Multiscale Science and Engineering Center, Department of Mechanical, Aerospace, & Nuclear Engineering, Rensselaer Polytechnic Institute, Troy, NY, USA*

[2]*Senior Manufacturing Project Engineer, 2000 Centerpoint Parkway, Pontiac, MI 48341, USA*

[*]Address all correspondence to Jacob Fish E-mail: fishj@rpi.edu

The manuscript focuses on the computational aspects of the eigendeformation-based, reduced-order homogenization developed in Fish and Yuan (2008), Oskay and Fish (2007), and Yuan and Fish (2009) with regard to its compatibility to commercial finite element code architecture and on standard user-defined material interfaces. Most commercial finite element software codes provide functionality for adding user-defined material models. The eigendeformation-based homogenization formulation has a lot of specificity that limits its flexibility to add user-defined material models. In the present manuscript we recast the original formulation referred to above into a more transparent and flexible form that enables easy addition of new material models of microconstituents. Several nonlinear examples, including damage, plasticity, and viscoplasticity, are used to demonstrate the canonical structure of the proposed formulation and its verification against the direct computational homogenization method.

KEY WORDS: *reduced order homogenization, composite material design system, material inelasticities*

1. INTRODUCTION

Due to their light weight, high specific strength/stiffness, and resistance to corrosion, composite materials have been increasingly attracting attention since the middle of the last century, yet the supporting modeling techniques are by and large limited to various effective medium models, such the Mori-Tanaka (1973) and self-consistent (Hill, 1965) approaches. Most finite element commercial software packages for composites house simplistic effective medium-like models, which tend to oversimplify the microstructural details and thus limit their full potential. On the other hand, in the academic community, computational homogenization methods that explicitly account for complex material microstructure have been widely used for both linear (Guedes and Kikuchi, 1990) and nonlinear (Terada and Kikuchi, 1995; Fish et al., 1997; Yu et al., 1999; Fish and Yu, 2001) problems. Despite this progress, a cost-effective and flexible multiscale methodology that can be seamlessly integrated into commercial finite element codes does not exist.

Adoption of computational homogenization methods in commercial finite element packages has been very slow, primarily due to their cumbersome code architecture that requires nested structure (Yuan and Fish, 2008). Furthermore, while the computational cost of the computational homogenization approaches is a small fraction compared to the direct numerical simulation, where a characteristic mesh size is of the heterogeneity order, they remain computationally prohibitive for complex microstructures. This is because a nonlinear unit cell problem for a two-scale problem has to be solved for a number of times equal to the product of number of quadrature points at a macroscale and the number of load increments and iterations at the macroscale.

The primary objective of the present manuscript is to integrate a computationally efficient method, such as the reduced-order homogenization method (Fish and Yuan, 2008; Oskay and Fish, 2007; and Yuan and Fish, 2009), in a conventional finite element code architecture. The reduced-order homogenization approach (Fish and Yuan, 2008; Oskay and Fish, 2007; and Yuan and Fish, 2009)

1543–1649/10/$35.00

constructs a unit cell problem in terms of eigendeformation modes, which a priori satisfy equilibrium equations at the microscale and therefore eliminate the need for costly solution of discretized nonlinear equilibrium. The challenge is to reformulate the reduced-order homogenization in terms of the conventional single-scale building blocks for each micro phase and micro interface, such as a stress update and consistent tangent operator. In the proposed canonical structure, the user is required to supply only a conventional stress update and consistent tangent routines for each micro phase and micro interface, from which the backend programs of the reduced-order homogenization formulation construct the overall stress update and the overall consistent tangent operator. Finally, we demonstrate a seamless integration of the reduced-order homogenization approach in a commercial finite element code by providing a sample of the user-defined material model that employs the same structure as the UMAT in ABAQUS.

This paper is organized as follows. Section 2 gives a brief introduction to eigendeformation-based homogenization. Section 3 describes the canonical framework starting from the formulation of the unit cell problem, followed by the consistent tangent, the user-defined material model, and the nested Newton method for solving the two-scale problem. In Section 4, several nonlinear examples, including, damage, plasticity, and viscoplasticity, are used to demonstrate the canonical structure of the method and its verification against the direct computational homogenization method.

2. REVIEW OF REDUCED-ORDER HOMOGENIZATION

2.1 Mathematical Homogenization

Following Yuan and Fish (2009), the strong form of the boundary value problem is stated at the microscale:

$$\sigma^{\zeta}_{ij,j}(\mathbf{x}) + b^{\zeta}_i(\mathbf{x}) = 0 \quad \mathbf{x} \in \Omega, \tag{1}$$

$$\sigma^{\zeta}_{ij}(\mathbf{x}) = L^{\zeta}_{ijkl}(\mathbf{x})\left[\varepsilon^{\zeta}_{kl}(\mathbf{x}) - \sum_I {}^I\mu^{\zeta}_{kl}(\mathbf{x})\right] \quad \mathbf{x} \in \Omega, \tag{2}$$

$$\varepsilon^{\zeta}_{ij}(\mathbf{x}) = u^{\zeta}_{(i,j)}(\mathbf{x}) \equiv \frac{1}{2}\left(u^{\zeta}_{i,j} + u^{\zeta}_{j,i}\right) \quad \mathbf{x} \in \Omega, \tag{3}$$

$$u^{\zeta}_i(\mathbf{x}) = \bar{u}_i(\mathbf{x}) \quad \mathbf{x} \in \Gamma_u, \tag{4}$$

$$\sigma^{\zeta}_{ij}(\mathbf{x})n_j(\mathbf{x}) = \bar{t}_i(\mathbf{x}) \quad \mathbf{x} \in \Gamma_t, \tag{5}$$

$$\delta^{\zeta}_i(\mathbf{x}) \equiv \left\langle u^{\zeta}_i(\mathbf{x}) \right\rangle = u^{\zeta}_i\Big|_{S^{\zeta}_-} - u^{\zeta}_i\Big|_{S^{\zeta}_+} \quad \mathbf{x} \in S^{\zeta}, \tag{6}$$

$$\sigma^{\zeta}_{ij}n_j\Big|_{S^{\zeta}_+} + \sigma^{\zeta}_{ij}n_j\Big|_{S^{\zeta}_-} = t^{\zeta}_i\Big|_{S^{\zeta}_+} + t^{\zeta}_i\Big|_{S^{\zeta}_-} = 0, \tag{7}$$

where the superscript ζ denotes dependence of the response fields on the microstructural heterogeneities. Equation (2) describes the constitutive relation which assumes an additive decomposition of total strain ε^{ζ}_{kl} into elastic and inelastic components, more generally referred to as eigenstrains ${}^I\mu^{\zeta}_{kl}$, where the left superscript I stands for various eigenstrain types, such as inelastic deformation, thermal change, moisture effects, etc. Equations (5)–(7) govern the traction continuity along the interface of microconstituents denoted by S^{ζ}; the $+/-$ signs indicate the two sides of the interface. δ^{ζ}_i is the displacement jump (or so-called eigenseparation) along the interface and $\langle\bullet\rangle$ is the jump operator.

Various fields are assumed to depend on the macroscopic coordinate $\mathbf{x}$ and microscopic coordinate $\mathbf{y} = \mathbf{x}/\zeta$. They are expressed in terms of the two-scale asymptotic expansion as

$$\begin{aligned}
&u_i(\mathbf{x},\mathbf{y}) = u^0_i(\mathbf{x}) + \zeta u^1_i(\mathbf{x},\mathbf{y}) + \cdots,\\
&\varepsilon_{ij}(\mathbf{x},\mathbf{y}) = \varepsilon^0_{ij}(\mathbf{x},\mathbf{y}) + \zeta\varepsilon^1_{ij}(\mathbf{x},\mathbf{y}) + \cdots.\\
&\sigma_{ij}(\mathbf{x},\mathbf{y}) = \sigma^0_{ij}(\mathbf{x},\mathbf{y}) + \zeta\sigma^1_{ij}(\mathbf{x},\mathbf{y}) + \cdots,\\
&{}^I\mu_{ij}(\mathbf{x},\mathbf{y}) = {}^I\mu^0_{ij}(\mathbf{x},\mathbf{y}) + \zeta{}^I\mu^1_{ij}(\mathbf{x},\mathbf{y}) + \cdots,
\end{aligned} \tag{8}$$

Inserting the asymptotic expansions into the governing Eqs. (1)–(7) yields the microscale unit cell problem

$$\left\{L_{ijkl}(\mathbf{y})\left[\bar{\varepsilon}_{kl}(\mathbf{x}) + u^1_{k,y_l}(\mathbf{x},\mathbf{y}) - \sum_I {}^I\mu^0_{kl}(\mathbf{x},\mathbf{y})\right]\right\}_{,y_j} = 0 \tag{9}$$

from which the macroscopic stress can be computed by

$$\bar{\sigma}_{ij,j}(\mathbf{x}) = \frac{1}{\Theta}\int_{\Theta} L_{ijkl}(\mathbf{y})\Big(\bar{\varepsilon}_{kl}(\mathbf{x}) + u^1_{k,y_l}(\mathbf{x},\mathbf{y}) - \sum_I {}^I\mu^0_{kl}(\mathbf{x},\mathbf{y})\Big)d\mathbf{y} \tag{10}$$

where Θ is the unit cell domain, and $\bar{\sigma}_{ij}$ and $\bar{\varepsilon}_{ij}$ are the macroscale stress and strain, respectively.

2.2 Reduced-Order Two-Scale Formulation

The salient feature of the eigendeformation-based homogenization is that the microscale displacement field $u^1_i(\mathbf{x},\mathbf{y})$ is constructed so that the stress field in the unit cell automatically satisfies the equilibrium equations for arbitrary eigenstrains ${}^I\mu^0_{ij}$ and eigenseparations $\delta_{\hat{n}}$:

$$u_i^1(\mathbf{x},\mathbf{y}) = u_i^{el}(\mathbf{x},\mathbf{y}) + \sum_I {}^I u_i^{\mu}(\mathbf{x},\mathbf{y}) + u_i^{\delta}(\mathbf{x},\mathbf{y})$$
$$= H_{ikl}^{mic}\bar{\varepsilon}_{kl}(\mathbf{x}) + \sum_I \int_\Theta {}^I h_{ikl}^{mic\text{-}\mu}(\mathbf{y},\hat{\mathbf{y}})\,{}^I\mu_{kl}^0(\mathbf{x},\hat{\mathbf{y}})d\hat{\mathbf{y}} \quad (11)$$
$$+ \int_S h_{i\hat{n}}^{mic\text{-}\delta}(\mathbf{y},\hat{\mathbf{y}})\delta_{\hat{n}}(\mathbf{x},\hat{\mathbf{y}})d\hat{\mathbf{y}}$$

The resulting microscale displacement gradients are given by

$$u_{i,y_j}^1(\mathbf{x},\mathbf{y}) = G_{ijkl}^{mic}\bar{\varepsilon}_{kl}(\mathbf{x}) + \sum_I \int_\Theta {}^I g_{ijkl}^{mic\text{-}\mu}(\mathbf{y},\hat{\mathbf{y}})$$
$$\times\, {}^I\mu_{kl}^0(\mathbf{x},\hat{\mathbf{y}})d\hat{\mathbf{y}} + \int_S g_{ij\hat{n}}^{mic\text{-}\delta}(\mathbf{y},\hat{\mathbf{y}})\delta_{\hat{n}}(\mathbf{x},\hat{\mathbf{y}})d\hat{\mathbf{y}} \quad (12)$$

where G_{ijkl}^{mic}, ${}^I g_{ijkl}^{mic\text{-}\mu}$, and $g_{ij\hat{n}}^{mic\text{-}\delta}$ are influence functions for macroscale strain, eigenstrain, and eigenseparation, respectively, which can be computed by solving a sequence of elastic boundary value problems prior to nonlinear macroanalysis. The reduced-order model is obtained by discretizing the eigenstrain and eigenseparation fields as

$${}^I\mu_{ij}^0(\mathbf{x},\mathbf{y}) = \sum_{\alpha=1}^{n_I} {}^I N^{(\alpha)}(\mathbf{y})\,{}^I\bar{\mu}_{ij}^{(\alpha)}(\mathbf{x})$$
$$\delta_{\hat{n}}(\mathbf{x},\tilde{\mathbf{y}}) = \sum_{\xi=1}^{m} N^{(\xi)}(\tilde{\mathbf{y}})\bar{\delta}_{\hat{n}}^{(\xi)}(\mathbf{x}) \quad (13)$$

where n_I and m are the number of partitions of phases and interfaces, respectively, and ${}^I\bar{\mu}_{ij}^{(\alpha)}$ and $\bar{\delta}_{\hat{n}}^{(\xi)}$ are the average eigenstrain and eigenseparation in the phase partition α and the interface partition ξ, respectively. $N^{(\alpha)}(\mathbf{y})$ is a piecewise constant shape function defined as

$$N^{(\alpha)}(\mathbf{y}) = \begin{cases} 1 & \mathbf{y} \in \Theta^{(\alpha)} \\ 0 & \mathbf{y} \notin \Theta^{(\alpha)} \end{cases} \quad (14)$$

whereas $N^{(\xi)}(\tilde{\mathbf{y}})$ is a linear combination of piecewise linear finite element shape functions defined over the surface partition ξ.

Combining the governing equations for the unit cell problem (9) with the decomposition (12) and the discretization (13) yields the reduced-order system of equations:

Reduced-order microscale unit cell problem:

$$\begin{aligned} &\varepsilon_{ij}^{(\beta)}(\mathbf{x}) - \sum_{I=1}^{N}\sum_{\alpha=1}^{n_I} {}^I P_{ijkl}^{(\beta\alpha)}\,{}^I\bar{\mu}_{kl}^{(\alpha)}(\mathbf{x}) \\ &- \sum_{\xi=1}^{m} Q_{ij\hat{n}}^{(\beta\xi)}\bar{\delta}_{\hat{n}}^{(\xi)}(\mathbf{x}) = A_{ijkl}^{(\beta)}\bar{\varepsilon}_{kl}(\mathbf{x}) \\ &- \sum_{I=1}^{N}\sum_{\alpha=1}^{n_I} {}^I C_{\hat{n}kl}^{(\eta\alpha)}\,{}^I\bar{\mu}_{kl}^{(\alpha)}(\mathbf{x}) + t_{\hat{n}}^{(\eta)}(\mathbf{x}) \\ &- \sum_{\xi=1}^{m} D_{\hat{n}\hat{n}}^{(\eta\xi)}\bar{\delta}_{\hat{n}}^{(\xi)}(\mathbf{x}) = B_{\hat{n}kl}^{(\eta)}\bar{\varepsilon}_{kl}(\mathbf{x}) \end{aligned} \quad (15)$$

Reduced-order macroscale stress update:

$$\bar{\sigma}_{ij}(\mathbf{x}) = \bar{L}_{ijkl}\bar{\varepsilon}_{kl}(\mathbf{x}) + \sum_{I=1}^{N}\sum_{\alpha=1}^{n_I} {}^I\bar{E}_{ijkl}^{(\alpha)}\,{}^I\bar{\mu}_{kl}^{(\alpha)}(\mathbf{x})$$
$$+ \sum_{\xi=1}^{m} \bar{F}_{ij\hat{n}}^{(\xi)}\bar{\delta}_{\hat{n}}^{(\xi)}(\mathbf{x}) \quad (16)$$

where $t_{\hat{n}} = G(\bar{\delta}_{\hat{n}})$ represents the traction along interface. All the coefficient tensors in the reduced-order system, such as ${}^I P_{ijkl}$, $Q_{ij\hat{n}}$, A_{ijkl}, ${}^I C_{\hat{n}ij}$, $D_{\hat{n}\hat{m}}$, $B_{\hat{n}ij}$, $\overline{L}_{ijkl}$, ${}^I\overline{E}_{ijkl}$, and $\overline{F}_{ij\hat{n}}$, are determined in the preprocessing stage prior to nonlinear macroanalysis. A detailed formulation can be found in Fish and Yuan (2008), and Yuan and Fish (2009).

3. THE CANONICAL STRUCTURE

In the present manuscript we focus on the computational aspects of the eigendeformation-based reduced-order homogenization, its compatibility to the commercial finite element software, and on a standard user-defined material interface. Most conventional finite element software packages provide functionality to add a user-defined material model. The eigendeformation formulation outlined in the previous section has a nonconventional data structure that complicates the task of adding user-defined material models. In this section we recast the original formulation (Fish and Yuan, 2008; and Yuan and Fish, 2009) into a form that provides a conventional hookup to add new materials models.

3.1 Reformulation of the Unit Cell Problem

To solve for Eq. (15), we define the following function:

$$\psi\left(\Delta\varepsilon_{ij}^{(\alpha)}, \Delta\bar{\delta}_{\hat{n}}^{(\xi)}\right) \equiv \begin{cases} \Delta\varepsilon_{ij}^{(\beta)} - \sum_{I=1}^{N}\sum_{\alpha=1}^{n_I} {}^{I}P_{ijkl}^{(\beta\alpha)}\Delta^{I}\bar{\mu}_{kl}^{(\alpha)} \\ - \sum_{\xi=1}^{m} Q_{ij\hat{n}}^{(\beta\xi)}\Delta\bar{\delta}_{\hat{n}}^{(\xi)} - A_{ijkl}^{(\beta)}\Delta\bar{\varepsilon}_{kl}, \\ - \sum_{I=1}^{N}\sum_{\alpha=1}^{n_I} {}^{I}C_{\hat{n}kl}^{(\eta\alpha)}\Delta^{I}\bar{\mu}_{kl}^{(\alpha)} + \Delta t_{\hat{n}}^{(\eta)} \\ - \sum_{\xi=1}^{m} D_{\hat{n}\hat{m}}^{(\eta\xi)}\Delta\bar{\delta}_{\hat{m}}^{(\xi)} - B_{\hat{n}kl}^{(\eta)}\Delta\bar{\varepsilon}_{kl.} \end{cases} \tag{17}$$

The unknowns are the increments of phase strain $\Delta\varepsilon_{ij}^{(\alpha)}$ and phase separation $\Delta\bar{\delta}_{\hat{n}}^{(\xi)}$, whereas the macro strain $\Delta\bar{\varepsilon}_{kl}$ is prescribed by the macro problem. The goal is to solve the nonlinear equations $\psi\left(\Delta\varepsilon_{ij}^{(\alpha)}, \Delta\bar{\delta}_{\hat{n}}^{(\xi)}\right) = 0$ for the unknown $\Delta\varepsilon_{ij}^{(\alpha)}$ and $\Delta\bar{\delta}_{\hat{n}}^{(\xi)}$. The above equation is solved using the Newton method, which requires function derivatives with respect to variables $\chi = \left\{\Delta\varepsilon_{kl}^{(\alpha)}, \Delta\bar{\delta}_{\hat{m}}^{(\xi)}\right\}$

$$\frac{\partial\psi}{\partial\chi} = \begin{pmatrix} \delta_{\beta\alpha}I_{ijkl} - \sum_{I=1}^{N}\sum_{\alpha=1}^{n_I} {}^{I}P_{ijmn}^{(\beta\alpha)} \times \frac{\partial^{I}\Delta\bar{\mu}_{mn}^{(\alpha)}}{\partial\Delta\varepsilon_{kl}^{(\alpha)}} & -\sum_{\xi=1}^{m} Q_{ij\hat{m}}^{(\beta\xi)} \\ -\sum_{I=1}^{N}\sum_{\alpha=1}^{n_I} {}^{I}C_{\hat{n}mn} \times \frac{\partial^{I}\Delta\bar{\mu}_{mn}^{(\alpha)}}{\partial\Delta\varepsilon_{kl}^{(\alpha)}} & \delta_{\eta\xi}\frac{\partial\Delta t_{\hat{n}}^{(\xi)}}{\partial\Delta\bar{\delta}_{\hat{m}}^{(\xi)}} - \sum_{\xi=1}^{m} D_{\hat{n}\hat{m}}^{(\eta\xi)} \end{pmatrix} \tag{18}$$

where δ_{ij} is the Kronecker delta. After $\chi = \left\{\Delta\varepsilon_{kl}^{(\alpha)}, \Delta\bar{\delta}_{\hat{m}}^{(\xi)}\right\}$ is calculated, the eigenstrain ${}^{I}\bar{\mu}_{ij}^{(\alpha)}$ is subsequently computed from $\Delta\varepsilon_{ij}^{(\alpha)}$, whereas the macroscopic stress follows from Eq. (16).

3.2 Consistent Tangent Operator

Consistent tangent is critical for rapid convergence of the Newton method at the macroscale. Recall the macroscopic stress is given by

$$\Delta\bar{\sigma}_{ij} = \bar{L}_{ijkl}\Delta\bar{\varepsilon}_{kl} + \sum_{I=1}^{N}\sum_{\alpha=1}^{n_I} {}^{I}\bar{E}_{ijkl}^{(\alpha)}\,{}^{I}\Delta\bar{\mu}_{kl}^{(\alpha)} + \sum_{\xi=1}^{m}\bar{F}_{ij\hat{n}}^{(\xi)}\Delta\delta_{\hat{n}}^{(\xi)} \tag{19}$$

For convenience, we adopt the Einstein summation convention over eigenstrain types I, volume partitions α, and interface partitions ξ. Taking the derivative of $\Delta\bar{\sigma}_{ij}$ with respect to $\Delta\bar{\varepsilon}_{kl}$ yields

$$\frac{\partial\Delta\bar{\sigma}_{ij}}{\partial\Delta\bar{\varepsilon}_{kl}} = \bar{L}_{ijkl} + {}^{I}\bar{E}_{ijmn}^{(\alpha)}\frac{\partial^{I}\Delta\bar{\mu}_{mn}^{(\alpha)}}{\partial\Delta\bar{\varepsilon}_{kl}} + \bar{F}_{ij\hat{n}}^{(\xi)}\frac{\partial\Delta\bar{\delta}_{\hat{n}}^{(\xi)}}{\partial\Delta\bar{\varepsilon}_{kl}} \tag{20}$$

Using the chain rule, Eq. (20) can be expressed as

$$\frac{\partial\Delta\bar{\sigma}_{ij}}{\partial\Delta\bar{\varepsilon}_{kl}} = \bar{L}_{ijkl} + {}^{I}\bar{E}_{ijmn}^{(\alpha)}\frac{\partial^{I}\Delta\bar{\mu}_{mn}^{(\alpha)}}{\partial\Delta\varepsilon_{pq}^{(\alpha)}}\boxed{\frac{\partial\Delta\varepsilon_{pq}^{(\alpha)}}{\partial\Delta\bar{\varepsilon}_{kl}}} + \bar{F}_{ij\hat{n}}^{(\xi)}\boxed{\frac{\partial\Delta\bar{\delta}_{\hat{n}}^{(\xi)}}{\partial\Delta\bar{\varepsilon}_{kl}}} \tag{21}$$

The unknown quantities in the boxes are obtained as follows. Recall the reduced-order unit cell problem:

$$\begin{aligned} &\Delta\varepsilon_{ij}^{(\beta)} - {}^{I}P_{ijkl}^{(\beta\alpha)}\,{}^{I}\Delta\bar{\mu}_{kl}^{(\alpha)} - Q_{ij\hat{n}}^{(\beta\xi)}\Delta\bar{\delta}_{\hat{n}}^{(\xi)} = A_{ijkl}^{(\beta)}\Delta\bar{\varepsilon}_{kl} \\ &-{}^{I}C_{\hat{n}kl}^{(\eta\alpha)}\,{}^{I}\Delta\bar{\mu}_{kl}^{(\alpha)} + \Delta t_{\hat{n}}^{(\eta)} - D_{\hat{n}\hat{m}}^{(\eta\xi)}\Delta\bar{\delta}_{\hat{m}}^{(\xi)} = B_{\hat{n}kl}^{(\eta)}\Delta\bar{\varepsilon}_{kl} \end{aligned} \tag{22}$$

Taking the derivative of (22) with respect to $\Delta\bar{\varepsilon}_{kl}$ gives

$$\begin{aligned} &\frac{\partial\Delta\varepsilon_{ij}^{(\beta)}}{\partial\Delta\bar{\varepsilon}_{kl}} - {}^{I}P_{ijmn}^{(\beta\alpha)}\frac{\partial^{I}\Delta\bar{\mu}_{mn}^{(\alpha)}}{\partial\Delta\bar{\varepsilon}_{kl}} - Q_{ij\hat{n}}^{(\beta\xi)}\frac{\partial\Delta\bar{\delta}_{\hat{n}}^{(\xi)}}{\partial\Delta\bar{\varepsilon}_{kl}} = A_{ijkl}^{(\beta)} \\ &-{}^{I}C_{\hat{n}mn}^{(\eta\alpha)}\frac{\partial^{I}\Delta\bar{\mu}_{mn}^{(\alpha)}}{\partial\Delta\bar{\varepsilon}_{kl}} + \frac{\partial\Delta t_{\hat{n}}^{(\eta)}}{\partial\Delta\bar{\varepsilon}_{kl}} - D_{\hat{n}\hat{m}}^{(\eta\xi)}\frac{\partial\Delta\bar{\delta}_{\hat{m}}^{(\xi)}}{\partial\Delta\bar{\varepsilon}_{kl}} = B_{\hat{n}kl}^{(\eta)} \end{aligned} \tag{23}$$

By the chain rule we have

$$\begin{aligned} &\left(\delta_{\beta\alpha}I_{ijpq} - {}^{I}P_{ijmn}^{(\beta\alpha)}\frac{\partial^{I}\Delta\bar{\mu}_{mn}^{(\alpha)}}{\partial\Delta\varepsilon_{pq}^{(\alpha)}}\right)\boxed{\frac{\partial\Delta\varepsilon_{pq}^{(\alpha)}}{\partial\Delta\bar{\varepsilon}_{kl}}} \\ &-Q_{ij\hat{n}}^{(\beta\xi)}\delta_{\hat{n}\hat{m}}\boxed{\frac{\partial\Delta\bar{\delta}_{\hat{m}}^{(\xi)}}{\partial\Delta\bar{\varepsilon}_{kl}}} = A_{ijkl}^{(\beta)} \\ &-{}^{I}C_{\hat{n}mn}^{(\eta\alpha)}\frac{\partial^{I}\Delta\bar{\mu}_{mn}^{(\alpha)}}{\partial\Delta\varepsilon_{pq}^{(\alpha)}}\boxed{\frac{\partial\Delta\varepsilon_{pq}^{(\alpha)}}{\partial\Delta\bar{\varepsilon}_{kl}}} \\ &+\left(\delta_{\eta\xi}\frac{\partial\Delta t_{\hat{n}}^{(\xi)}}{\partial\Delta\bar{\delta}_{\hat{m}}^{(\xi)}} - D_{\hat{n}\hat{m}}^{(\eta\xi)}\right)\boxed{\frac{\partial\Delta\bar{\delta}_{\hat{m}}^{(\xi)}}{\partial\Delta\bar{\varepsilon}_{kl}}} = B_{\hat{n}kl}^{(\eta)} \end{aligned} \tag{24}$$

The unknown quantities in the boxes can be expressed as

$$\begin{pmatrix} \boxed{\dfrac{\partial \Delta \varepsilon_{pq}^{(\alpha)}}{\partial \Delta \bar{\varepsilon}_{kl}}} \\ \boxed{\dfrac{\partial \Delta \bar{\delta}_{\hat{m}}^{(\xi)}}{\partial \Delta \bar{\varepsilon}_{kl}}} \end{pmatrix} = \begin{pmatrix} \delta_{\beta\alpha} I_{ijpq} & -Q_{ij\hat{m}}^{(\beta\xi)} \\ -{}^{I}P_{ijmn}^{(\beta\alpha)} \dfrac{\partial {}^{I}\Delta \bar{\mu}_{mn}^{(\alpha)}}{\partial \Delta \varepsilon_{pq}^{(\alpha)}} & \\ -{}^{I}C_{\hat{n}mn}^{(\eta\alpha)} \dfrac{\partial {}^{I}\Delta \bar{\mu}_{mn}^{(\alpha)}}{\partial \Delta \varepsilon_{pq}^{(\alpha)}} & \delta_{\eta\xi} \dfrac{\partial \Delta t_{\hat{n}}^{(\xi)}}{\partial \Delta \bar{\delta}_{\hat{m}}^{(\xi)}} - D_{\hat{n}\hat{m}}^{(\eta\xi)} \end{pmatrix}^{-1} \times \begin{pmatrix} A_{ijkl}^{(\beta)} \\ B_{\hat{n}kl}^{(\eta)} \end{pmatrix} \tag{25}$$

Finally, the macroscopic consistent tangent $(\partial \Delta \bar{\sigma}_{ij})/(\partial \Delta \bar{\varepsilon}_{kl})$ follows from Eq. (21).

3.3 Canonical Structure of the Unit Cell Problem

Consider the remaining unknowns denoted in the previous sections, $(\partial {}^{I}\Delta \bar{\mu}_{ij}^{(\alpha)})/(\partial \Delta \varepsilon_{kl}^{(\alpha)})$ and $(\partial \Delta t_{\hat{n}}^{(\xi)})/(\partial \Delta \bar{\delta}_{\hat{m}}^{(\xi)})$. Note that these derivatives are taken with respect to the increment of strain or eigenseparation in the corresponding phase α or interface ξ. These quantities can be derived from a single-scale constitutive model or cohesive law (see Appendix for various material models). $(\partial \Delta t_{\hat{n}}^{(\xi)})/(\partial \Delta \bar{\delta}_{\hat{m}}^{(\xi)})$ is the relation between the traction and displacement jump, which can be specified by the cohesive law.

We now focus on the derivative of the eigenstrain. By definition, the eigenstrain is given as

$${}^{I}\Delta \bar{\mu}_{ij}^{(\alpha)} = \Delta \varepsilon_{ij}^{(\alpha)} - M_{ijkl}^{(\alpha)} \Delta \sigma_{kl}^{(\alpha)} \tag{26}$$

where $M_{ijkl}^{(\alpha)}$ is the elastic compliance tensor for phase partition α. The derivative of the eigenstrain is given by

$$\frac{\partial {}^{I}\Delta \bar{\mu}_{ij}^{(\alpha)}}{\partial \Delta \varepsilon_{kl}^{(\alpha)}} = \frac{\partial}{\partial \Delta \varepsilon_{kl}^{(\alpha)}} \left(\Delta \varepsilon_{ij}^{(\alpha)} - M_{ijmn}^{(\alpha)} \Delta \sigma_{mn}^{(\alpha)} \right) = I_{ijkl} - M_{ijmn}^{(\alpha)} \frac{\partial \Delta \sigma_{mn}^{(\alpha)}}{\partial \Delta \varepsilon_{kl}^{(\alpha)}} \tag{27}$$

where $(\partial \Delta \sigma_{mn}^{(\alpha)})/(\partial \Delta \varepsilon_{kl}^{(\alpha)})$ is a single-scale consistent tangent stiffness for the corresponding phase. Formulation of the consistent tangent operator for each phase is a standard building block in any implicit finite element code. Given the $(\partial \Delta \sigma_{mn}^{(\alpha)})/(\partial \Delta \varepsilon_{kl}^{(\alpha)})$, the eigenstrain derivative $(\partial {}^{I}\Delta \bar{\mu}_{ij}^{(\alpha)})/(\partial \Delta \varepsilon_{kl}^{(\alpha)})$ can be found from (27). Consequently, the nonlinear unit cell problem can be solved (see Section 3.1) and the macroscopic consistent tangent stiffness $(\partial \Delta \bar{\sigma}_{ij})/(\partial \Delta \bar{\varepsilon}_{kl})$ can be obtained as described in Section 3.2. Figure 1 depicts the canonical structure of the reduced-order homogenization and its implementation in the commercial finite element code.

Note that in general, the unit cell problem is solved for the internal variables in addition to eigenstrains and eigenseparations. In the following, we present a nested Newton method that can handle various material models in the context of ABAQUS code.

Let $n = 1 \rightarrow n_{\max}$ be the iteration count for the macro problem and denote it by the right subscript. Let $iter = 1 \rightarrow iter_{\max}$ be the iteration count for the unit cell problem and denote it by the left superscript.

Given: $\bar{\varepsilon}_{ij(n)}$, $\chi_{(n)} = \left\{ \varepsilon_{ij(n)}^{(\alpha)}, \bar{\delta}_{\hat{n}(n)}^{(\xi)} \right\}$, $\sigma_{ij(n)}^{(\alpha)}$, $t_{\hat{n}(n)}^{(\xi)}$, $\gamma_{(n)}^{(\alpha)}$, where γ is an internal variable, α the α^{th} phase partition, ξ the ξ^{th} interface partition, and $\Delta \bar{\varepsilon}_{ij(n+1)}$ the macro strain increment.

Find: $\Delta \bar{\sigma}_{ij(n+1)}$, $\Delta \chi_{(n+1)} = \left\{ \Delta \varepsilon_{ij(n+1)}^{(\alpha)}, \Delta \bar{\delta}_{\hat{n}(n+1)}^{(\xi)} \right\}$, $\sigma_{ij(n+1)}^{(\alpha)}$, $t_{\hat{n}(n+1)}^{(\xi)}$, $\gamma_{(n+1)}^{(\alpha)}$.

Recalling the function ψ from Eq. (17), we have the following stress update algorithm:

Algorithm 1 Stress update procedure

1. Initialize ${}^{0}\Delta \chi_{(n+1)} = \left\{ {}^{0}\Delta \varepsilon_{ij(n+1)}^{(\alpha)}, {}^{0}\Delta \bar{\delta}_{\hat{n}(n+1)}^{(\xi)} \right\} = 0$.

2. Compute

$${}^{(iter)}\Delta \chi_{(n+1)} = {}^{(iter-1)}\Delta \chi_{(n+1)} - \left[\frac{\partial \psi \left({}^{(iter-1)}\Delta \chi_{(n+1)}, \Delta \bar{\varepsilon}_{ij(n+1)} \right)}{\partial {}^{(iter-1)}\Delta \chi_{(n+1)}} \right]^{-1} \times \psi \left({}^{(iter-1)}\Delta \chi_{(n+1)}, \Delta \bar{\varepsilon}_{ij(n+1)} \right)$$

3. Use ${}^{(iter)}\Delta \chi_{(n)}$, $\sigma_{ij(n)}^{(\alpha)}$, $t_{\hat{n}(n)}^{(\xi)}$, $\gamma_{(n)}^{(\alpha)}$, in Newton method to solve for the material internal variable ${}^{(iter)}\gamma_{(n+1)}^{(\alpha)}$ for microscopic phases.

4. Get ${}^{(iter)}\sigma_{ij(n+1)}^{(\alpha)}$, ${}^{(iter)}t_{\hat{n}(n)}^{(\xi)}$ from ${}^{(iter)}\gamma_{(n+1)}^{(\alpha)}$.

5. Compute ${}^{(iter)}\Delta \bar{\mu}_{ij(n+1)}^{(\alpha)} = {}^{(iter)}\Delta \varepsilon_{ij(n+1)}^{(\alpha)} - M_{ijkl}^{(\alpha)} {}^{(iter)}\Delta \sigma_{kl(n+1)}^{(\alpha)}$.

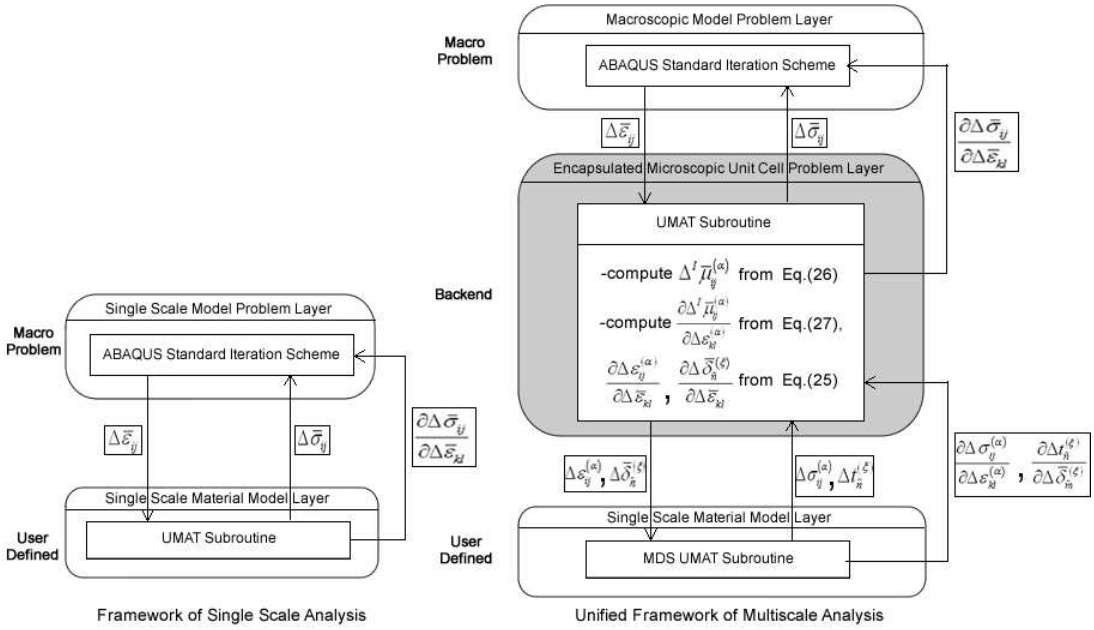

FIG. 1: Canonical structure of the unit cell problem.

6. Compute $\dfrac{\partial \psi\left({}^{(iter)}\Delta\chi_{(n+1)},\ \Delta\bar{\varepsilon}_{ij(n+1)}\right)}{\partial {}^{(iter)}\Delta\chi_{(n+1)}}$.

7. Check whether $\psi\left({}^{(iter)}\Delta\chi_{(n+1)}, \Delta\bar{\varepsilon}_{ij(n+1)}\right) < tol$; if yes, go to step 9; if no, go to step 8.

8. Let $iter = iter + 1$. Go to step 2.

9. Let $\sigma^{(\alpha)}_{ij(n+1)} = {}^{(iter)}\sigma^{(\alpha)}_{ij(n+1)}$, $t^{(\xi)}_{\hat{n}(n+1)} = {}^{(iter)}t^{(\xi)}_{\hat{n}(n+1)}$, $\gamma^{(\alpha)}_{(n+1)} = {}^{(iter)}\gamma^{(\alpha)}_{(n+1)}$, $\Delta\chi_{(n+1)} = {}^{(iter)}\Delta\chi_{(n+1)}$, and $\Delta\bar{\mu}^{(\alpha)}_{ij(n+1)} = {}^{(iter)}\Delta\bar{\mu}^{(\alpha)}_{ij(n+1)}$, update $\Delta\bar{\sigma}_{ij(n+1)}$ from Eq. (19).

10. Check the residual in macroanalysis. If $R_{macro(n+1)} < tol_{macro}$ go to the next time interval $\Delta t'$; otherwise, let $n = n + 1$, calculate new $\Delta\bar{\varepsilon}_{ij(n+1)}$, and go to step 1.

In step 10, once the strain increment $\Delta\bar{\varepsilon}_{ij(n+1)}$ has been updated, the consistent tangent $(\partial\Delta\bar{\sigma}_{ij(n+1)})/(\partial\Delta\bar{\varepsilon}_{kl(n+1)})$ is computed based on Section 3.2.

4. EXAMPLES

From the user's perspective, the canonical structure of the reduced-order homogenization allows addition of new material models without familiarity with the formulation. The user-defined routine "MDS UMAT" in Fig. 1 follows the same syntax as the standard UMAT function in ABAQUS (ABAQUS 6.8 documentation). In this section and in the Appendix we consider three material models of microconstituents to demonstrate the implementation of the formulation. In all examples we consider the fibrous composite unit cell[1] shown in Fig. 2. The elastic properties of microconstituents are given in Table 1. Numerical

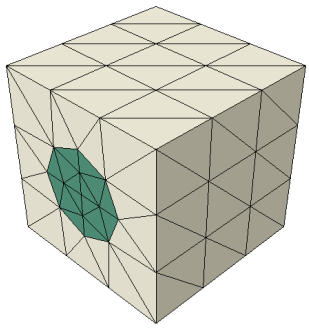

FIG. 2: Fibrous composite unit cell.

[1]The user can define any shape of unit cell. Here we give an example which is also the most common one.

TABLE 1: Elastic properties of micro unit cell.

Vol. Frac. = 22%	Young's modulus	Poisson ratio
Matrix	1.31E+5 MPa	0.36
Fiber	2.62E+5 MPa	0.36

results are compared against the direct homogenization for verification purposes. For simplicity, the superscripts denoting partition number are omitted. Constitutive models of continuum damage mechanics, plasticity, and viscoplasticity are detailed in the Appendix.

4.1 Continuum Damage Mechanics Example

The damage parameters considered in this study are summarized in Table 2. Two tension tests are performed. The first is loading along the fiber direction; the second is loading orthogonal to the fibers. Figures 3 and 4 depict the strain/stress responses for the two cases, respectively. For the first case, there is almost no difference between the reduced-order homogenization and direct homogenization. For the second case, the reduced-order homogenization with one partition per phase gives rise to higher failure stress than the direct homogenization. To alleviate the problem one can either increase the number of partitions or calibrate the phase partition properties [see Fish and Yuan (2008), Oskay and Fish (2007), and Yuan and Fish (2009) for details].

TABLE 2: Damage parameters for the fiber and matrix phases.

	S (MPa)	G (MJ/m^3)	c
Matrix	300	0.1	0
Fiber	600	0.2	0

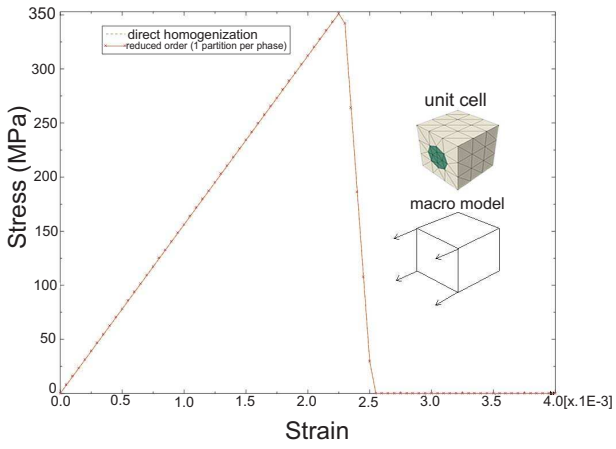

FIG. 3: Tension test under damage law (along fiber direction).

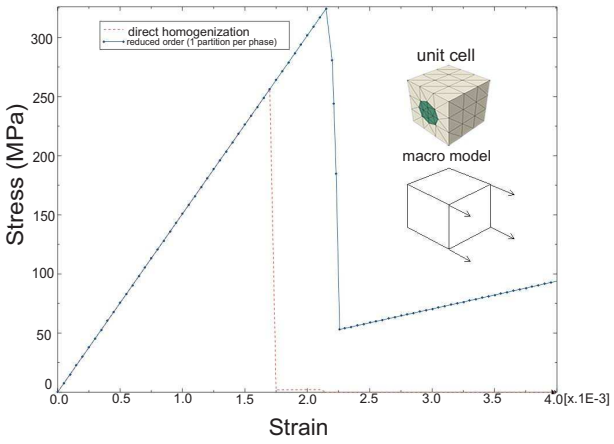

FIG. 4: Tension test under damage law (orthogonal to fiber direction).

4.2 Plasticity Example

We use the same tension tests as in the previous example. Plasticity parameters for the matrix phase are given in Table 3. Simulation results are shown in Figs. 5 and 6. It can be seen that as in the previous example, in the orthogonal to the fibers loading case the results are less accurate.

4.3 Viscoplasticity Example

In this example we consider the viscoplasticity law based on the overstress (VBO) (Tachibana and Krempl, 1995, 1997, 1998). The VBO parameters for the fiber and matrix phases are listed in Table 4. Creep simulation is performed with a constant stress load ($20\ \mathrm{MPa}$) applied in the orthogonal fiber direction. Figure 7 compares the reduced-order homogenization against the direct homogenization. The *x*-axis is the elapsed time and the *y*-axis denotes the strain evolution in the loading direction.

TABLE 3: Plasticity parameters for the matrix phase.

	σ_Y (MPa)	H (MPa)	θ
Matrix	50	1000	1.0

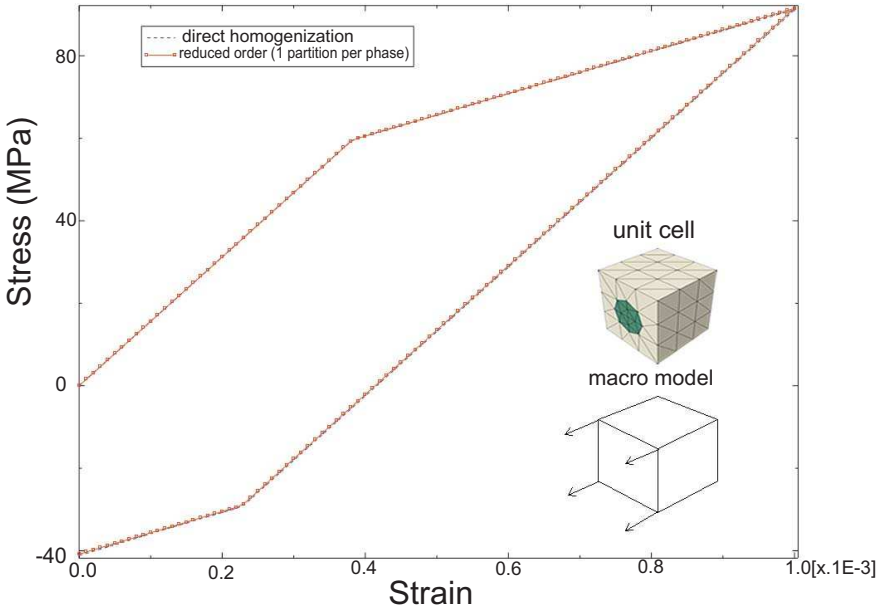

FIG. 5: Tension test under plasticity law (along fiber direction).

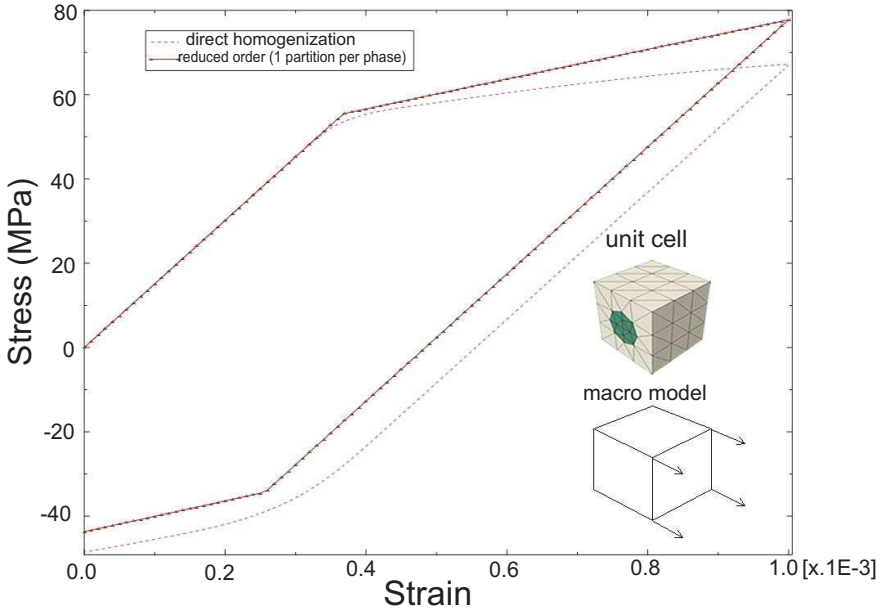

FIG. 6: Tension test under plasticity law (orthogonal to fiber direction).

TABLE 4: VBO parameters for the fiber–matrix phases.

	ψ **(MPa)**	k_1	k_2 **(MPa)**	k_3	A_0 **(MPa)**	A_c	A_f **(MPa)**	R **(1/s)**
Matrix	32750.0	0.305	26.0	5.0	28.0	213.0	1.0	1.97E-5
Fiber	65500.0	0.610	52.0	10.0	56.0	1260.0	2.0	1.97E-5

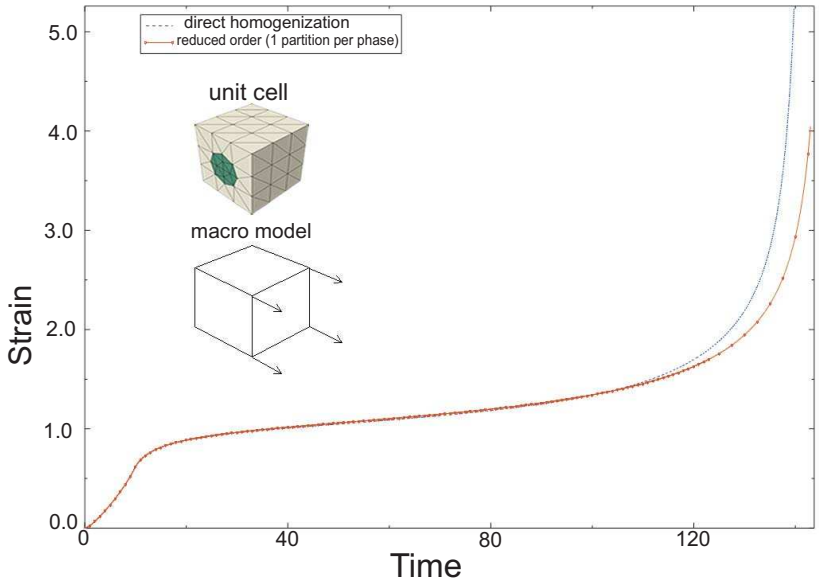

FIG. 7: Creep simulation under VBO law (orthogonal to fiber direction).

ACKNOWLEDGEMENTS

Financial support from the Automotive Composites Consortium, General Electric, and Dassault Systémes are gratefully acknowledged.

REFERENCES

ABAQUS 6.8 Documentation, *User Subroutines Reference Manual*, http://www.simulia.com.

Fish, J., Shek, K., Pandheeradi, M., and Shephard, M. S., Computational plasticity for composite structure based on mathematical homogenization: Theory and practice, *Comp. Meth. Appl. Mech. Eng.*, vol. **148**, pp. 53–73, 1997.

Fish, J. and Yu, Q., Multiscale damage modeling for composite materials: Theory and computational framework, *Int. J. Num. Meth. Eng.*, vol. **52**(1-2), pp. 161–192, 2001.

Fish, J. and Yuan, Z., N-scale model reduction theory, in *Bridging the Scales in Science and Engineering*, J. Fish, Ed., Oxford University Press, 2008.

Guedes, J. M. and Kikuchi, N., Preprocessing and postprocessing for materials based on the homogenization method with adaptive finite element methods, *Comp. Meth. Appl. Mech. Eng.*, vol. **83**, pp. 143–198, 1990.

Hill, R., A self-consistent mechanics of composite materials, *J. Mech. Phys. Solids*, vol. **13**, pp. 357–372, 1965.

Mori, T. and Tanaka, K., Average stress in the matrix and average elastic energy of materials with misfitting inclusions, *Acta Metall.*, vol. **21**, pp. 571–574, 1973.

Oskay, C. and Fish, J., Eigendeformation-based reduced order homogenization, *Comp. Meth. Appl. Mech. Eng.*, vol. **196**, pp. 1216–1243, 2007.

Tachibana, Y. and Krempl, E., Modeling of high homologous temperature deformation behavior using the viscoplasticity theory based on overstress (VBO): Part I. Creep and tensile behavior, *J. Eng. Mater. Technol., ASME*, vol. **117**, pp. 456–461, 1995.

Tachibana, Y. and Krempl, E., Modeling of high homologous temperature deformation behavior using the viscoplasticity theory based on overstress (VBO): Part II. Characteristics of the VBO model, *J. Eng. Mater. Technol., ASME*, vol. **119**, pp. 1–6, 1997.

Tachibana, Y. and Krempl, E., Modeling of high homologous temperature deformation behavior using the viscoplasticity theory based on overstress (VBO): Part III. A simplified model, *J. Eng. Mater. Technol., ASME*, vol. **120**, pp. 193–196, 1998.

Terada, K. and Kikuchi, N., Nonlinear homogenization method for practical applications, *Comput. Methods Micromech.*, S. Ghosh and M. Ostoja-Starzewski, Eds., ASME, New York, AMD-212/MD-62, pp. 1–16, 1995.

Yu, Q., Fish, J., and Shek, K. L., Computational damage mechanics for composite materials based on mathematical homogenization, *Int. J. Num. Meth. Eng.*, vol. **45**, pp. 1657–1679, 1999.

Yuan, Z. and Fish, J., Towards realization of computational homogenization in practice, *Int. J. Num. Meth. Eng.*, vol. **73**(3), pp. 361–380, 2008.

Yuan, Z. and Fish, J., Multiple scale eigendeformation-based reduced order homogenization, *Comp. Meth. Appl. Mech. Eng.*, vol. **198**, pp. 2016–2038, 2009.

APPENDIX

A. CONTINUUM DAMAGE

We consider a piecewise isotropic damage law for both phases. Let ω be the damage parameter. The inelastic strain (or eigenstrain) ε^{in}_{ij} is given by $\omega\varepsilon_{ij}$, where ε_{ij} is the total strain. Consider the $(n+1)^{th}$ iteration. Following Fig. 1, given $\Delta\varepsilon_{ij(n+1)}$, we need to calculate the stress increment $\Delta\sigma_{ij(n+1)}$ and consistent tangent $(\partial\Delta\sigma_{ij(n+1)})/(\partial\Delta\varepsilon_{kl(n+1)})$ for each micro phase. From the stress definition, we have

$$\begin{aligned}\Delta\sigma_{ij(n+1)} &= L_{ijkl}\left(\Delta\varepsilon_{kl(n+1)} - \Delta\varepsilon^{in}_{kl(n+1)}\right)\\ &= L_{ijkl}\Big(\Delta\varepsilon_{kl(n+1)} - \omega_{(n+1)}\varepsilon_{kl(n+1)}\\ &\quad + \omega_{(n)}\varepsilon_{kl(n)}\Big)\end{aligned} \tag{A.1}$$

and the consistent tangent is given by

$$\begin{aligned}\frac{\partial\Delta\sigma_{ij(n+1)}}{\partial\Delta\varepsilon_{kl(n+1)}} &= L_{ijkl} - L_{ijmn}\frac{\partial\left(\omega_{(n+1)}\varepsilon_{mn(n+1)}\right)}{\partial\Delta\varepsilon_{kl(n+1)}}\\ &= L_{ijkl} - \omega_{(n+1)}L_{ijkl} - L_{ijmn}\varepsilon_{mn(n+1)}\\ &\quad\times\frac{\partial\omega_{(n+1)}}{\partial\Delta\varepsilon_{kl(n+1)}}\end{aligned} \tag{A.2}$$

The last term in (A2) depends on the evolution of damage parameter ω. Here we adopt a linear stress/strain relation as shown in Fig. 8.

In Fig. 8, S is the critical stress at the end of the elastic process and G is the area under the stress/strain curve or the strain energy density. The evolution of the damage parameter is defined as

$$\omega = \begin{cases} 0, & \|\varepsilon\|^{eq} < k_i \\ \dfrac{\omega_{\max}k_f}{\|\varepsilon\|^{eq}}\dfrac{\|\varepsilon\|^{eq}-k_i}{k_f-k_i}, & k_i \le \|\varepsilon\|^{eq} \le k_f \\ \omega_{\max}, & \|\varepsilon\|^{eq} > k_f \end{cases} \tag{A.3}$$

$$k_i = \frac{S}{E_a}, \quad k_f = \frac{2G}{S} \tag{A.4}$$

where E_a is the elastic modulus in the loading direction. The equivalent strain is defined as $\|\varepsilon(t)\|^{eq} = \max\left(\sqrt{[\![\hat{\varepsilon}_I(T)]\!]\cdot[\![\hat{\varepsilon}_I(T)]\!]}, T\le t\right)$ where $\hat{\varepsilon}_I$ are the principal components. $[\![x]\!]$ is defined as follows:

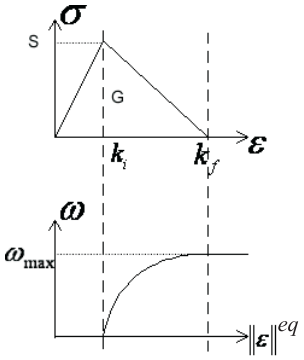

FIG. 8: Damage parameter evolution.

$$[\![x]\!] = \begin{cases} x, & \text{if} \quad x \ge 0 \\ cx, & \text{otherwise} \end{cases} \tag{A.5}$$

where c is a material parameter.

Derivation of $(\partial\omega_{(n+1)})/(\partial\Delta\varepsilon_{ij(n+1)})$ in Eq. (A2) follows from the chain rule.

$$\begin{aligned}\frac{\partial\omega_{(n+1)}}{\partial\Delta\varepsilon_{ij_{(n+1)}}} &= \frac{\partial\omega_{(n+1)}}{\partial\|\varepsilon\|^{eq}_{(n+1)}}\frac{\partial\|\varepsilon\|^{eq}_{(n+1)}}{\partial[\![\hat{\varepsilon}_{I_{(n+1)}}]\!]}\\ &\quad\times\frac{\partial[\![\hat{\varepsilon}_{I_{(n+1)}}]\!]}{\partial\hat{\varepsilon}_{J_{(n+1)}}}\frac{\partial\hat{\varepsilon}_{J_{(n+1)}}}{\partial\varepsilon_{kl_{(n+1)}}}\frac{\partial\varepsilon_{kl(n+1)}}{\partial\Delta\varepsilon_{ij_{(n+1)}}}\end{aligned} \tag{A.6}$$

where

$$\frac{\partial\omega}{\partial\|\varepsilon\|^{eq}} = \frac{k_ik_f}{\left(\|\varepsilon\|^{eq}\right)^2(k_f-k_i)} \tag{A.7}$$

$$\frac{\partial\|\varepsilon\|^{eq}_{(n+1)}}{\partial[\![\hat{\varepsilon}_{I_{(n+1)}}]\!]} = \frac{[\![\hat{\varepsilon}_{I_{(n+1)}}]\!]}{\|\varepsilon\|^{eq}_{(n+1)}} \tag{A.8}$$

$$\frac{\partial[\![\hat{\varepsilon}_I]\!]}{\partial\hat{\varepsilon}_J} = \begin{cases} \delta_{IJ}, & \text{if} \quad \hat{\varepsilon}_I \ge 0 \\ c\delta_{IJ}, & \text{otherwise} \end{cases} \tag{A.9}$$

$$\begin{aligned}\frac{\partial\hat{\varepsilon}_{J_{(n+1)}}}{\partial\varepsilon_{ij_{(n+1)}}} &= \left[3\left(\hat{\varepsilon}_{J_{(n+1)}}\right)^2 - 2I_1\hat{\varepsilon}_{J_{(n+1)}} + I_2\right]^{-1}\\ &\quad\times\left[\frac{\partial I_1}{\partial\varepsilon_{ij_{(n+1)}}}\left(\hat{\varepsilon}_{J_{(n+1)}}\right)^2 - \frac{\partial I_2}{\partial\varepsilon_{ij_{(n+1)}}}\left(\hat{\varepsilon}_{J_{(n+1)}}\right)\right.\\ &\quad\left.+\frac{\partial I_3}{\partial\varepsilon_{ij_{(n+1)}}}\right]\end{aligned} \tag{A.10}$$

In Eq. (A10), I_1, I_2, I_3 are the three invariants given by

$$\begin{aligned} I_1 &= trace\,(\varepsilon_{ij}) = \hat{\varepsilon}_1 + \hat{\varepsilon}_2 + \hat{\varepsilon}_3 \\ I_2 &= \frac{1}{2}\left[(trace\,(\varepsilon_{ij}))^2 - trace\,(\varepsilon_{ik}\varepsilon_{kj})\right] \\ &= \hat{\varepsilon}_1\hat{\varepsilon}_2 + \hat{\varepsilon}_2\hat{\varepsilon}_3 + \hat{\varepsilon}_3\hat{\varepsilon}_1 \\ I_3 &= \det(\varepsilon_{ij}) = \hat{\varepsilon}_1\hat{\varepsilon}_2\hat{\varepsilon}_3 \end{aligned} \tag{A.11}$$

and their derivatives with respect to $\varepsilon_{ij_{(n+1)}}$ are

$$\begin{aligned} \frac{\partial I_1}{\partial \varepsilon_{ij_{(n+1)}}} &= \delta_{ij} \\ \frac{\partial I_2}{\partial \varepsilon_{ij_{(n+1)}}} &= I_1\delta_{ij} - \varepsilon_{ij_{(n+1)}} \\ \frac{\partial I_3}{\partial \varepsilon_{ij_{(n+1)}}} &= \varepsilon_{ik_{(n+1)}}\varepsilon_{kj_{(n+1)}} - I_1\varepsilon_{ij_{(n+1)}} + I_2\delta_{ij} \end{aligned} \tag{A.12}$$

Since $(\partial\varepsilon_{ij(n+1)})/(\partial\Delta\varepsilon_{kl(n+1)}) = I_{ijkl}$, the derivation of $(\partial\Delta\sigma_{ij(n+1)})/(\partial\Delta\varepsilon_{kl(n+1)})$ follows from Eq. (A2).

B. PLASTICITY

In this example we adopt the classical isotropic/kinematic hardening plasticity law for matrix phase with fibers being elastic. Consider the $(n+1)^{th}$ iteration. The stress increment is given by $\Delta\sigma_{ij(n+1)} = L_{ijkl}\Big(\Delta\varepsilon_{kl(n+1)} - \Delta\varepsilon^{in}_{kl(n+1)}\Big)$, where $\Delta\varepsilon^{in}_{kl(n+1)}$ is the plastic strain increment. The radial return algorithm is typically employed to ensure consistency.

Let α be the equivalent plastic strain that represents isotropic hardening of the von Mises yield surface, β_{ij} the back stress, ς_{ij} the relative elastic stress, and $\Delta\gamma$ the consistency parameter. For simplicity, we assume isotropic/kinematic hardening with a constant hardening modulus $\bar{H}$. We denote $K(\alpha) = \sigma_Y + \theta\bar{H}\alpha$ as an isotropic hardening and $H(\alpha) = (1-\theta)\bar{H}\alpha$ as a kinematic hardening. For pure isotropic hardening $\theta = 1$; for pure kinematic hardening $\theta = 0$. The stress update procedure and consistent tangent are summarized in the box below.

Algorithm 2 Radial return algorithm for plasticity with isotropic/kinematic hardening

1. Compute trial elastic stress.

$$\begin{aligned} e_{ij(n+1)} &= \varepsilon_{ij(n+1)} - \frac{1}{3}\delta_{ij}\varepsilon_{kk(n+1)} \\ s^{trial}_{ij(n+1)} &= 2\mu\left(e_{ij(n+1)} - \varepsilon^p_{ij(n)}\right) \\ \varsigma^{trial}_{ij(n+1)} &= s^{trial}_{ij(n+1)} - \beta_{ij(n)} \end{aligned}$$

2. Check yield condition

$$f^{trial}_{(n+1)} \equiv \left\|\varsigma^{trial}_{ij(n+1)}\right\| - \sqrt{\frac{2}{3}}K\left(\alpha_{(n)}\right)$$

   If $f^{trial}_{(n+1)} \le 0$, then set $(\cdot)_{(n+1)} = (\cdot)^{trial}_{(n+1)}$ and exit.

3. Compute the unit vector $n_{ij(n+1)} \equiv \frac{\varsigma^{trial}_{ij(n+1)}}{\left\|\varsigma^{trial}_{ij(n+1)}\right\|}$.

4. Use Newton method to solve for $\Delta\gamma$ from

$$\begin{aligned} g(\Delta\gamma) \equiv &-\sqrt{\frac{2}{3}}K\left(\alpha^{trial}_{(n+1)}\right) + \left\|\varsigma^{trial}_{ij(n+1)}\right\| \\ &- \left\{2\mu\Delta\gamma + \sqrt{\frac{2}{3}}\left[H\left(\alpha^{trial}_{(n+1)}\right) - H\left(\alpha_{(n)}\right)\right]\right\} = 0 \end{aligned}$$

   where $\alpha^{trial}_{(n+1)} = \alpha_{(n)} + \sqrt{2/3}\Delta\gamma$.

5. Update the equivalent plastic strain $\alpha_{(n+1)} = \alpha^{trial}_{(n+1)}$.

6. Update the back stress, plastic strain and stress.

$$\begin{aligned} \beta_{ij(n+1)} &= \beta_{ij(n)} + \sqrt{\frac{2}{3}}\Big[H\left(\alpha_{(n+1)}\right) \\ &\quad - H\left(\alpha_{(n)}\right)\Big]n_{ij(n+1)} \\ \varepsilon^p_{ij(n+1)} &= \varepsilon^p_{ij(n)} + \Delta\gamma n_{ij(n+1)} \\ \Delta\sigma_{ij(n+1)} &= L_{ijkl}\left(\Delta\varepsilon_{kl(n+1)} - \Delta\gamma n_{kl(n+1)}\right) \end{aligned}$$

7. Compute the consistent tangent

$$\begin{aligned} \frac{\partial\Delta\sigma_{ij_{(n+1)}}}{\partial\Delta\varepsilon_{kl_{(n+1)}}} &= L_{ijkl} - 2\mu \\ &\times\left(n_{ij_{(n+1)}}\frac{\partial\Delta\gamma_{(n+1)}}{\partial\Delta\varepsilon_{kl_{(n+1)}}} + \Delta\gamma_{(n+1)}\frac{\partial n_{ij_{(n+1)}}}{\partial\Delta\varepsilon_{kl_{(n+1)}}}\right). \end{aligned}$$

   where

$$\begin{aligned} \frac{\partial\Delta\gamma_{(n+1)}}{\partial\Delta\varepsilon_{kl_{(n+1)}}} &= \left[1 + \frac{K'_{(n+1)} + H'_{(n+1)}}{3\mu}\right]^{-1} n_{kl_{(n+1)}} \\ \frac{\partial n_{ij_{(n+1)}}}{\partial\Delta\varepsilon_{kl_{(n+1)}}} &= \frac{2\mu}{\left\|\varsigma^{trial}_{ij(n+1)}\right\|} \\ &\times\left(I_{ijkl} - \frac{1}{3}\delta_{ij}\delta_{kl} - n_{ij_{(n+1)}}n_{kl_{(n+1)}}\right) \end{aligned}$$

C. VISCOPLASTICITY

As in the previous two models the basic assumption is that the rate of total strain can be additively decomposed into elastic and inelastic parts, which gives

$$\dot{\varepsilon}_{ij} = \dot{\varepsilon}^{el}_{ij} + \dot{\varepsilon}^{in}_{ij} \tag{C.1}$$

The corresponding deviatoric expression is given as

$$\dot{\eta}_{ij} = \dot{\eta}^{el}_{ij} + \dot{\eta}^{in}_{ij} \tag{C.2}$$

where

$$\dot{\eta}_{ij} = \dot{\varepsilon}_{ij} - \frac{1}{3}\delta_{ij}\dot{\varepsilon}_{kk} \tag{C.3}$$

The inelastic part of strain is assumed to be volume preserving; thus, the inelastic strain rate is deviatoric

$$\dot{\eta}^{in}_{ij} = \dot{\varepsilon}^{in}_{ij} \tag{C.4}$$

The rate form of the stress–strain relation is given as

$$\dot{\sigma}_{ij} = L_{ijkl}\dot{\varepsilon}^{el}_{kl} = L_{ijkl}\left(\dot{\varepsilon}_{kl} - \dot{\varepsilon}^{in}_{kl}\right) \tag{C.5}$$

The material is assumed to be isotropic

$$L_{ijkl} = \lambda\delta_{ij}\delta_{kl} + \mu\delta_{ik}\delta_{jl} + \mu\delta_{il}\delta_{jk} \tag{C.6}$$

The corresponding deviatoric expression is given as

$$\dot{s}_{ij} = 2\mu\dot{\eta}^{el}_{ij} = 2\mu\left(\dot{\eta}_{ij} - \dot{\eta}^{in}_{ij}\right) \tag{C.7}$$

where

$$\dot{s}_{ij} = \dot{\sigma}_{ij} - \frac{1}{3}\delta_{ij}\dot{\sigma}_{kk} \tag{C.8}$$

C.1 Overstress and Evolution of Inelastic Strain

In order to evaluate the evolution of the inelastic strain, the concept of overstress is introduced. The overstress deviator is given as

$$o_{ij} = s_{ij} - g_{ij} \tag{C.9}$$

where g_{ij} is defined as the equilibrium stress deviator. The scalar invariant of the overstress deviator (or equivalent overstress) is defined as

$$\Gamma = \sqrt{\frac{3}{2}o_{ij}o_{ij}} \tag{C.10}$$

and the normalized tensor of overstress deviator is given as

$$n_{ij} = \sqrt{\frac{3}{2}}\frac{o_{ij}}{\Gamma} \tag{C.11}$$

With the introduction of overstress, the inelastic strain rate is given as

$$\dot{\eta}^{in}_{ij} = \sqrt{\frac{3}{2}}\dot{\bar{\eta}}^{in}n_{ij} \tag{C.12}$$

where $\dot{\bar{\eta}}^{in}$ is the equivalent inelastic strain rate defined as

$$\dot{\bar{\eta}}^{in} = \frac{\Gamma}{Ek\left(\Gamma\right)} \tag{C.13}$$

where E is Young's modulus; k is positive and a decreasing function of the equivalent overstress Γ and acts as a repository for nonlinear viscous behavior. A recommended form is given as

$$k = k_1\left(1 + \frac{\Gamma}{k_2}\right)^{-k_3} \tag{C.14}$$

where k_1, k_2, and k_3 are model parameters.

With the definition of the inelastic strain rate, the rate form of stress–strain relation can be rewritten as

$$\dot{\sigma}_{ij} = L_{ijkl}\dot{\varepsilon}_{kl} - \sqrt{6}\mu\dot{\bar{\eta}}^{in}n_{ij} \tag{C.15}$$

The corresponding deviatoric expression is given as

$$\dot{s}_{ij} = 2\mu\dot{\eta}_{ij} - \sqrt{6}\mu\dot{\bar{\eta}}^{in}n_{ij} \tag{C.16}$$

C.2 Evolution of Equilibrium Stress

The high-homologous temperature VBO model has the equilibrium stress evolution equation expressed in rate the form as

$$\dot{g}_{ij} = \frac{\psi}{E}\left[\dot{s}_{ij} + \frac{o_{ij}}{k} - \frac{\Gamma}{k}\frac{g_{ij}}{A}\right] - R\left\|g_{ij}\right\|g_{ij} \tag{C.17}$$

where ψ and R are model constants, and A is the isotropic stress introduced to model the cyclic hardening or softening behavior. The evolution form is given as

$$\dot{A} = A_c\left(A_f - A\right)\dot{\bar{\eta}}^{in} \tag{C.18}$$

with the initial condition

$$A\left(t = 0\right) = A_0 \tag{C.19}$$

where A_c, A_f, and A_0 are model parameters.

Now, with the explanation of all parameters, the VBO model for high homologous temperature has been introduced.

C.3 Integration Scheme of the VBO Model

The problem of stress update can be stated as follows: given the value of at the time $t_{(n)}$ and the strain increment $\Delta\varepsilon_{ij(n+1)}$, find the value of at the time $t_{(n+1)}$.

Using the backward Euler integration scheme, the stress update is given as

$$\sigma_{ij(n+1)} = \sigma_{ij(n)} + \Delta t\dot{\sigma}_{ij(n+1)} \tag{C.20}$$

Referring to Eqs. (C15) and (C16), the stress and stress deviator at time $t_{(n+1)}$ can be expressed as

$$\sigma_{ij(n+1)} = \sigma^{trial}_{ij(n+1)} - \sqrt{6}\mu\Delta\bar{\eta}^{in}_{(n+1)}n_{ij(n+1)} \tag{C.21}$$

$$s_{ij(n+1)} = s^{trial}_{ij(n+1)} - \sqrt{6}\mu\Delta\bar{\eta}^{in}_{(n+1)}n_{ij(n+1)} \tag{C.22}$$

where

$$\sigma^{trial}_{ij(n+1)} = \sigma_{ij(n)} + L_{ijkl}\Delta\varepsilon_{kl(n+1)} \tag{C.23}$$

$$s^{trial}_{ij(n+1)} = s_{ij(n)} + 2\mu\Delta\eta_{ij(n+1)} \tag{C.24}$$

$$\Delta\bar{\eta}^{in}_{n+1} = \Delta t\dot{\bar{\eta}}^{in}_{(n+1)} \tag{C.25}$$

The equilibrium stress at time $t_{(n+1)}$ is given as

$$\begin{aligned} g_{ij(n+1)} &= g_{ij(n)} + \frac{\psi}{E}\Big[2\mu\Delta\eta_{ij(n+1)} \\ &- \sqrt{6}\mu\Delta\bar{\eta}^{in}_{(n+1)}n_{ij(n+1)} + \Delta t\frac{o_{ij(n+1)}}{k_{(n+1)}} \\ &- E\Delta\bar{\eta}^{in}_{(n+1)}\frac{g_{ij(n+1)}}{A_{(n+1)}}\Big] - \Delta tR\left|g_{ij(n)}\right| g_{ij(n+1)} \end{aligned} \tag{C.26}$$

where

$$A_{(n+1)} = \frac{A_{(n)} + A_c A_f \Delta\bar{\eta}^{in}_{(n+1)}}{1 + A_c\Delta\bar{\eta}^{in}_{(n+1)}} \tag{C.27}$$

Recalling $o_{ij(n+1)} = \sqrt{2/3}\Gamma_{(n+1)}n_{ij(n+1)}$, Eq. (C26) can be rearranged as

$$\begin{aligned} &g_{ij(n+1)}\left(1+\frac{\psi}{A_{(n+1)}}\Delta\bar{\eta}^{in}_{(n+1)}+\Delta tR\left|g_{ij(n)}\right|\right) \\ &= \left(g_{ij(n)}+\frac{2\psi\mu}{E}\Delta\eta_{ij(n+1)}\right)+\frac{\psi}{E}\Big(-\sqrt{6}\mu \\ &+\sqrt{\frac{2}{3}}E\Big)\Delta\bar{\eta}^{in}_{(n+1)}n_{ij(n+1)} \end{aligned} \tag{C.28}$$

Define

$$g_{ij(n+1)} = C_1 g^{trial}_{ij(n+1)} + C_2 n_{ij(n+1)} \tag{C.29}$$

where

$$C_1 = \frac{A_{(n+1)}}{A_{(n+1)}+\psi\Delta\bar{\eta}^{in}_{(n+1)}+A_{(n+1)}\Delta tR\left|g_{ij(n)}\right|} \tag{C.30}$$

$$C_2 = C_1\frac{\psi}{E}\Delta\bar{\eta}^{in}_{(n+1)}\left(-\sqrt{6}\mu+\sqrt{\frac{2}{3}}E\right) \tag{C.31}$$

$$g^{trial}_{ij(n+1)} = g_{ij(n)} + \frac{2\psi\mu}{E}\Delta\eta_{ij(n+1)} \tag{C.32}$$

Since $o_{ij(n+1)} = s_{ij(n+1)} - g_{ij(n+1)}$ and $s_{ij(n+1)} = s^{trial}_{ij(n+1)} - \sqrt{6}\mu\Delta\bar{\eta}^{in}_{(n+1)}n_{ij(n+1)}$, we have

$$\left(\sqrt{\frac{2}{3}}\Gamma_{(n+1)}+C_3\right)n_{ij(n+1)} = s^{trial}_{ij(n+1)} - C_1 g^{trial}_{ij(n+1)} \tag{C.33}$$

where

$$C_3 = \sqrt{6}\mu\Delta\bar{\eta}^{in}_{(n+1)} + C_2 \tag{C.34}$$

Take the inner product for both sides of Eq. (C33), we have

$$\begin{aligned} F(\Gamma_{(n+1)}) \doteq &\left(\sqrt{\frac{2}{3}}\Gamma_{(n+1)}+C_3\right)^2 - \Big(s^{trial}_{ij(n+1)} \\ &- C_1 g^{trial}_{ij(n+1)}\Big)\Big(s^{trial}_{ij(n+1)} - C_1 g^{trial}_{ij(n+1)}\Big) = 0 \end{aligned} \tag{C.35}$$

$\Gamma_{(n+1)}$ can be found by solving a nonlinear Eq. (C35) using the Newton method. A consistent tangent for the Newton method is

$$\begin{aligned} \frac{\partial F(\Gamma_{(n+1)})}{\partial\Gamma_{(n+1)}} &= 2\left(\sqrt{\frac{2}{3}}\Gamma_{n+1}+C_3\right)\left(\sqrt{\frac{2}{3}}+\frac{\partial C_3}{\partial\Gamma_{(n+1)}}\right) \\ &+ 2\left(s^{trial}_{ij(n+1)} - C_1 g^{trial}_{ij(n+1)}\right)\frac{\partial C_1}{\partial\Gamma_{(n+1)}}g^{trial}_{ij(n+1)} \end{aligned} \tag{C.36}$$

$$\frac{\partial C_3}{\partial\Gamma_{(n+1)}} = \sqrt{6}\mu\frac{\partial\Delta\bar{\eta}^{in}_{(n+1)}}{\partial\Gamma_{n+1}} + \frac{\partial C_2}{\partial\Gamma_{(n+1)}} \tag{C.37}$$

$$\frac{\partial\Delta\bar{\eta}^{in}_{(n+1)}}{\partial\Gamma_{(n+1)}} = \frac{\Delta t}{Ek^2}\left(k - \Gamma_{(n+1)}\frac{\partial k}{\partial\Gamma_{(n+1)}}\right) \tag{C.38}$$

$$\frac{\partial k}{\partial\Gamma_{(n+1)}} = -\frac{k_1 k_3}{k_2}\left(1+\frac{\Gamma_{(n+1)}}{k_2}\right)^{-k_3-1} \tag{C.39}$$

$$\begin{aligned} \frac{\partial C_2}{\partial\Gamma_{(n+1)}} &= \frac{\psi}{E}\left(-\sqrt{6}\mu+\sqrt{\frac{2}{3}}E\right) \\ &\times\left(\frac{\partial C_1}{\partial\Gamma_{(n+1)}}\Delta\bar{\eta}^{in}_{(n+1)} + \frac{\partial\Delta\bar{\eta}^{in}_{(n+1)}}{\partial\Gamma_{(n+1)}}C_1\right) \end{aligned} \tag{C.40}$$

$$\frac{\partial C_1}{\partial \Gamma_{(n+1)}} = \frac{\partial A_{(n+1)}}{\partial \Gamma_{(n+1)}} \Big[\left(1+\Delta t R \left|g_{ij(n)}\right|\right) A_{(n+1)} + \psi \Delta \bar{\eta}^{in}_{(n+1)} \Big]^{-1} - A_{(n+1)} \Big[\left(1+\Delta t R \left|g_{ij(n)}\right|\right) \times A_{(n+1)} + \psi \Delta \bar{\eta}^{in}_{(n+1)} \Big]^{-2} \Big[\left(1+\Delta t R \left|g_{ij(n)}\right|\right) \times \frac{\partial A_{(n+1)}}{\partial \Gamma_{(n+1)}} + \psi \frac{\partial \Delta \bar{\eta}^{in_{(n+1)}}}{\partial \Gamma_{(n+1)}} \Big] \tag{C.41}$$

$$\frac{\partial A_{(n+1)}}{\partial \Gamma_{(n+1)}} = \frac{\left(A_f - A_{(n)}\right) A_c}{\left(1 + A_c \Delta \bar{\eta}^{in}_{(n+1)}\right)^2} \frac{\partial \Delta \bar{\eta}^{in}_{(n+1)}}{\partial \Gamma_{(n+1)}} \tag{C.42}$$

A summary of the implicit back-Euler method for the VBO integration scheme is given in the Algorithm 3.

Algorithm 3 Implicit integration scheme for VBO

1. Database: $\sigma_{ij(n)}$, $g_{ij(n)}$, $A_{(n)}$.
2. Given the strain field $\varepsilon_{ij(n+1)} = \varepsilon_{ij(n)} + \Delta\varepsilon_{ij(n+1)}$.
3. Compute the trial stress.
$$\sigma^{trial}_{ij(n+1)} = \sigma_{ij(n)} + L_{ijkl}\Delta\varepsilon_{kl(n+1)}$$
$$s^{trial}_{ij(n+1)} = \sigma^{trial}_{ij(n+1)} - \frac{1}{3}\delta_{ij}\sigma^{trial}_{kk(n+1)}$$
4. Solve for the nonlinear function $F\left(\Gamma_{(n+1)}\right) = 0$ for $\Gamma_{(n+1)}$ using the Newton method.
5. Compute $\Delta\bar{\eta}^{in}_{(n+1)}$ and $n_{ij(n+1)}$.
$$\bar{\eta}^{in}_{(n+1)} = \Delta t \frac{\Gamma_{(n+1)}}{Ek\left(\Gamma_{(n+1)}\right)}$$
$$n_{ij(n+1)} = \frac{\left(s^{trial}_{ij(n+1)} - C_1 g^{trial}_{ij(n+1)}\right)}{\left(\sqrt{2/3}\Gamma_{(n+1)} + C_3\right)}$$
6. Update the stress and all the internal variables.
$$\sigma_{ij(n+1)} = \sigma^{trial}_{ij(n+1)} - \sqrt{6}\mu\Delta\bar{\eta}^{in}_{(n+1)} n_{ij(n+1)}$$
$$g_{ij(n+1)} = C_1 g^{trial}_{ij(n+1)} + C_2 n_{ij(n+1)}$$
$$A_{(n+1)} = \frac{A_{(n)} + A_c A_f \Delta\bar{\eta}^{in}_{(n+1)}}{1 + A_c \Delta\bar{\eta}^{in}_{(n+1)}}$$

C.4 Formulas for $\Delta\sigma_{ij(n+1)}$ and Consistent Tangent $\frac{\partial \Delta\sigma_{ij(n+1)}}{\partial \Delta\varepsilon_{kl(n+1)}}$

Recall $\sigma_{ij(n+1)} = \sigma^{trial}_{ij(n+1)} - \sqrt{6}\mu\Delta\bar{\eta}^{in}_{(n+1)} n_{ij(n+1)}$, we have

$$\Delta\sigma_{ij(n+1)} = \sigma_{ij(n+1)} - \sigma_{ij(n)} = \sigma^{trial}_{ij(n+1)} - \sqrt{6}\mu\Delta\bar{\eta}^{in}_{(n+1)} n_{ij(n+1)} - \sigma_{ij(n)} \tag{C.43}$$

The consistent tangent is given by

$$\begin{aligned}
\frac{\partial \Delta\sigma_{ij(n+1)}}{\partial \Delta\varepsilon_{kl(n+1)}} &= \frac{\partial}{\partial \Delta\varepsilon_{kl(n+1)}} \left(\sigma^{trial}_{ij(n+1)} - \sqrt{6}\mu\Delta\bar{\eta}^{in}_{(n+1)} n_{ij(n+1)} - \sigma_{ij(n)} \right) \\
&= L_{ijkl} - \sqrt{6}\mu \frac{\partial}{\partial \Delta\varepsilon_{kl(n+1)}} \left(\Delta\bar{\eta}^{in}_{(n+1)} n_{ij(n+1)} \right) \\
&= L_{ijkl} - \sqrt{6}\mu \left(\frac{\partial \Delta\bar{\eta}^{in}_{(n+1)}}{\partial \Delta\varepsilon_{kl(n+1)}} n_{ij(n+1)} + \Delta\bar{\eta}^{in}_{(n+1)} \frac{\partial n_{ij(n+1)}}{\partial \Delta\varepsilon_{kl(n+1)}} \right) = L_{ijkl} - \sqrt{6}\mu \\
&\times \left(\frac{\partial \Delta\bar{\eta}^{in}_{(n+1)}}{\partial \Gamma_{(n+1)}} n_{ij(n+1)} + \Delta\bar{\eta}^{in}_{(n+1)} \frac{\partial n_{ij(n+1)}}{\partial \Gamma_{(n+1)}} \right) \\
&\times \frac{\partial \Gamma_{(n+1)}}{\partial \Delta\varepsilon_{kl(n+1)}}
\end{aligned} \tag{C.44}$$

where

$$\frac{\partial n_{ij(n+1)}}{\partial \Gamma_{(n+1)}} = -\frac{g^{trial}_{ij(n+1)} \frac{\partial C_1}{\partial \Gamma_{(n+1)}}}{\left(\sqrt{2/3}\,\Gamma_{(n+1)} + C_3\right)} - \frac{\left(\sqrt{2/3} + \frac{\partial C_3}{\partial \Gamma_{(n+1)}}\right)\left(s^{trial}_{ij(n+1)} - C_1 g^{trial}_{ij(n+1)}\right)}{\left(\sqrt{2/3}\Gamma_{(n+1)} + C_3\right)^2} \tag{C.45}$$

Equation (C44) has a single unknown $(\partial\Gamma_{(n+1)})/(\partial\Delta\varepsilon_{kl(n+1)})$ (the other terms have already been calculated in the process of solving for $\Gamma_{(n+1)}$ described in the previous section). Differentiating $F\left(\Gamma_{(n+1)}\right) = 0$ gives

$$dF = \frac{\partial F}{\partial \Gamma_{(n+1)}} d\Gamma_{(n+1)} + \frac{\partial F}{\partial \Delta\varepsilon_{ij(n+1)}} \times d\Delta\varepsilon_{ij(n+1)} = 0 \tag{C.46}$$

From Eq. (C35) it follows that

$$\frac{\partial F}{\partial \Delta\varepsilon_{ij(n+1)}} = -2\left(s^{trial}_{ij(n+1)} - C_1 g^{trial}_{ij(n+1)}\right) \times \left(\frac{\partial s^{trial}_{ij(n+1)}}{\partial \Delta\varepsilon_{kl(n+1)}} - C_1 \frac{\partial g^{trial}_{ij(n+1)}}{\partial \Delta\varepsilon_{kl(n+1)}} \right) \tag{C.47}$$

where

$$\frac{\partial s^{trial}_{ij(n+1)}}{\partial \Delta\varepsilon_{kl(n+1)}} = 2\mu \frac{\partial \Delta\eta_{ij}}{\partial \Delta\varepsilon_{kl(n+1)}} = 2\mu \frac{\partial e_{ij(n+1)}}{\partial \Delta\varepsilon_{kl(n+1)}} \tag{C.48}$$

$$\frac{\partial g^{trial}_{ij(n+1)}}{\partial \Delta \varepsilon_{kl(n+1)}} = \frac{2\psi\mu}{E}\frac{\partial \Delta \eta_{ij}}{\partial \Delta \varepsilon_{kl(n+1)}} = \frac{2\psi\mu}{E}\frac{\partial e_{ij(n+1)}}{\partial \Delta \varepsilon_{kl(n+1)}} \tag{C.49}$$

$$\frac{\partial e_{ij(n+1)}}{\partial \Delta \varepsilon_{kl(n+1)}} = I_{ijkl} - \frac{1}{3}\delta_{ij}\delta_{kl} \tag{C.50}$$

Since $(\partial F)/(\partial \Gamma_{(n+1)})$ has been already computed, from Eq. (C36) we have

$$\frac{\partial \Gamma_{(n+1)}}{\partial \Delta \varepsilon_{ij(n+1)}} = -\left(\frac{\partial F}{\partial \Gamma_{(n+1)}}\right)^{-1}\frac{\partial F}{\partial \Delta \varepsilon_{ij(n+1)}} \tag{C.51}$$

And finally, $(\partial \Delta \sigma_{ij(n+1)})/(\partial \Delta \varepsilon_{kl(n+1)})$ follows from Eq. (C44).

Journal for Multiscale Computational Engineering 8(6), 631–640 (2010)

ENERGY-BASED FUSION SCHEME FOR SURVEILLANCE AND NAVIGATION

S. Senthil Kumar,[1,] S. Muttan,[2] & K. Mahesh Bharath[3]*

[1]*Research Scholar, Anna University Chennai, Department of Electronics and Communication Engineering, Anna University, Chennai 600025, India*

[2]*Professor, Anna University Chennai, Department of Electronics and Communication Engineering, Anna University, Chennai 600025, India*

[3]*St. Joseph's College of Engineering Chennai, Department of Electronics and Communication Engineering, St. Joseph's College of Engineering, Chennai 600119, India*

[*]Address all correspondence to S. Senthil Kumar E-mail: ssk_puliyur@yahoo.com

Image fusion is used to integrate multiple images into a composite image which contains complementary information from each of the source images. In defense applications, fusion is widely employed to obtain images pertaining to the object under surveillance and also for mapping terrain for navigation purposes. Although there are a many fusion algorithms reported in the literature, the need is for a computationally efficient fusion rule that can be implemented easily in hardware. Driven by this motivation we have formulated a discrete wavelet transform–based fusion technique that uses the energy of the wavelet coefficients to determine the fusion weights for the approximate image and choose maximum intensity rule for the detail image. Surveillance imaging generally uses two imaging sources, one an infrared camera and the other a conventional digital camera, and the images are usually captured under low lighting and night-time conditions. We used the structural similarity index, mutual information, and standard deviation as metrics to evaluate the performance of our fusion scheme with existing algorithms. Our experiments have shown that the algorithm developed produces good results under the constraints imposed by this application.

KEY WORDS: *image fusion, surveillance and navigation, discrete wavelet transform, energy of wavelet coefficients, structural similarity index, mutual information*

1. INTRODUCTION

Image fusion finds widespread application in night-time surveillance and navigation systems used by the military. These require the ability to detect targets and obstructions under low-light conditions. Night vision images are usually obtained by means of conventional charge-coupled device (CCD) cameras which produce a low-intensity image, or forward-looking infrared (FLIR) cameras which give an infrared image. However, both these cameras do not capture all available information due to the characteristics of the sensors employed. While the FLIR camera responds to variations in heat, they cannot capture the variations in intensity. The CCD cameras, on the other hand, respond to the illumination of the scene and give an image that has visible details as perceived by the human visual system. Hence, the need arises for a data fusion technique that can combine the information from each of these images to produce a composite output image that can be processed for further analysis.

The pixel level image fusion algorithms reported in the literature are broadly classified as statistical fusion schemes and multiresolution analysis-based fusion. Das and Krebs (2000) proposed a principal component analysis (PCA)–based fusion scheme for navigation and surveillance. Apart from this, experimental tests have been carried out for various fusion algorithms using night-time images and the results have been reported in Chen and Blum (2005) and Canga et al. (2005). The PCA-based fusion rule (Das et al., 2000) is efficient in terms of the

1543–1649/10/$35.00

output fused image quality; however, implementing it in real time is more involved. This arises due to the matrix multiplication operations involved in the computation of the principal components. As the size of the input image increases, the matrix dimensions increase, making cost-effective implementation not feasible. According to our literature survey, there have not been many publications reported in this area. This has been a motivation for our research, to present a new and efficient algorithm.

In this paper we present a multiresolution-based fusion scheme using the discrete wavelet transform (DWT). This algorithm proposes a weighted fusion scheme for the approximation sub-images, where the weights are calculated based on the energy of the DWT coefficients. The detail sub-images are fused using the rule of choosing the maximum intensity pixels. The paper is organized as follows: Section 2 details the image fusion methodology using wavelet transform and the proposed fusion scheme is described. In Section 3, the various quality metrics deployed to evaluate the performance of the fusion scheme are outlined. Section 4 gives the results obtained and compares the performance with existing fusion techniques.

2. DISCRETE WAVELET TRANSFORM-BASED FUSION

The multiresolution image fusion algorithms used widely follow two stages: First, they decompose the input image into multiple resolution levels using different decomposition methods. Then they combine the decomposition images of specific levels using fusion rules to obtain the fused output. The pyramid decomposition and wavelets are the commonly used multiresolution image decomposition schemes. The pyramidal decomposition has been implemented using various algorithms such as Toet's ratio pyramid (1989), the contrast pyramid–based fusion of Toet et al. (1989), the generalized Laplacian pyramid (GLP) method put forward by Kim et al. (1993), and Burt's Gaussian pyramid (GP) and the enhanced Laplacian pyramid (ELP) (1984). However, in these methods the computations involved increase rapidly with an increase in the decomposition levels, and hence a tradeoff is sought between the accuracy and the computation in applications.

The DWT-based fusion techniques involve the initial multiresolution decomposition of the input images, combining the coefficients of the corresponding levels using fusion rules and finally, synthesizing the fused image using inverse discrete wavelet transform (IDWT). The flow of a DWT-based fusion scheme is illustrated in Fig. 1.

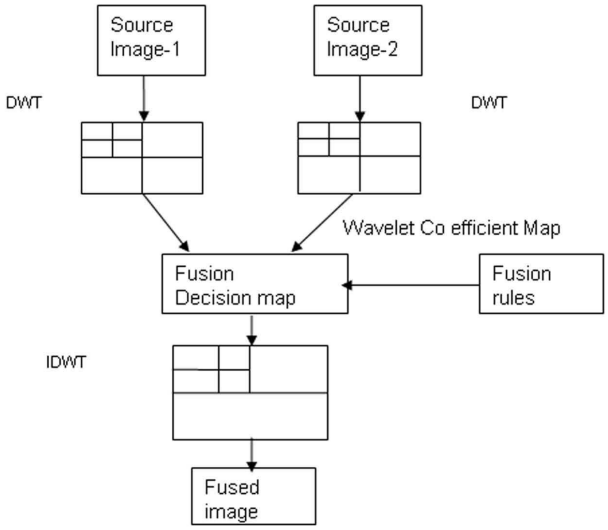

FIG. 1: Flow of DWT-based data fusion method.

Actually the fusion rules adopted in images select maximum or minimum for detail images. Averaging the approximation of images results in a problem in that the fused images are inconsistent. Detailed images contain important information such as image edges, lines, and region boundaries. The approximation image represents the low-frequency component of the image. Hence, while combining these images, the useful low-frequency component information must be transferred from the sources to the fused output image. To better meet the need of human visual systems, fusion rules of detail images usually acquire salient information and sharper contrast that is easier for observation. The fusing of detail information requires preserving the edges in the source images and avoiding the introduction of artifacts in the fused image due to the high-frequency components.

Numerous fusion rules have been published in the literature, and most of these techniques used a weighting scheme to combine the coefficients. Our fusion scheme uses the energy of the wavelet coefficients to determine the fusion weights.

2.1 DWT Energy-Based Weighted Fusion Algorithm

This algorithm proposes a weighted fusion scheme for the approximation sub-images, where the weights are calculated based on the energy of the DWT coefficients. The detail sub-images are fused using the rule of choosing

the maximum intensity pixels. This effectively makes use of the energy of the source images upon knowing the weights of the corresponding source images at the fused output image.

Here we assume the images to be designated as I_{vis} and I_{ir}, corresponding to the inputs from the CCD camera and the IR camera. The approximation sub-images are A_{vis} and A_{ir}, and the detail components are H_{vis} and H_{ir} (horizontal details), V_{vis} and V_{ir} (vertical details), and D_{vis} and D_{ir} (diagonal details). All the individual detail components can be represented by Det_{vis} and Det_{ir} in general.

The image of a road has been considered for illustrating the fusion scheme. Both the IR camera and the CCD camera source images are decomposed using the DWT for a single decomposition level, as shown in Fig. 2.

2.1.1 Approximation Sub-Image Fusion Rule

The basic fusion rule for the low-frequency approximation is the weighted image fusion given by

$$\mathrm{App_{fuse}} = (\mathrm{w_1} \times \mathrm{A_{vis}}) + (\mathrm{w_2} \times \mathrm{A_{ir}}) \tag{1}$$

where w_1 and w_2 are the normalized weights computed from the energy of the approximation coefficients, and App_{fuse} is the fused approximation image.

The weights have been computed from the energy so that the image which has the highest energy has more weight at the fused output image. This implies that the fused output image receives more information from the source image, which has higher energy, and much less information is taken from a low-energy content source image.

The energies of the approximation images, E_{a1} and E_{a2}, are calculated using the general expression for energy

$$\mathrm{E_{a1}} = \sum_{\mathrm{i,j}} \left(\mathrm{A_{ir}(i,j)}\right)^2 \tag{2}$$

$$\mathrm{E_{a2}} = \sum_{\mathrm{i,j}} \left(\mathrm{A_{vis}(i,j)}\right)^2 \tag{3}$$

The normalization factor E_t is then calculated as the maximum energy value of the two images.

$$\mathrm{E_t} = \mathrm{Max}\left\{\sum_{\mathrm{i,j}} \left(\mathrm{A_{ir}(i,j)}\right)^2, \sum_{\mathrm{i,j}} \left(\mathrm{A_{vis}(i,j)}\right)^2\right\} \tag{4}$$

Then the weights w_1 and w_2 are given by

$$\mathrm{w_1} = \frac{\mathrm{E_{a1}}}{\mathrm{E_t}} \tag{5}$$

$$\mathrm{w_2} = \frac{\mathrm{E_{a2}}}{\mathrm{E_t}} \tag{6}$$

where w_1 and w_2 lie in the range 0 to 1.

From experimentation it has been determined that using the normalization value E_t for finding out the weights w_1 and w_2 gives better results than using the energy of the source images directly. One of the weighting factors is almost equal to one and the other is less than one but not zero. The result of fusing the approximation components using the energy-based weighted fusion scheme is shown in Fig. 3.

2.1.2 Detail Sub-Image Fusion Rule

The detail components of the DWT decomposition are combined using the method of obtaining the fused output by selecting the maximum intensity pixels from each of the detail sub-image. This method ensures that the high-frequency edge details that are present in each of the sub-images are appropriately retained in the fused image. Mathematically, the decision map for this is given by

$$\mathrm{Det_{fuse}(i,j)} = \begin{cases} |\mathrm{Det_{ir}(i,j)}| \\ \text{if} \quad |\mathrm{Det_{ir}(i,j)}| > |\mathrm{Det_{vis}(i,j)}| \\ \\ |\mathrm{Det_{vis}(i,j)}| \\ \text{if} \quad |\mathrm{Det_{ir}(i,j)}| < |\mathrm{Det_{vis}(i,j)}| \end{cases} \tag{7}$$

where, i = 1, 2, 3, ... S_i; j = 1, 2, 3, ... S_j[$S_i \times S_j$] is the dimension of the detail sub-image, and Det_{fuse}(i, j) is the fused detail image. As per our fusion rule, the detailed maximum of image coefficients is calculated either from an IR image or CCD image, so the resultant pixel value of detailed image is also only 8 bit. The resultant fused detail image is shown in Fig. 4.

The final fused image is then obtained by taking the inverse discrete transform using the fused detail and approximation sub-images. The resultant image as shown in Fig. 5 shows that information from both the sources is present in the output and the image also has an appreciably good subjective quality.

3. FUSION PERFORMANCE METRIC

The multisensor image fusion methods outlined in this paper are directed toward applications in the areas of surveillance and navigation. In these applications, due to the real-time nature of the scene being imaged, there are no ground truth data available and so evaluating the performance of such fusion schemes requires the use of nonreference-quality metrics. We have used the following

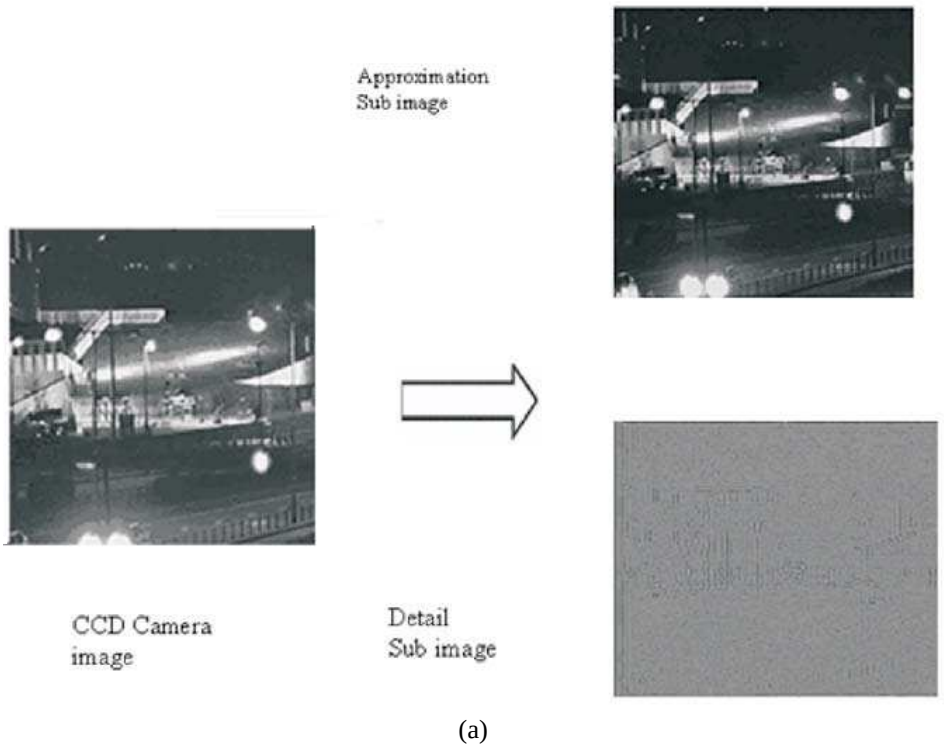

(a)

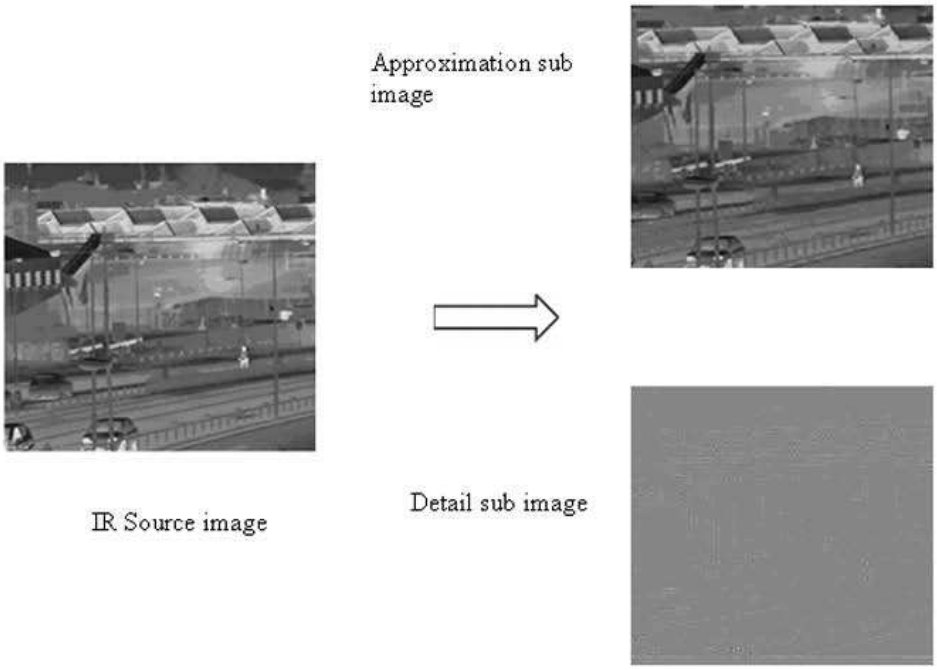

(b)

FIG. 2: DWT decomposition of **(a)** CCD and **(b)** IR image.

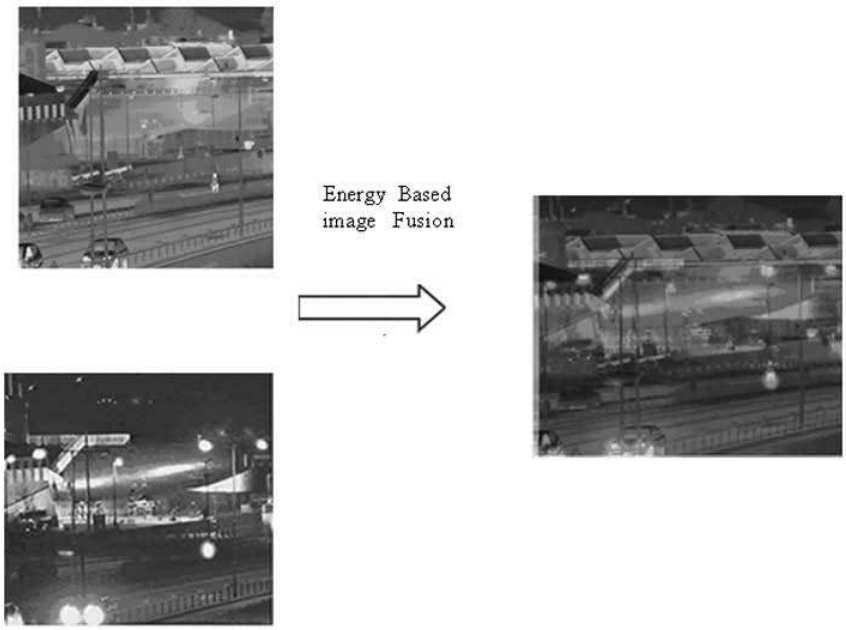

FIG. 3: Weighted fusion of approximation sub-images based on energy.

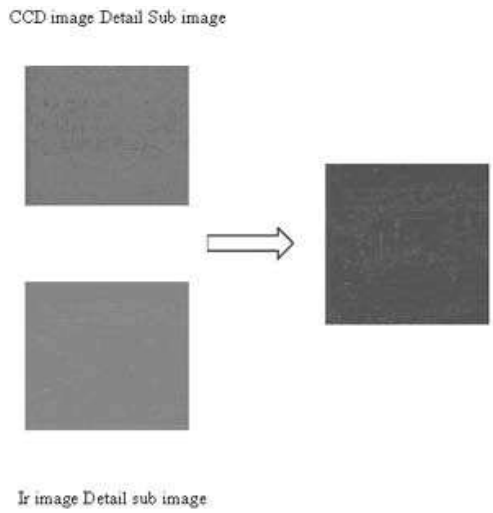

FIG. 4: Result of fusing detail components using choose maximum rule.

FIG. 5: Result of fusing using the energy-based fusion algorithm.

four metrics to compute the efficiency of our algorithm: entropy, mutual information (MI), SSIM-based measure (SI), and standard deviation (SD). Structure, intensity, and contrast detail gives the better view for human perception. The SSIM index produces the index value based on structure similarity of images, intensity, and contrast detail, so it is quite capable of measuring image quality. Entropy measures the amount of information and is a useful metric to compare source and fused images in a noise-free environment. SD measures the contrast detail. The evaluation of image quality by subjective testing gives additional support to the above metrics.

3.1 Mutual Information (MI)

Mutual information has been employed as a means of assessing image fusion quality. This metric is utilized to determine the amount of information transferred from source images to fused images. It is calculated by defining the joint histogram of the source image I_{vis}, I_{ir} and the fused image I_{fuse} as p(fuse, ir) and p(fuse, vis). The mutual information between the source image and the fused image is given by Qu et al. (2002) as

$$\mathrm{Mi}_1(\mathrm{fuse},\mathrm{ir}) = -\sum \mathrm{p}(\mathrm{fuse},\mathrm{ir}) \times \log_2\left\{\frac{\mathrm{p}(\mathrm{fuse},\mathrm{ir})}{[\mathrm{p}(\mathrm{fuse})\,.\,\mathrm{p}(\mathrm{ir})]}\right\} \tag{8}$$

$$\mathrm{Mi}_2(\mathrm{fuse},\mathrm{vis}) = -\sum \mathrm{p}(\mathrm{fuse},\mathrm{vis}) \times \log_2\left\{\frac{\mathrm{p}(\mathrm{fuse},\mathrm{vis})}{[\mathrm{p}(\mathrm{fuse})\,.\,\mathrm{p}(\mathrm{vis})]}\right\} \tag{9}$$

where p(fuse, ir) and p(fuse, vis) are the joint histograms of the source image I_{vis}, I_{ir} and the fused image I_{fuse}. Image fusion performance is measured by size, where a larger measure implies better image quality. The fusion algorithm efficiency is determined by the metric MI which is defined by

$$\mathrm{MI} = \mathrm{Mi}_1(\mathrm{fuse},\mathrm{ir}) + \mathrm{Mi}_2(\mathrm{fuse},\mathrm{vis}) \tag{10}$$

3.2 Structural Similarity Index-Based Measure (SI)

The SSIM index proposed by Wang et al. (2004) is used as an objective image quality metric to indicate the similarity of the structure information present in the two images being compared. The SSIM of two images x and y is defined as

$$\mathrm{SSIM}(\mathrm{x},\mathrm{y}) = \frac{(2\mathrm{m_x m_y} + \mathrm{C}_1)(2\sigma_{\mathrm{xy}} + \mathrm{C}_2)}{(\mathrm{m_x^2} + \mathrm{m_y^2} + \mathrm{C}_1)(\sigma_{\mathrm{x}}^2 + \sigma_{\mathrm{y}}^2 + \mathrm{C}_2)} \tag{11}$$

where, m_x is the mean intensity of image x, σ_x is the standard deviation of image x used as an estimate of image contrast, and C_1 and C_2 are constants. However, the SSIM is a full-reference approach and requires the need for a complete reference image for its calculation. This impediment is overcome by separately calculating the amount of structural information transferred from each of the source images to the fused image, SSIM(fuse, ir) and SSIM(fuse, vis). Then the SSIM index for the fused image is calculated by (Maruthi and Suresh, 2007)

$$\mathrm{SI} = \mathrm{SSIM}(\mathrm{fuse},\mathrm{ir}) + \mathrm{SSIM}(\mathrm{fuse},\mathrm{vis}) \tag{12}$$

3.3 Standard Deviation (SD)

For a fused image of size N × M, the standard deviation is given by

$$\mathrm{SD} = \sqrt{\frac{1}{\mathrm{NM}}\sum_{\mathrm{i}=1}^{\mathrm{N}}\sum_{\mathrm{j}=1}^{\mathrm{M}}(\mathrm{I}_{\mathrm{fuse}}(\mathrm{i},\mathrm{j}) - \mathrm{m}_{\mathrm{fuse}})^2} \tag{13}$$

where I_{fuse}(i, j) is the *(i,j)*th pixel intensity value and m_{fuse} is the sample mean of all pixel values of the fused image. The SD value gives the contrast of the image; a higher SD value signifies a better contrast in the gray levels of the image. The SD is composed of the signal part and the noise part, and this measurement is more efficient in the absence of noise (Chen and Blum, 2005).

4. EXPERIMENTAL RESULTS

The experimental results were obtained using various sets of images and the results using the proposed new method compared with existing fusion schemes. Three sets of images were selected: the road image and the boat image corresponding to night-time navigation application, and the house on hill image corresponds to a surveillance application. These images were obtained from Image Fusion (www.imagefusion.org). The Laplacian pyramid scheme for image fusion (Zhang and Blum, 1999; Burt and Adelson, 1983) and the DWT weighted fusion using the principal components as weights (Zheng et al., 2007) were considered for a comparative study of the new energy-based DWT fusion scheme.

The fusion outputs for the different images are shown in Figs. 6–8. Different parameters such as Entropy, SSIM, Mutual information and Standard deviation have been compared and listed out in Table 1. The SSIM values show that the new energybased rule performs as well as the Laplacian pyramid and outperforms the DWT PCA fusion scheme, though the Laplacian fusion shows a higher SSIM value. MI is lower in all three images. MI represents the amount of information transformed from source to fused image. We have considered the highest MI as the best value when SSIM is only slightly low. From the tabulated results, SD is higher in our proposed scheme as compared to the Laplacian pyramid, which gives the highest SSIM. Though the SD computed is higher for DWT PCA, the corresponding SSIM is the least of all three methods. From a complexity point of view, the wavelet-based reduction method yields the order of O(MN), where N is the number of bands and M is the number of pixels in the spatial domain. On the other hand, the total estimated

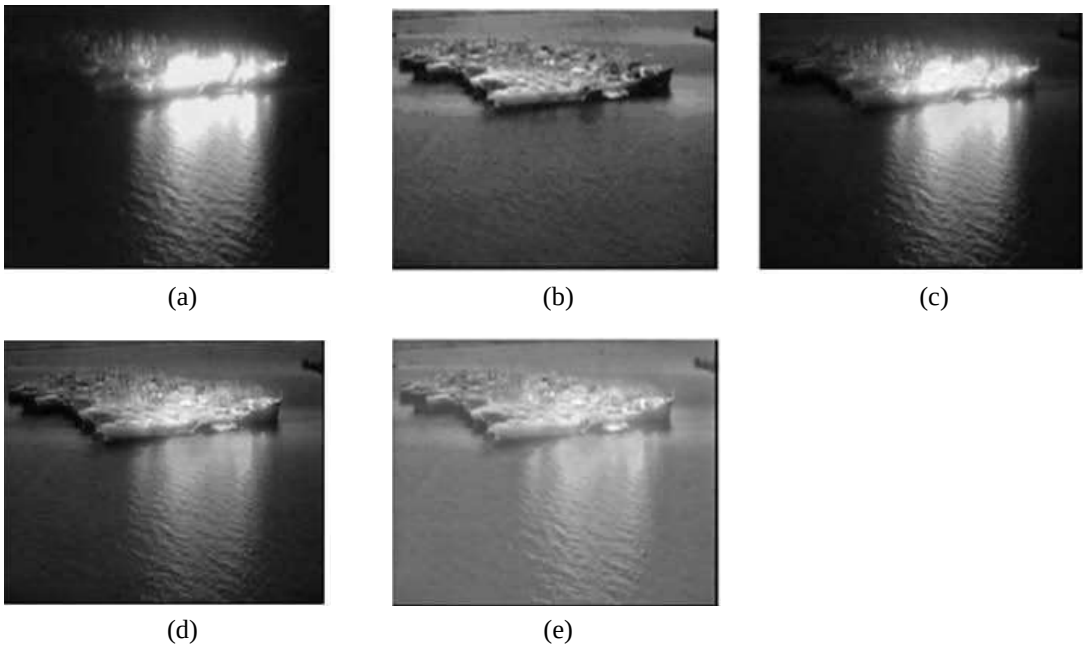

FIG. 6: Results of MRA-based fusion algorithms for "boat" image: **(a)** CCD camera source image, **(b)** IR camera source image, **(c)** DWT PCA max fused image, **(d)** DWT energy-fused image, and **(e)** Laplacian fused image.

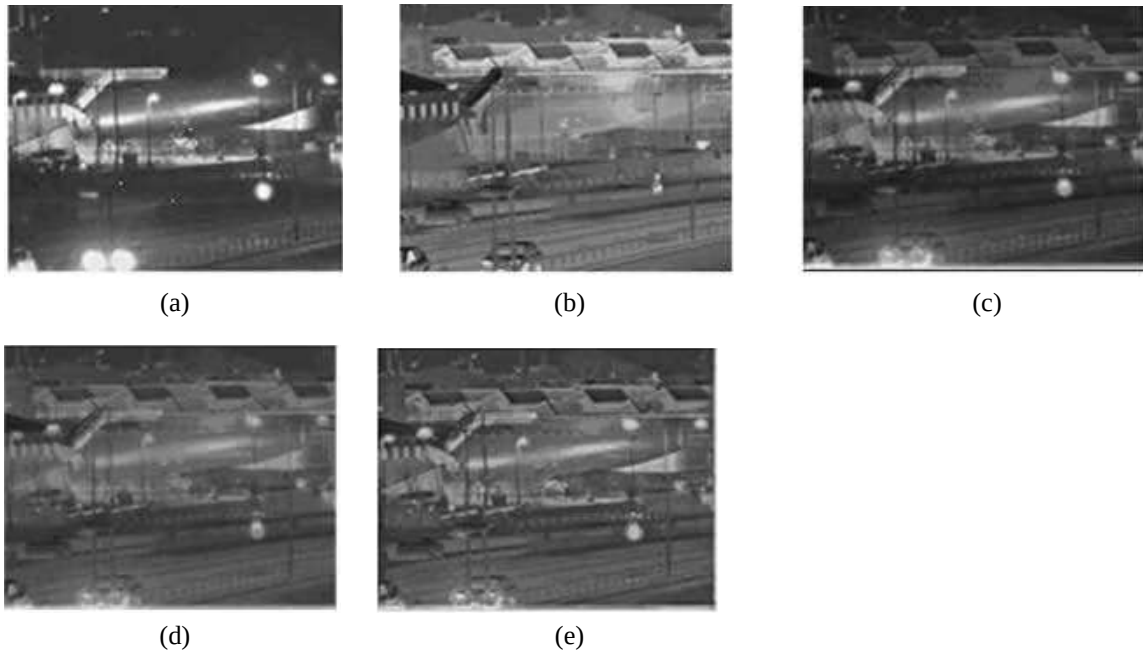

FIG. 7: Results of MRA-based fusion algorithms for "road" image: **(a)** CCD camera source image, **(b)** IR camera source image, **(c)** DWT PCA max fused image, **(d)** DWT energy-fused image, and **(e)** Laplacian fused image.

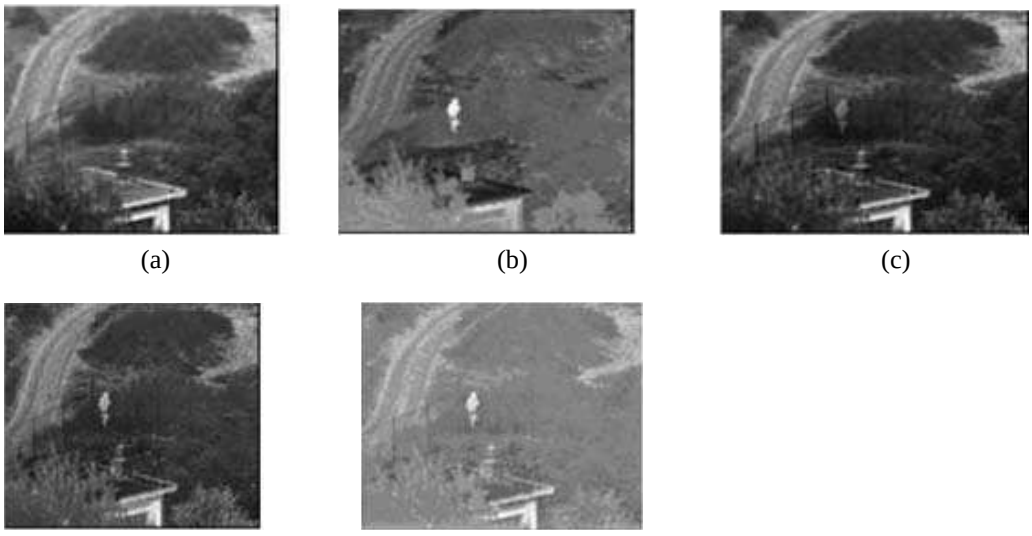

(a) (b) (c)

(d) (e)

FIG. 8: Results of MRA-based fusion algorithms for "house on hill" image: **(a)** CCD camera source image, **(b)** IR camera source image, **(c)** DWT PCA max fused image, **(d)** DWT energy-fused image, and **(e)** Laplacian fused image.

TABLE 1: Comparison of fusion quality metrics.

Image	Fusion scheme	En	SSIM	MI	SD
Boat	DWT energy	7.1679	0.5636	3.8379	78.1263
	DWT PCA max	7.0557	0.2275	4.2786	316.506
	Laplacian pyramid	6.6104	0.6816	3.2648	45.4758
Road	DWT energy	6.9639	0.5635	2.5039	86.1933
	DWT PCA max	7.0566	0.2678	2.7189	200.599
	Laplacian pyramid	6.9988	0.7046	2.1312	54.2838
House on hill	DWT energy	6.7851	0.5527	1.5555	44.1744
	DWT PCA max	6.9453	0.1836	2.2319	129.664
	Laplacian pyramid	6.1980	0.7164	1.3372	30.4117

complexity of PCA is $O((MN)^2 + N^3)$, which shows that the computation efficiency of a wavelet reduction technique is superior to the efficiency of the PCA method.

Subjective test ranking was carried out with 20 human visual perception, and as seen in the tabulated results, the DWT energy-based scheme gives the best result. A visual inspection shows that images fused using the Laplacian algorithm have a lower contrast compared to the other two methods. A visual perception assessed by subjective testing also indicates that the energy fusion scheme performs better than other methods. Also, it can be inferred that the SSIM index is also used as a quality metric for non-reference images that reflect the fused image quality as perceived by the human visual system.

5. CONCLUSION

In this paper, we present a new energy-based fusion algorithm that uses the DWT for multiresolution decomposition of source images. The approximation sub-image uses the energy of wavelet coefficients as weights for fusion, and the detail images are fused by choosing the maximum intensity pixels from either of the source images. The structural similarity and MI analytical measure are used as the parameters to evaluate fusion rule performance. Visual perception also assessed by subjective testing also indicates that the energy fusion scheme performs better than other methods. The results are very impressive for night vision applications such as surveillance and navigation,

and they prove to be better than existing multiresolution-based fusion methods.

REFERENCES

Burt, P. J. and Adelson, E. H., The Laplacian pyramid as a compact image code, *IEEE Trans. Commun.*, vol. **31**(4), pp. 532–540, 1983.

Burt, P. J., The pyramid as a structure for efficient computation, in Rosenfeld, A., Ed., *Multiresolution Image Processing and Analysis*, Berlin: Springer-Verlag, 1984.

Das, S., Zhang, Y.-L., and Krebs, W. K., Color night vision for navigation and surveillance, *Proc. of the Fifth Joint Conf. on Information Science*, 2000.

Canga, E. F., Nikolov, S. G., Canagarajah, C. N., Bull, D. R., Dixon, T. D., Noyes, J. M., and Troscianko, T., Characterization of image fusion quality metrics for surveillance applications over band-limited channels, *Proc. of the 7^{th} Int'l. Conf. on Information Fusion*, pp. 483–490, 2005.

Chen, Y. and Blum, R. S., Experimental tests of image fusion for night vision, *Proc. of the 7^{th} International Conf. on Information Fusion*, pp. 491–498, 2005.

Image Fusion, www.imagefusion.org, December 2008.

Kim, M. G., Dinstein, I., and Shaw, L., A prototype filter design approach to pyramid generation, *IEEE Trans. Pattern Machine Intell.*, vol. **15**(12), pp. 1233–1240, 1993.

Maruthi, R. and Suresh, R. M., Metrics for measuring the quality of fused images, *Proc. of the Int'l. Conf. on Computational Intelligence and Multimedia Applications*, vol. **3**, pp. 153–158, 2007.

Qu, G., Zhang, D., and Yan, P., Information measure for performance of image fusion, *Electron. Lett.*, vol. **38**(7), pp. 313–315, 2002.

Toet, A., Image fusion by a ratio of low pass pyramid, *Pattern Recog. Lett.*, vol. **9**, pp. 245–253, 1989.

Toet, A., van Ruvven, L. J., and Valeton, J. M., Merging thermal and visual images by a contrast pyramid, *Opt. Eng.*, vol. **28**(7), pp. 789–792, 1989.

Wang, Z., Bovik, A. C., Sheikh, H. R., and Simoncelli, E. P., Image quality assessment: From error visibility to structural similarity, *IEEE Trans. Image Process.*, vol. **13**(4), pp. 600–612, 2004.

Zhang, Z. and Blum, R. S., A categorization of multiscale-decomposition-based image fusion schemes with a performance study for a digital camera application, *Proc. IEEE*, vol. **87**(8), pp. 1315–1326, 1999.

Zheng, Y., Hou, X., Bian, T., and Oin, Z., Effective image fusion rules of multiscale image decomposition, *Proc. of the 5^{th} Int'l. Symp. on Image and Signal Processing and Analysis*, pp. 362–366, 2007.

S. Senthil Kumar (Fig. 9) acquired a B.E. degree in electronics and communication engineering from Vellore Engineering College, Vellore, in the year 1988, and an M.Tech. degree in electronics and communication from Pondicherry Engineering College, Pondicherry, 1997. He is currently pursuing the PhD in the Department of Electronics and Communication Engineering, College of Engineering, Anna University, Chennai, India. He has published over seven research papers in national and international journals and conferences. His areas of interest include image fusion, digital signal processing, and digital image processing.

Dr. S. Muttan (Fig. 10) is an assistant professor at Center of Medical Electronics, Department of Electronics and Communication Engineering, Anna University, Chennai, India. He obtained his Masters and PhD degree

FIG. 9: S. Senthil Kumar

FIG. 10: Dr. S. Muttan

from Anna University, Chennai, India. His area of specialization is medical informatics and E-health services. He had his training in medical informatics at Fh. Geissen, Germany. He has published over 40 papers in international and national journals and conferences. He is a life member of Indian Association of Biomedical Scientists, Biomedical Society of India, and ISTE. He was an Academic Council member and executive member of Anna University Research Forum, Anna University, Chennai, India.

K. Mahesh Bharath acquired a BE degree in electronics and communication engineering from St. Joseph's College of Engineering, Chennai, India, in 2009. He is currently a research assistant in the R&D Laboratory at St. Joseph's College of Engineering. His interests include image processing and digital signal processing.

International Journal for
Multiscale Computational Engineering

Volume 8, Issue 6 **2010**

TABLE OF CONTENTS